Electrochemical surface science of tungsten and molybdenum oxide clusters on boron nitride nanomesh

Enrico De Bonis

This dissertation is submitted for the degree of

Doctor of Philosophy

October 2023

Department of Chemistry

Declaration

This thesis has not been submitted in support of an application for another degree at this or any other university. It is the result of my own work and includes nothing that is the outcome of work done in collaboration except where specifically indicated. Many of the ideas in this thesis were the product of discussions with my supervisor Professor Stijn Mertens.

Electrochemical surface science of tungsten and molybdenum oxide clusters on boron nitride nanomesh – Enrico De Bonis – October 2023

Abstract

In the pursuit of more efficient heterogeneous catalysts and electrocatalysts, the real-space observation of active sites at the atomic scale under reaction conditions opens exciting possibilities for establishing detailed composition–structure–reactivity relationships. In this work, we focus on the study of small oxide clusters of the early transition metals tungsten and molybdenum using electrochemical scanning tunnelling microscopy (EC-STM). The metal oxide clusters are generated directly in the aqueous electrolyte, with the metals acting as 'electrochemical evaporator', and this process is studied through a combination of cyclic voltammetry, electrochemical impedance spectroscopy, inductively coupled plasma–optical emission spectroscopy and high-resolution mass spectrometry. Once the transition metal oxide clusters are generated, we immobilise them on boron nitride nanomesh, a corrugated monolayer of hexagonal boron nitride on Rh(111) with unique molecular trapping properties. The immobilisation of the oxide clusters is experimentally verified using *ex situ* X-ray photoelectron and Raman spectroscopy, also gauging any chemical changes of the clusters compared to the dispersed state in aqueous environment. Finally, we use EC-STM to directly observe the tungsten and molybdenum oxide cluster-decorated nanomesh surface in the presence of electrolyte under electrochemical potential control. To the best of our knowledge, this is the first study where molybdenum tips have been used for EC-STM observation. By imaging tungsten oxide clusters with Mo tips and *vice versa*, we explore the stable combinations of substrate and tip materials and potentials towards chemically selective imaging at the atomic scale. Moving forward, we will use this knowledge to develop operando electrochemical imaging while an electrocatalytic reaction is ongoing.

Acknowledgements

Table of contents

List of figures

electrified interface. The physical components in the equivalent circuit represent the relative process occurring at the interface and in the solution during the electrochemical reaction. Double layer capacitance (C_d), charge-transfer resistance (R_p) Warburg impedance (W), and solution resistance (R_s). Adapted.[74]

List of tables

1 Introduction

The chemical and physical properties of surfaces are of great interest as their understanding is pivotal in applications, from the production of devices (e.g., semiconductors, functionalised materials) to heterogeneous catalysis. Surfaces can be considered as long-range defects in the solid state since they interrupt the periodicity of the solid matter, generating structural variations. On the molecular level, the atomic and electronic configurations of the surface influence the interactions with species at the interface, affecting adsorption processes or, in the case of catalysed reactions, the pathway evolution. Consequently, the design of heterogeneous catalysts with optimal performance requires an exhaustive, molecular-level understanding of the interactions at the surface.[1, 2]

Obtaining a molecular-level understanding of the chemistry taking place at the liquid/solid interface is not trivial and includes discrimination between atoms at the interface and the bulk phases.[3] Historically, the study of structural and reaction properties of electrochemical interfaces has relied on measurements of Faradaic and non-Faradaic currents as a function of electrode potential and/or time. However, the primary limitation is related to the ensemble-averaging nature of such approach, which results in indirect interpretation rather than direct observation of the surface structures at their molecular and atomic level. On the other hand, research on metal surfaces in ultrahigh vacuum (UHV) benefits from techniques supplying microscopic structural information by means of electron- and photon-based spectroscopies as 'direct' probes of the electronic and vibrational states.[4, 5, 6]

Over the years, a lot of progress has been made in adapting UHV surface science techniques for the characterisation of metal electrodes at microscopic level, two main approaches are distinguished. The first approach involves *ex situ* methods for which the surface is analysed separately in the electrochemical and UHV environments. However, the separation of the approaches between the two environments has an inherent limitation as the surface structure and composition may varies uncontrollably. Alternatively, a more direct approach involves *in situ* characterization of electrochemical interfaces under potential control.[6, 7, 8] The combination of surface science and electrochemistry allowed

for the description of processes occurring on the solid surface at the interface with liquid (or gas), necessary for fundamental research and technological advancements on fields such as electrocatalysis, solar energy harvesting, corrosion, electrochemical energy storage and conversion devices, and sensors.[9, 10, 11, 12]

The invention of scanning tunnelling microscopy (STM) in 1981 made atomic resolution during real-space imaging possible, as the available technologies (e.g., low-energy electron diffraction, field ion microscopy) were based on reciprocal-space techniques, only suitable for measuring periodic structures.[13] Under particular conditions, STM not only provides the crystallographic structure of single crystal surfaces but is also capable of imaging the local chemical structure and electronic density of states of multicomponent surfaces at the atomic scale.[14] Following the initial development in ultra-high vacuum, the STM was quickly adapted to measurements in a liquid environment.[15] Electrochemical STM (EC-STM) was one of the first techniques adopted to study solid-liquid interfaces, allowing for *in situ* real-space imaging of electrode surfaces at the atomic level. Hence, EC-STM swiftly became a significant addition to the array of techniques for investigating local surface structures, reaction dynamics and processes occurring at surfaces in an electrolytic environment.[9, 16]

One of the first areas where *in situ* STM enabled spectacular progress is the understanding of molecular adsorption and self-organisation, crucial for supramolecular chemistry. Non-covalent intermolecular interactions at solid-liquid interface rely on intrinsic properties, which are responsible of the interplay between molecules, the substrate, and the phase in contact with the substrate. Further controls over these interactions are provided by external stimuli (e.g., heat, light).[17, 18]

Figure 1.1 schematises the adsorption and self-organisation process at the solid-liquid interface. To form an ordered adsorbate layer (i.e., a 2-dimensional crystal) on the surface, the molecules have to absorb on the substrate before the self-organisation step by overcoming the diffusional energy barrier. If the diffusion on the surface occurs at suitable rate, the absorbates can form an ordered layer, otherwise disordered structures are obtained as result of kinetic trapping. In the electrolyte, an electrochemical double layer is formed at the electrified solid-liquid interface. The double layer produces a

tuneable high electric field (with an order of magnitude of 10^9 V/m) as it is proportional on the external applied potential. The control over the charge density at the electrode surface allows to regulate most of the energy contributions shown in Figure 1.1. In the case of EC-STM, a similar electric field is localised between the tip and substrate granting precise control of the electrified interface Figure 1.1c. However, the submolecular resolution of the process is limited by the acquisition speed, and generally only stable systems with limited surface diffusion can be investigated.[17, 19]
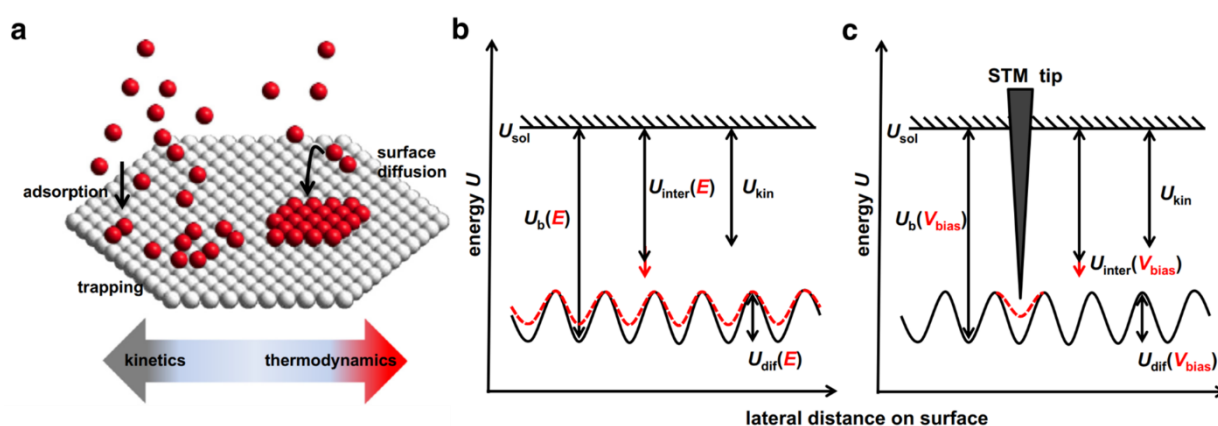
Figure 1.1. (a) Molecular adsorption on the surface followed by self-organisation at solid-liquid interface. Ordered structure may originate when the surface diffusion energy is sufficient to overcome kinetic trapping. (b) Energy landscape at non-electrochemical interface (black trace). At electrified interface (red trace) the adsorption energy (U_b) measured from energy level in solution (U_{sol}), the intermolecular interaction energy (U_{inter}), and the surface diffusion barrier (U_{diff}) can be modulated by the substrate potential E. (c) Energy landscape locally modulated at the electric field between STM tip and substrate ($V_b = E - E_{tip}$). Adapted.[17]

The localised potential control of the EC-STM allowed to gradually and reversibly study *in situ* transitions between supramolecular structures at the electrified solid-liquid interface. The strong field of the electrochemical double layer granted efficient ordering of permanently charged tectons over spontaneous self-assembly which may occur at the solid-liquid interface. The tuning of the electrochemical potential allowed to switch between an open porous structure, to a more compact layer by accommodating another molecule as guest, and finally, to a stacked three-dimensional structure. Such dynamic and precise electrochemical control of a host-guest system capable of switching between a 2D and 3D system may enable applications such as artificial receptors (Figure 1.2).[20]
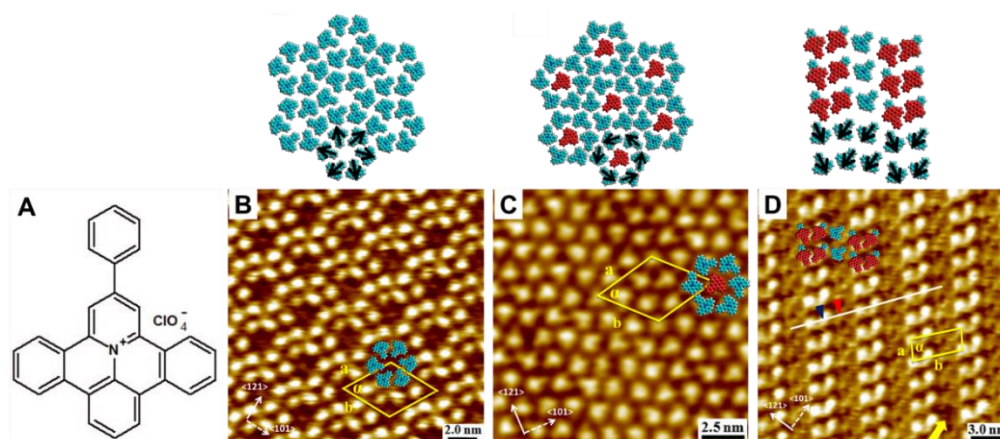
Figure 1.2. STM images of the patterns associated with the proposed models for the (9-phenylbenzo[1,2]quinolizino[3,4,5,6-fed]phenanthridinylium perchlorate) PQPClO$_4$-modified Au(111) in 0.1 M HClO$_4$. B) porous structure I$_t$ = 1.0 nA, V$_b$ = -0.62 V, E$_{sub}$ = 0.6 V vs RHE, van der Waals area of the pore A$_I$=2.5 nm^2. C) self-host-guest structure, I$_t$ = 1.0 nA, V$_b$ = -0.61 V, E$_{sub}$ = 0.4 V vs RHE, A$_I$=3.9 nm^2. D) 3D stacked structures I$_t$ = 1.0 nA, V$_b$ = -0.50 V, E$_{sub}$ = 0.15 V vs RHE. Adapted.[20]

Very recently, STM has allowed to achieve single-molecule switching under ambient conditions of molecular dipoles formed by an organic salt with a large polyaromatic cation and a small anion to reversibly write, read, and erase binary information. The dipole self-assembled on the surface in the presence of a low dielectric solvent which confined and locked together the ion pairs, different from solvated ions in electrochemical environment. The localised electric field of the scanning tip granted precise control over the orientation of individual dipoles as a function of the tunnelling conditions, allowing to write at room temperature binary information at single-molecule level (Figure 1.3).[21]
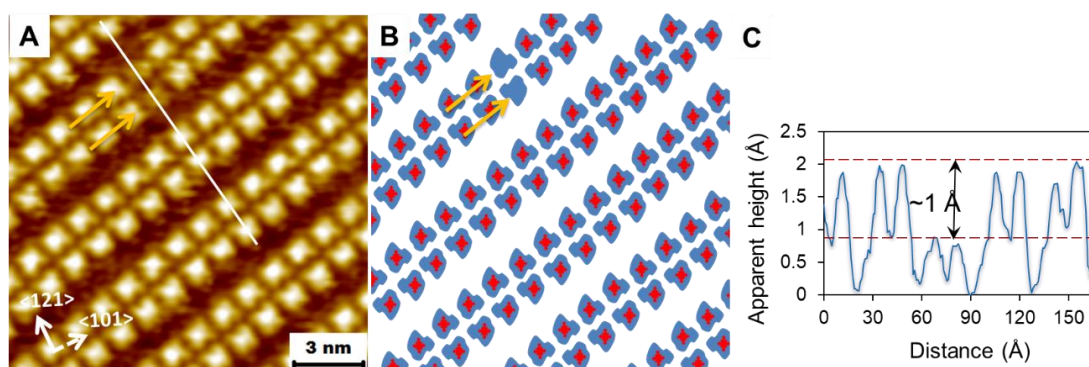
Figure 1.3. A) STM image of Au(111)/PQPC$_{14}$ClO$_4$ (9-tetradecyl-2-phenylbenzo[8,9]-quinolizino-[4,5,6,7-fed]phenanthridinylium perchlorate) (1µM in otanoic acid) V$_b$ = -0.25 V, I$_t$= 80 pA. Bias switching by applying a +0.5V pulse for 30ms. B) Representation of contrast inversion. C) cross-sectional profile along the line in A). Adapted.[21]

4

Moving to the study of chemical reactions, a pioneering paper in 1996 successfully employed the EC-STM to distinguish between two similar porphyrins adsorbed on graphene thanks to the precise and independent control of substrate and probe potentials. The author demonstrated a significant increase in the tunnelling current as a result of the resonance achieved once the Fermi levels of tip and substrate aligned to the energy level of the molecules. Such precise control allowed to finely tune in and out of resonance states and distinguish between structurally similar molecules, only by exploiting their different redox properties (Figure 1.4).[22]
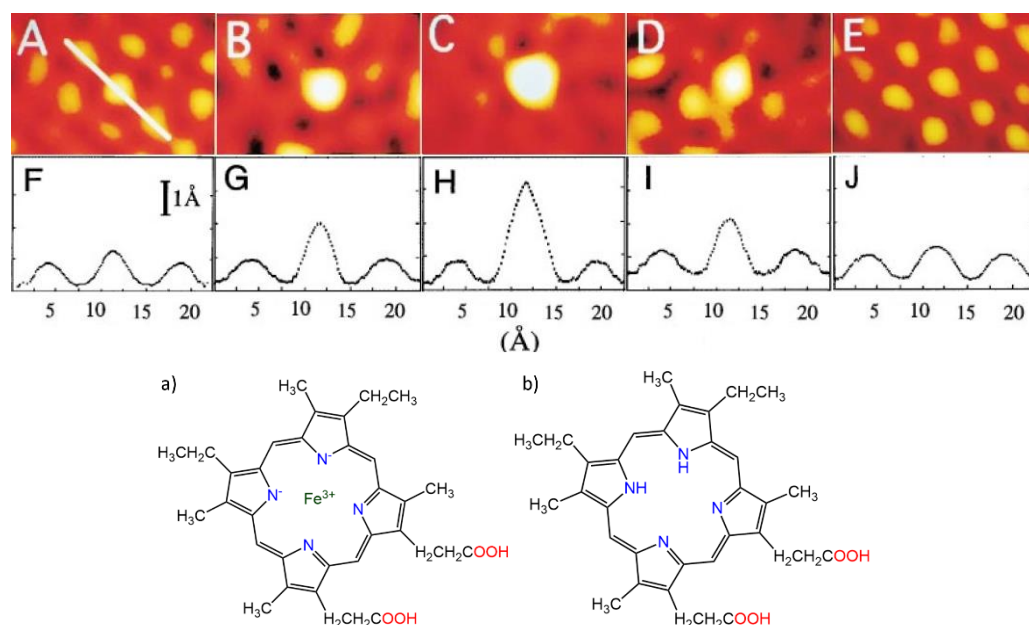
Figure 1.4. STM image of a Fe(III)-protoporphyrin IX molecule (a) embedded in an ordered array of protoporphyrin IX molecules (b) when the substrate is held at -0.15 V(A), -0.30 V(B), -0.42 V (C), -0.55 V (D), and -0.65 V (E), respectively. (F)–(J) the corresponding plots of the cross sections along the white line indicated in (A). The data are symmetrised with respect to the centre. Adapted.[22]

In the late 2000s, EC-STM allowed to control and follow, at the single-molecule level, the oxidation of porphyrins forming a monolayer on gold. In this study, the porphyrins were oxidated by applying short potential pulse. Despite the molecules generating random domains, the slow reduction process allowed to obtain spatially and temporally resolved images, providing insight into the dynamics of interfacial reaction and charge percolation (Figure 1.5).[23]
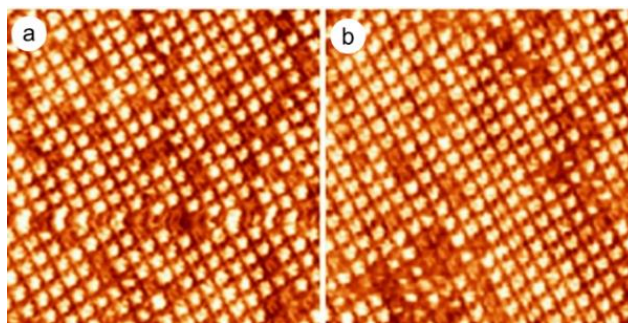
Figure 1.5. STM image of Au(111) in 0.1 M H_2SO_4 (27x27 nm^2, V_b = -0.1 V) with (a) pre-adsorbed porphyrins. (b) After oxidation of the porphyrins with a potential pulse of 0.2 V for duration 1 s, image at V_b = -0.1 V three minutes after obtaining image (a). (Oxidised (darker spots) and reduced (brighter spots) molecules). Adapted.[23]

More recently, STM has been used to investigate the evolution of single molecule in a multi-step reaction at solid/liquid interface. Under environmental control, the high lateral resolution of the STM combined with its capability to identify variation in the electronic properties of the molecules, enabled direct identification of different intermediates at submolecular level of a multi-step catalytic reaction (Figure 1.6). The experimental timescale allowed to monitor in real-space and real-time the reaction dynamics while the conversion between different intermediates was controlled by atmosphere composition and surface potential. The STM provided direct observation of transitions between different species which, more broadly, contributes in defining unique kinetics and mechanistic insights into the investigated reactions.[24]

In electrochemical surface science materials with simple, well-defined characteristic allow for more unambiguous models and essential approach, therefore two-dimensional (2D) materials play a fundamental role.[25] The most studied 2D surfaces include graphene-based materials, for which electronic and electrochemical properties are strongly influenced by their structure; and metal-organic frameworks (MOFs), porous materials with significant degree of tunability and applications.[26, 27] Materials such as metal chalcogenides, transition metal oxides, and other 2D compounds have been discovered and gained renewed interest over the past decades, especially as their distinctive properties allowed for various applications such as optoelectronics, catalysts, sensing, supercapacitors, solar cells, and batteries.[28, 29]
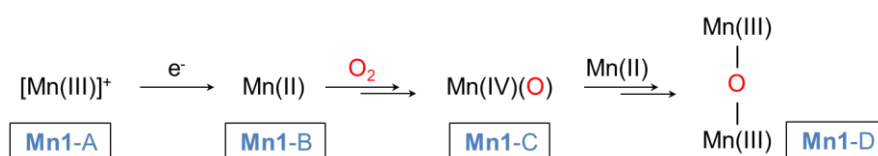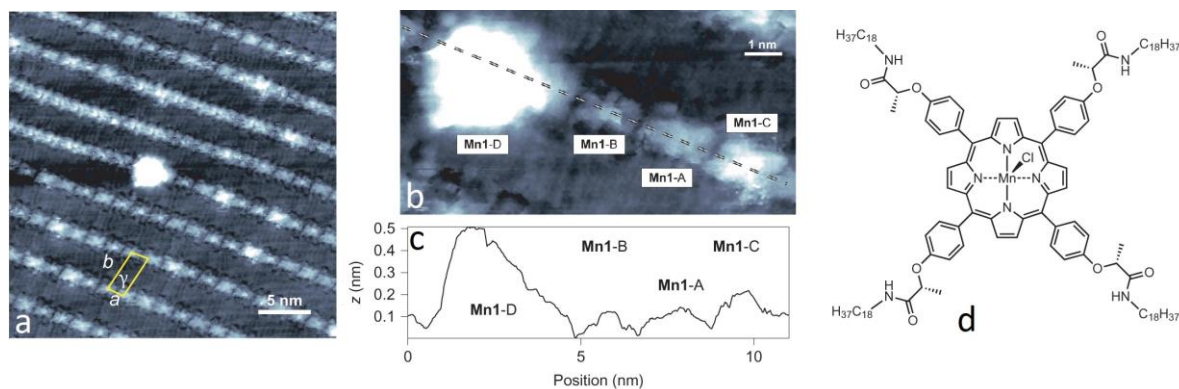
Figure 1.6 STM image of (a) ordered array of Mn–porphyrins (Mn1Cl in (d)) at the HOPG/1-octanoic acid interface under ambient conditions after 8h from the monolayer formation, V_b = -800 mV, I_t = 50 pA. (b) Magnification of (a) showing the evolution of the Mn-porphyrin centre during the reaction with O_2 (only the relevant intermediates of the multi-step reaction are shown below). (c) cross-sectional profile along the dashed line in (b). Adapted.[24]

Among the diverse class of 2D materials, hexagonal boron nitride (hBN) consists of an equal number of boron and nitrogen atoms arranged in a sp2-bonded honeycomb lattice which makes hBN isostructural and isoelectronic to graphene. However, due to the difference in electronegativity between boron and nitrogen, the material is a wide-band-gap insulator (Figure 1.7).[30, 31]
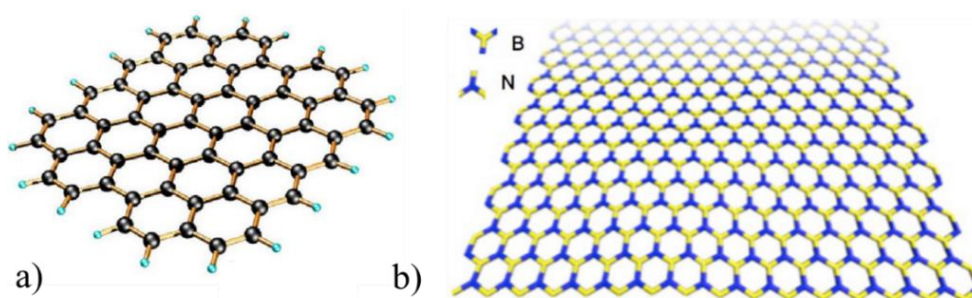
Figure 1.7. Hexagonal lattices of graphene (a) and boron nitride (b). Adapted.[30, 32]

Surfaces with insulating properties are generally unsuitable for electrochemistry as high electrical conductance is a necessary requirement. However, electrical interaction may occur when only few layers of the dielectric substrate are in contact with a metal conductor as the electronic wave function permeate the barrier.[33, 34] Therefore, for any

interactions occurring within such systems, careful considerations are required as the insulating properties of the thin layer are affected.[35] For instance, it has been reported how the gold electrode modified with insulating BN nanosheets becomes an efficient electrocatalyst for hydrogen evolution and oxygen reduction reactions.[36]

hBN monolayers are easily prepared by chemical vapor deposition on suitable single crystal metal surfaces. The reaction is self-terminated once the surface is covered as the metal catalyses the process. The final geometrical structure and electronic properties of the hBN monolayers are the result of the interaction with the metal substrate, allowing for considerable tunability. The unique characteristics of each 2D structure allow for tailored interactions with adsorbates and play a fundamental role in applications (e.g. catalytic activity, templating and self-assembly reactions).[30] The synthesis of boron nitride on rhodium single crystal leads to the spontaneous formation of a highly regular structure. The hBN/Rh(111), or boron nitride nanomesh, was discovered by the Greber group in the mid-2000s and its distinctive corrugated structure originates from the spatial mismatch between the hBN and metal lattices as 13 B or N atoms fit on 12 Rh atoms. The superstructure is formed by areas with stronger (pores) and weaker (wires) interactions between the monolayer and metal (Figure 1.8).[37, 38]
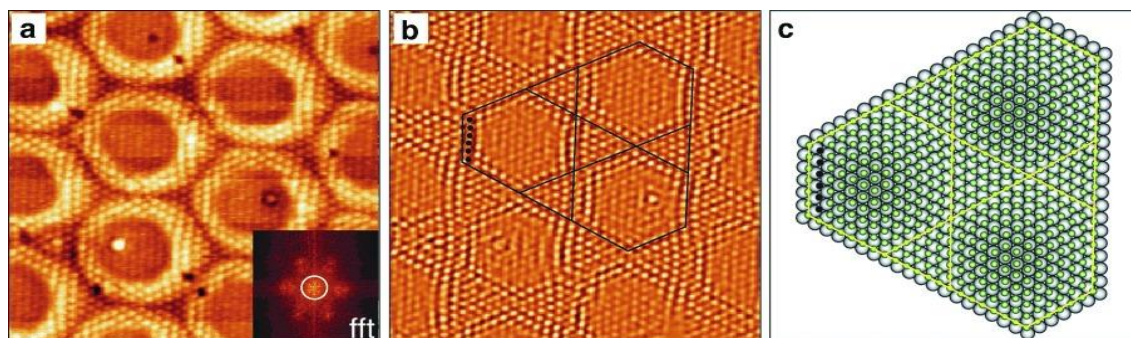
Figure 1.8 Atomic structure of the nanomesh. a) Constant-current STM image taken at 77 K (I_t = 1 nA, V_s = -2 mV, 10 x 10 nm^2). b) Shows the filtered a) to remove the 3.22 nm nanomesh periodicity and emphasise the atomic corrugation. c) Atomic model for the single layer nanomesh representing the N atoms (green spheres) for the area delimited by the black lines in b). Adapted.[38]

The lateral variation of the surface potential between pores and wires induces in-plane dipole rings. The strength of a single dipole ring is the equivalent of 5.5 water molecules oriented towards the centre of the pore. As a result, the nanomesh gives a templating

platform where atoms and molecules can be trapped with weak interactions and locked in a confined and ordered array (Figure 1.9). The molecules tend to be adsorbed at the edge of the pore where is located the maximum potential gradient (up to 1 Vnm^{-1}).[39]
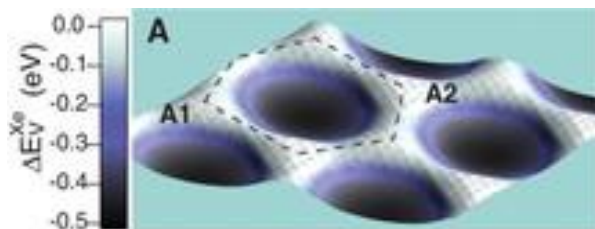
Figure 1.9. Energy landscapes of the hBN nanomesh. The variation in the potential is due to locally different charge transfer from the boron nitride and the metallic substrate and reflects the dipole rings. The potential in the holes is 0.5 eV lower. Adapted.[39]

The stability and trapping ability of the nanomesh have been extensively exploited for imaging different molecules not only in UHV, but also at room temperature, with remarkable detail thanks to the strong dipole rings effect which cannot be easily overcome by the thermal energy. Both computational simulation and experimental results showed the strong adsorption selectivity of the pores. The nanomesh allows to trap single porphyrins at the edge of the pores in UHV (Figure 1.10a). Despite the lower resolution due to molecular thermal agitation, the nanomesh is also capable of trapping porphyrins at room temperature (Figure 1.10b,c).[39, 40]
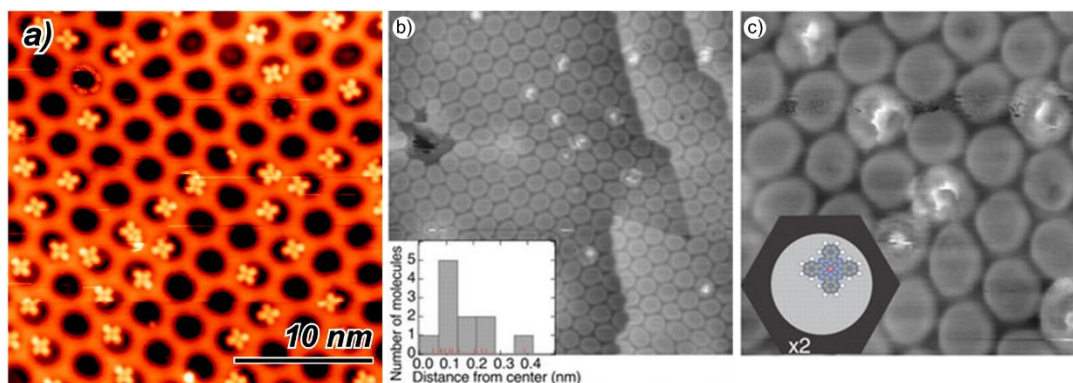
Figure 1.10. a) STM image of Cu-phthalocyanine at 5 K adsorbed on the hBN nanomesh (V_b = −0.525 V; I_C = 18 pA). (b) Room-temperature STM image (50 x 50 nm^2) of a low coverage of Cu-phthalocyanine trapped in the holes of the hBN nanomesh. V_b = 1.2 V, I_C = 30 pA. The inset shows the distribution of the distances of the molecular centre of gravity from the hole centre. (c) High-resolution image (18 x 18 nm^2). The inset shows a magnified model of the trapped Cu-phthalocyanine molecule. Adapted.[39, 40]

Despite its "templating" effect, the nanomesh is more broadly defined as an inert surface. Due to the insulating nature of the boron nitride layer, the nanomesh is capable of decoupling adsorbed molecules from the substrate, protecting from a strong interaction with the metal which would result in the re-hybridization of the frontier orbitals. Furthermore, the thin layer does not completely prevent influence from the metal, for instance, allowing the conductivity necessary for techniques such as scanning tunnelling microscopy.[41, 42] Unlike more conventional insulating materials (i.e. sodium chloride films) which have been used for imaging but are limited to UHV, the nanomesh stability was demonstrated within the electrochemical potential window of the water in aqueous electrolytes.[43] The nanomesh shows great stability in acidic environment as its potential window is approximately 1 volt, which is larger than that of the bare rhodium substrate. The potential window is limited by evolution of molecular hydrogen on the negative side and by oxidative removal of boron nitride on the positive side.[44] However, most of the investigations involving the nanomesh have been conducted in vacuum.[45, 46] The templating effect of the nanomesh has been investigated for electrochemical and self-assembly processes at the solid-liquid interface with STM imaging under potential control.[17, 43, 47] As a unique feature, electrochemical switching of the nanomesh corrugation by intercalation and deintercalation of atomic hydrogen has been demonstrated and linked to a change in adhesion properties of the interface (Figure 1.11) The macroscopic variation resulted from the variation in the lateral electric field of the in-plane dipole rings.[48]
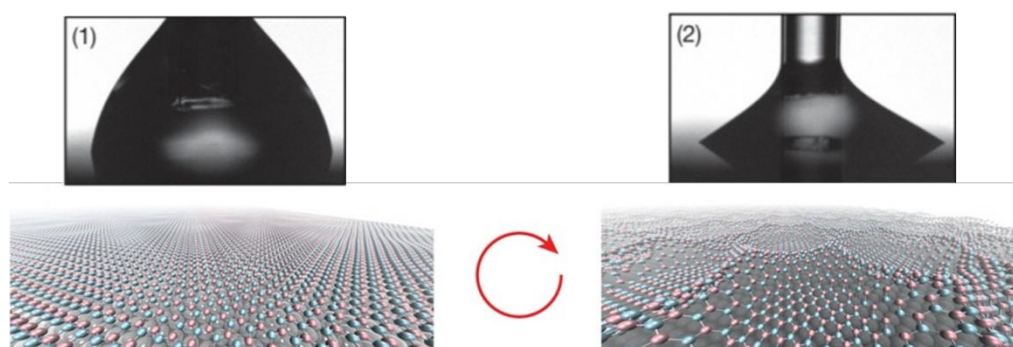
Figure 1.11. Advancing (1) and receding (2) angles of an electrolyte drop on hBN/Rh(111), from which the macroscopic effect of a change in nanomesh corrugation (microscopic change) can be inferred. Three-dimensional representation of the flat and corrugated h-BN layer (N, sky blue; B, pink; Rh, dark grey; H, white). Heights of N and B above the Rh top layer stretched by a factor of three. Adapted.[48]

Transition metal oxides (TMOs) have been extensively used for many applications, ranging from opto-electronics to energy materials, catalysis and sensing. [49, 50] The vast array of applications is attributable to their diversity in physical and chemical properties. The core of the TMOs tuneability is linked to the metal oxidation states which influences the electronic properties, allowing to range between metallic to wide-gap insulating behaviours.[51] TMOs are usually produced as thin film rather than low coverage distribution of isolated species on a solid substrate. The process required to synthetise isolated TMOs is more challenging as spontaneous uncontrolled polymerisation may occur.[52] Nevertheless, TMOs films play relevant role for electrodes or for charge generation and recombination materials due to their high work function, semiconduction properties and good transparency.[53]

Over the last decades, the interest on tungsten and molybdenum oxide materials grew considerably, reflecting their importance for distinctive applications as thin film catalysts (photo-, electro-, chemical) and semiconductor thanks to their large availability, low cost and reliability.[27, 51, 54, 55, 56] Recently, stable TMO clusters were isolated allowing a first understanding of their reactivity and difference in the reaction mechanisms of tungsten and molybdenum cluster oxide towards alcohol reactions.[57, 58, 59] The importance of such small cluster is related to their d-orbital based σ-aromaticity, observed for the first in 2005 following their generation in the gas phase (Figure 1.12). The analyses of the nature of the HOMOs related to the single and double anionic species revealed that they were all completely bonding three-centre σ-bonds, thus the d-orbitals from of transition metal atoms contributing in the σ-aromaticity of the clusters resulted in extra resonance energy stability of approximately 7.6 kcal/mol.[60, 61, 62, 63]
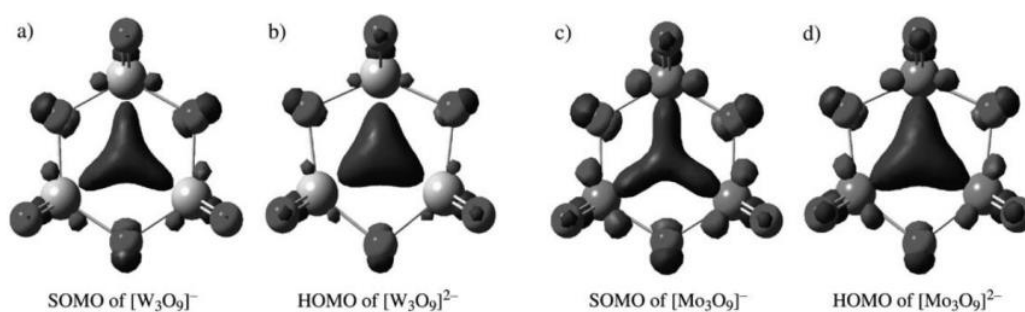
Figure 1.12. Singly occupied molecular orbital (SOMO) for $[W_3O_9]^-$ (a) and $[Mo_3O_9]^-$ (c) and highest occupied molecular orbital (HOMO) of $[W_3O_9]^{2-}$ (b) and $[Mo_3O_9]^{2-}$ (d). Adapted.[60]

Aims and objectives
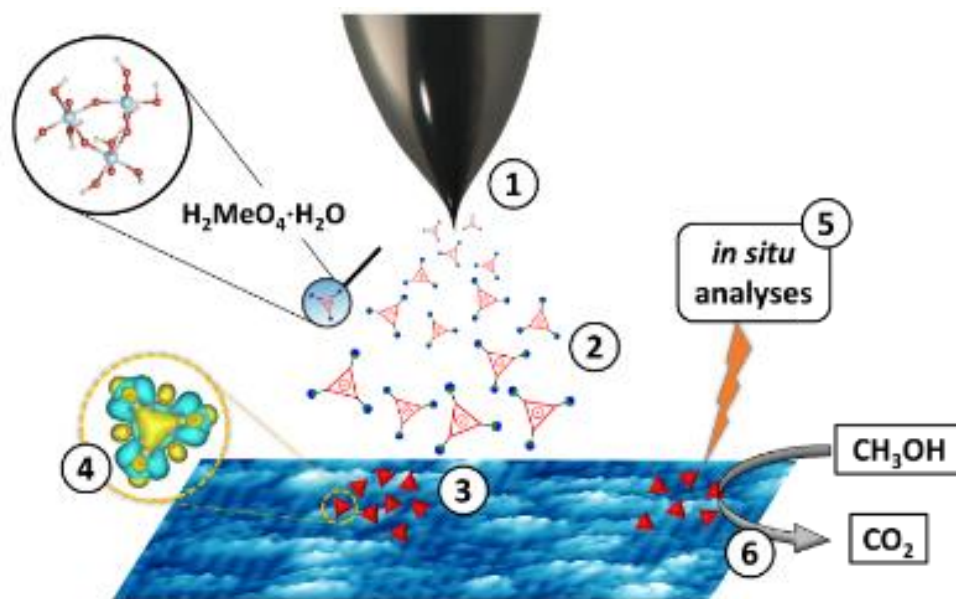
Figure 1.13. Approach followed in this thesis. ① Tungsten and molybdenum probes and 'electrochemical evaporators' for EC-STM. Characterisation of the oxide species ② in solution and ③ on the nanomesh. ④ High-resolution ⑤ *in situ* imaging and characterisation to allow for ⑥ *in operando* electrocatalytic reactions.

The objective of this thesis was the imaging with STM of early of transition metal oxide clusters monodisperse on boron nitride nanomesh under electrochemical conditions, and to study the effect of this substrate on the resolution that can be achieved. From previous work in the group,[64] we know that a tungsten STM tip in aqueous electrolyte spontaneously generates WO_3 species through a corrosion-like process and can therefore be considered as an 'electrochemical evaporator' for this species.[65] In order to broaden the scope of our study, we also investigated molybdenum tips for the same purpose – a metal from the same group as W that to our knowledge has never been used for EC-STM imaging as only recent papers reported its use limited to UHV conditions.[66, 67]

The thesis is divided into 3 main chapters:

In chapter 2, we study the electrochemical behaviour of both W and Mo metal (steps ① and ② in Figure 1.13) using cyclic voltammetry and impedance measurements to determine their stability regions as a function of pH and electrolyte composition. The results are compared with existing literature reports and the mechanism of the oxides formation are proposed.

Chapter 3 focusses on non-electrochemical techniques to characterise the formation of metal oxide clusters in solution (step ②) and their binding to the boron nitride nanomesh surface (step ③). In particular, we use inductively coupled plasma-optical emission spectroscopy (ICP-OES) to assess the concentrations of metal oxide that can be generated in solution and high-resolution mass spectrometry (MS) to gauge the likely composition of these clusters. We study the boron nitride nanomesh surface after exposure to the metal oxide clusters using *ex situ* X-ray photoelectron spectroscopy (XPS) and Raman spectroscopy, to independently evidence the presence of the clusters on the surface and to try and understand any changes in chemical nature compared to their native (solution-based) state.

Chapter 4 first documents the improvements we had to make to the Lancaster EC-STM setup to enable atomic resolution, and how we make and electrochemically insulate sharp W and Mo STM probes. We then discuss EC-STM imaging of metal-cluster-decorated hBN/Rh(111) surfaces (steps ④ and ⑤), using W and Mo tips and how different combinations (imaging W with Mo and *vice versa*) may help to increase our understanding. Finally, as an outlook, we discuss the possibility of studying electrocatalytic reactions (step ⑥) on these decorated hBN surfaces.

2 Electrochemical characterisation of tungsten and molybdenum

In this chapter we study the electrochemical behaviour of W and Mo as a function of pH and electrolyte composition to investigate the oxide evolution and determine experimental conditions in which the metals could behave similarly, as suggested from their thermodynamic properties.

2.1 Theorical background

In this section we introduce the fundamentals of electrochemistry derived from thermodynamic principles following the outline of Girault,[68] where a more comprehensive and detailed overview is provided. We define the principles of electrochemical processes at the solid/liquid interfaces from the definition of the electrochemical potential μ. Ultimately, the concepts of the main electrochemical techniques used in this work are described.

2.1.1 Electrochemical potential

The chemical potential μ of the species i is equal to the work necessary to transfer one mole of species i (n_i) from vacuum to a phase while keeping temperature T, pressure P and moles of component j (different from i) constant, except for the volume work.

$$\mu_i = \left(\frac{\partial G}{\partial n_i}\right)_{T,P,n_{j\neq i}}$$

(2.1)

with G Gibbs free energy.

The chemical potential describes the thermodynamic behaviour of chemical systems in equilibrium as it represents the available energy for the species i to undergo a chemical reaction or to move from one phase to another. In the case of charged species, the work necessary to transfer one mole of ions i from vacuum into a phase is added to the chemical potential (2.1). The electrostatic work $z_i F \phi$ is the result of two electrostatic terms: the first relates to the crossing of ions through a layer of oriented interfacial dipoles towards

the phase $z_i F \chi$, while the second term is associated with the charge of the phase itself $z_i F \psi$. Therefore, the electrochemical potential $\tilde{\mu}_i$ is

$$\tilde{\mu}_i = \mu_i^o + RT \ln a_i + z_i F \phi$$

(2.2)

with a activity of the species , F the Faraday constant (by definition $F = N_A \cdot e = 96485\ C/mol$ and N_A Avogadro constant and e elementary charge); $z_i F$ is the charge of one mole of ions; $\phi = \chi + \psi$, represents the inner electrostatic potential, the sum of the effect of the surface (χ) and the outer (ψ) potentials.

The standard electrochemical potential, which to an extent is independent of the concentration is defined as

$$\tilde{\mu}_i{}^\circ = \mu_i^o + z_i F \phi$$

(2.3)

added to the variation of internal energy

$$
\begin{aligned}
dU &= -P\,dV + T\,dS + \Sigma_i \tilde{\mu}_i\,dn_i \\
&= -P\,dV + T\,dS + \Sigma_i (\mu_i + z_i F \phi)\,dn_i \\
&= -P\,dV + T\,dS + \Sigma_i \mu_i\,dn_i + \Sigma_i \phi\,dq_i
\end{aligned}
$$

(2.4)

$\phi\,dq_i$ defines the work associated with the charges addition to a phase having inner potential ϕ.

Hence, the general definition of electrochemical potential is related to the work necessary to move one mole of ions from a vacuum to a charged phase, while pressure and temperature are constant

$$\tilde{\mu}_i = \left(\frac{\partial \tilde{G}}{\partial n_i} \right)_{T,P,n_{j \neq i}}$$

(2.5)

However, it only represents an abstract notion, it cannot be determined experimentally because it is impossible to add ions into a phase without changing its charge.

2.1.2 Redox reactions

Redox (short for reduction-oxidation) reactions involve the transfer of electrons between two species. The process can be separated in two reactions as one reactant loses electrons (oxidation), while the other species gains electrons (reduction). In the electrochemical cell, the electrons are exchanged between the species and the electrodes and the equilibrium of the redox reaction can be controlled. Figure 2.1 shows a generic electrochemical equilibrium of a redox reaction in the solution S at a metal electrode M

$$Ox^S + ne^{-M} \leftrightharpoons Red^S$$

(2.6)
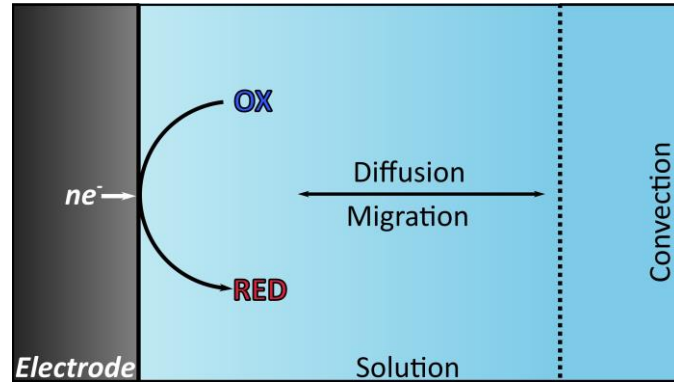
Figure 2.1. Diagram of a generic redox reaction occurring at the metal electrode when the movement of chemical species to (and from) the surface of the electrode is governed only by diffusion.

The equilibrium can be described as a linear combination of electrochemical potential of the reactant species, the electrochemical Gibbs energy, as

$$\Delta\tilde{G} = \tilde{\mu}_{red}^S - (n\tilde{\mu}_{e^-}^M + \tilde{\mu}_{ox}^S) = 0$$

(2.7)

combined with (2.2) becomes

$$\left[\tilde{\mu}_{red}^{o,S} + RT\ln a_{red}^S + z_{red}F\phi^S\right] - n[\tilde{\mu}_{e^-}^M - F\phi^M] - \left[\tilde{\mu}_{ox}^{o,S} + RT\ln a_{ox}^S + z_{ox}F\phi^S\right] = 0$$

(2.8)

with $\tilde{\mu}_i^{o,S}$ the standard chemical potential of the species i in solution and a_i^S the activity of i in the molarity scale.

As the electron exchanged during the reaction are $n = z_{ox} - z_{red}$, (2.8) becomes

$$nF(\phi^M - \phi^S) = (\tilde{\mu}_{ox}^{o,S} - \tilde{\mu}_{red}^{o,S} + n\tilde{\mu}_{e^-}^M) + RT\ln\left(\frac{a_{ox}^S}{a_{red}^S}\right) = -\Delta G^o + RT\ln\left(\frac{a_{ox}^S}{a_{red}^S}\right) = -\Delta G$$

<div align="right">(2.9)</div>

with ΔG^o is the standard Gibbs energy, a ΔG represents the chemical contribution of Gibbs energy of the reduction of the species O into R at the electrode. $\phi^M - \phi^S$ is the Galvani potential and the term $F(\phi^M - \phi^S)$ describes the electrical work necessary to transfer one mole of elementary charge from inside the metal electrode to the bulk of the solution.

For the redox reaction (2.6) the equilibrium constant is

$$K_e = \frac{a_{red}^S}{a_{ox}^S} = exp\left(\frac{-\Delta G^0}{RT}\right) exp\left(\frac{-nF(\phi^M - \phi^S)}{RT}\right)$$

<div align="right">(2.10)</div>

The equilibrium constant is a function of the inner potential between the electrode and the solution. Therefore, is possible to impose a Galvani potential difference with a potentiostat and affect the ratio of the activities of the species in solution.

2.1.3 Nernst Equation, Standard reduction potential

For the electrochemical reaction in the cell, the Gibbs energy is

$$\Delta_r G = \Delta_r G^o + RT \ln Q = -nFE_{cell}$$

<div align="right">(2.11)</div>

with Q reaction quotient, the ratio between the activities of products and reagent.

By rearranging the terms in (2.11) the equation for the cell potential in terms of the composition, known as Nernst equation

$$E_{cell} = E_{cell}^o + \frac{RT}{nF}\ln Q$$

<div align="right">(2.12)</div>

with E_{cell}^o the standard cell potential.

The Nernst equation describes the relation of the potential difference between two electrodes, the working electrode (WE) at which the redox reaction occurs, and the

reference electrode (RE). It was first defined experimentally. By convention, the origin of the scale is defined in terms of the standard hydrogen electrode (SHE) (2.1.4)

$$E_{SHE} = [E^o_{ox/red}]_{SHE} + \frac{RT}{nF} lnQ$$

(2.13)

Therefore, the standard reduction potential for the reduction of a proton in water is equal to zero, at all temperatures

$$\left[E^o_{H^+/\frac{1}{2}H_2}\right]_{SHE} = 0\ V$$

(2.14)

To avoid relying on activities and to use experimental quantities that can be directly measured, the formal reduction potential is defined as

$$\left[E^{o\prime}_{ox/red}\right]_{SHE} = [E^o_{ox/red}]_{SHE} + \frac{RT}{nF} ln\left(\frac{\gamma_{ox}}{\gamma_{red}}\right)$$

(2.15)

Allowing to express the Nernst equation (2.13) in a form related directly to experimental conditions

$$E_{SHE} = \left[E^{o\prime}_{ox/red}\right]_{SHE} + \frac{RT}{nF} ln\left(\frac{c_{ox}}{c_{red}}\right)$$

(2.16)

with c_i concentration of the species i in solutions. The formal reduction potential tends to the standard reduction potential for diluted solutions as the activity coefficient tends to 1.

2.1.4 Reference electrodes

From the Nernst equation (2.13) is impossible to measure the absolute value for the Galvani potential ($\phi^M - \phi^S$) of a half-cell reaction. Therefore, the potential is indirectly measured against a reference electrode with a voltmeter by the passage of a small current – practically zero – that no net electrode reactions can take place to disturb its equilibrium. The RE has to generate a stable Nernst potential, therefore the activity ratio of the oxidised and reduced species have to be constant. This is achieved in practice by using

electrodes capable of keeping a constant composition. Last, a fast electron transfer kinetic is required to maintain the thermodynamic equilibrium.

$$Measured\ potenital\ difference = \ (\phi^M - \phi^S)_{WE} - (\phi^M - \phi^S)_{RE}$$

(2.17)

Standard hydrogen electrode

By convention, the electrode potential scale origin is based on the standard hydrogen electrode (SHE). The SHE potential is determined with a platinized platinum electrode in contact with a solution of hydrogen ions at a standard pressure and concentration. In practice, the hydrogen is constantly bubbled through the acid solution with a pH of zero. The fugacity of the gas remains at standard pressure of 1 bar. To ensure the inner potentials are the same, the acid solution and the working electrode solution are physically separated, and the circuit is completed with a salt bridge. The redox reaction taking place at the reference electrode is

$$\frac{n}{2} H_2 \rightleftharpoons nH^+ + ne^-$$

(2.18)

As the SHE is complicate to use in practical, other RE are commonly adopted, in particular:

Reversible hydrogen electrode

The reversible hydrogen electrode (RHE) is a simpler and more convenient RE to use. The electrode is in direct contact with the solution where the redox reaction is taking place. The redox reaction on the RHE is analogous to that of the SHE (2.18) as they both occur on a platinum electrode in contact with trapped hydrogen and an electrolyte. However, the potential of the RHE is pH-dependent, as it is affected by the proton activity of the solution

$$[E_{RHE}^o]_{SHE} = \left[E_{H^+/\frac{1}{2}H_2}^o\right]_{SHE} + \frac{RT}{F} ln a_{H^+} = 0\ V - 0.0059\ V \cdot pH$$

(2.19)

Silver-silver chloride electrode

The silver-silver chloride electrode is another commonly used RE as it is reliable and accurate. This electrode consists of a silver coated with silver chloride and immersed in an electrolyte solution. The electrolyte solution is typically a potassium or sodium chloride (saturated) solution with a constant ionic strength. The potential of the silver chloride electrode is determined by the equilibrium between the silver and chloride ions in the electrolyte solution. Hence, the equilibrium

$$AgCl + e^- \rightleftharpoons Ag + Cl^-$$

(2.20)

is practically controlled by the concentration of the chloride ions, related to the solubility product of silver chloride

$$K_S = \frac{a_{Ag^+} \cdot a_{Cl^-}}{a_{AgCl}} = a_{Ag^+} \cdot a_{Cl^-} = 1.77 \cdot 10^{-10}$$

(2.21)

$$\left[E^o_{Ag|AgCl}\right]_{SHE} = \left[E^o_{Ag^+/Ag}\right]_{SHE} + \frac{RT}{F} lnK_S = 0.223 \, V$$

(2.22)

As the electrode potential is stable and the pH does not affect its potential, the silver chloride electrode can be used in both alkaline and acidic solutions. The electrode solution is separated from the WE solution through a liquid junction.

Pt quasi reference electrode

In some cases, due to specific conditions or experimental setups, the use of a standard reference electrode may not be possible, and quasi-reference electrodes (QREs) are used as an alternative. However, QREs are not stable, and their reference potential may not be predictable. For instance, in EC-STM (4.1.2), a simple platinum wire is often used as QRE as it is small enough to fit into the cell. Unfortunately, the potential of the platinum QRE can fluctuate over time and its uncertainty becomes more significant with an increase in the pH of the electrolyte (Figure 2.2).
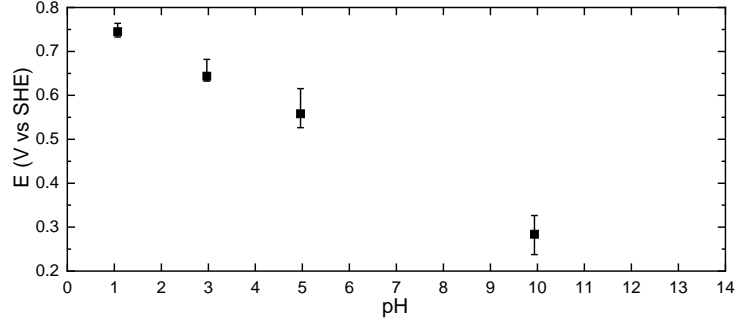
Figure 2.2. Pt electrode potential (vs SHE) as a function of pH, adapted.[69]

2.1.5 Mass transport

For electrolyte solutions two type of mass transport are considered: thermal (or mechanical) convection and transport driven by a Gibbs energy gradient. The diffusion flux vector $\boldsymbol{J}_i$ describes the transport of species i under the influence of an electrochemical potential gradient

$$\boldsymbol{J}_i = -c_i \tilde{u}_i \boldsymbol{\nabla} \mu_i - z_i F c_i \tilde{u}_i \boldsymbol{\nabla} \phi$$

(2.23)

With c_i molar concentration, $\tilde{u}_i$ electrochemical mobility (always positive for cations and anions by definition), represents the ratio of the velocity to the driving force, $\boldsymbol{\nabla}$ gradient.

The equation is not only limited to transport under gradients of chemical and electrical potential, other forces (i.e., pressure, gravitational or centrifugal) can be similarly included in (2.23) when required. An electrical potential gradient (electric field) affects only ions and not uncharged species. In real conditions, the presence of supporting electrolyte eliminates possible electric fields in the bulk of the solution but not in the electrode proximity.

When diffusion is driven solely by concentration gradients, in the absence of thermal or mechanical agitation, Fick's first law applies: the diffusion flux is directly proportional to the concentration gradient

$$J_i = -D_i \left(\frac{\partial c_i}{\partial x} \right)$$

(2.24)

with D_i diffusion coefficient. In the interface proximity, between the electrode and the solution, a thin liquid layer is stagnant. It is called diffusion layer and its thickness is in the order of micrometres.

Fick's second law describes the dynamic changes in the concentration over time,

$$\left(\frac{\partial c_i}{\partial t}\right)_x = \left(\frac{\partial J_i}{\partial x}\right)_t$$

(2.25)

in the case of a planar interface and by using (2.24) it becomes

$$\frac{\partial c_i}{\partial t} = D_i \frac{\partial^2 J_i}{\partial x^2}$$

(2.26)

allowing to predict the variation of the concentration close to the electrode surface.

2.1.6 Electrochemical kinetics

In Figure 2.1 the electrons generated from the redox reaction drive the flow of electrical current I through the electrode, related to the flux of reactant and undergoing electrolysis

$$I = FAJ = FAk^n[reactant]_0^n$$

(2.27)

with F Faraday constant, A electrode area, J flux of the species, it is a measure of the rate of the heterogeneous interfacial electrochemical reaction with k^n the nth order rate constant, n the order of the reactant, commonly n = 1. The concentration of the reactant is in proximity of the surface, the subscript "0" discriminates from the concentration in bulk solution.

When is applied to electrode a potential more positive than the equilibrium value, the reduced species undergo oxidation at the working electrode. The transfer of electrons from the reduced species to the electrode generates an anodic current, denoted as I_a (2.27). The current represents the rate at which electrons are transferred per second, and it is proportional to the interfacial concentration of the reduced species according to a first-order reaction

$$I_a = nFAk_a[RED]_0$$

(2.28)

Similarly, when a more negative potential is applied the resulting cathodic current I_c

$$I_c = -nFAk_c[OX]_0$$

(2.29)

with k_a and k_c electrochemical rate constants for oxidation and reduction respectively.

At equilibrium, the rates of reduction and oxidation are equivalent. Assuming that mass transfer occurs quickly in comparison to the kinetics of the electron transfer reaction, the concentration of species at the bulk and the surface are also equivalent

$$[RED]_0 = [OX]_0 = [RED]_\infty = [OX]_\infty$$

(2.30)

In this case $k_a = k_c = k^0$, with k^0 standard rate constant that can be written as

$$k^0 = \delta \left(\frac{kT}{h}\right) e^{\frac{-\Delta G_{act}^0}{RT}}$$

(2.31)

with δ approximal to the minimum distance between reactants and electrode, k Boltzmann constant, h Plank constant, and ΔG_{act}^0 standard Gibbs activation energy of the electron transfer reaction.

For a general case $[RED]_\infty \neq [OX]_\infty$, the activation barrier is not symmetrical at the equilibrium, the anodic and cathodic activation energies are different, therefore $k_a \neq k_c$. At the equilibrium the rates of oxidation and reduction are equal $(k_a[RED]_0 = k_c[OX]_0)$, therefore the respective rate constants cannot be identical (Figure 2.3).
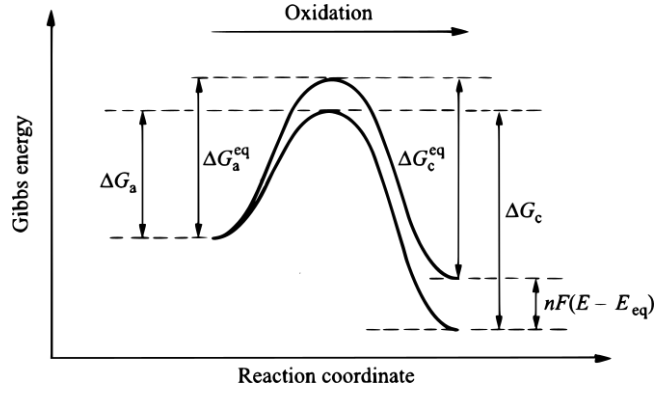
Figure 2.3. Effect of the working electrode polarisation over the activation energy for a generic redox reaction. Adapted.[68]

An increase to the electrode potential by applying $(E - E_{eq})$ the anodic and cathodic activation energies become

$$\Delta G_a = \Delta G_a^{eq} - \alpha nF(E - E_{eq})$$

(2.32)

$$\Delta G_c = \Delta G_c^{eq} + (1 - \alpha)nF(E - E_{eq})$$

(2.33)

with α the charge transfer coefficient.

From (2.31), (2.32), and (2.33) the variation of the anodic and cathodic rate constant can be expressed as a function of the electrode potential as

$$k_a = k_a^0 e^{\frac{\alpha nFE}{RT}}$$

(2.34)

$$k_c = k_c^0 e^{-(1-\alpha)nFE/RT}$$

(2.35)

At the formal redox potential $E^{0\prime}$, the activation barrier is symmetrical, k_a^0 and k_c^0 are related to the standard rate constant $k^{\ominus}$

$$k^{\ominus} = k_a^0 e^{\frac{\alpha nFE^{0\prime}}{RT}} = k_c^0 e^{\frac{-(1-\alpha)nFE^{0\prime}}{RT}}$$

(2.36)

The total current generated as a function of the applied potential perturbation with respect to the equilibrium, or η the overpotential $(\eta = E - E_{eq})$ is

$$I = I_0 \left[\frac{[RED]_0}{[RED]_\infty} e^{\frac{\alpha nF\eta}{RT}} - \frac{[OX]_0}{[OX]_\infty} e^{\frac{-(1-\alpha)nF\eta}{RT}} \right]$$

<div align="right">(2.37)</div>

with I_0 exchange current equal to

$$I_0 = nFAk^\ominus [RED]_\infty^{1-\alpha} [OX]_\infty^\alpha$$

<div align="right">(2.38)</div>

If the current at the electrode is small and the mass transfer is rapid, the concentration at the surface can be approximated to be equal to the concentration in the bulk solution (constant for large volumes). Under these conditions, the equation (2.38) is simplified to

$$I = I_0 \left[e^{\frac{\alpha nF\eta}{RT}} - e^{\frac{-(1-\alpha)nF\eta}{RT}} \right]$$

<div align="right">(2.39)</div>

known as the Butler-Volmer equation, with the first exponential related to anodic currents and the second to cathodic currents. The equation can be expressed as exchange current density $j_0 = I_0/A$, the logarithmic of its absolute value j plotted as a function of the overpotential η is known as Tafel plot and allows to evaluate the rate determining steps in the reaction and to determine by graphical extrapolation the Tafel slopes for $\eta = 0$ V, useful to calculate the value of the charge transfer coefficients.

2.1.7 Three-electrode cell and potentiostat

To allow the passage of the electrical current, a second electrode must be present and connected through an external circuit. However, to study electrode kinetics a three-electrode configuration is required. This configuration comprises of a working electrode, where the electrochemical reaction takes place, a reference electrode used to measure potential, and a counter electrode (CE) which completes the circuit and enables the electrons to flow. To control the electrode potential, a potentiostat is used to apply a voltage between the WE and RE, and the resulting current flow is then measured between the WE and CE (Figure 2.4).
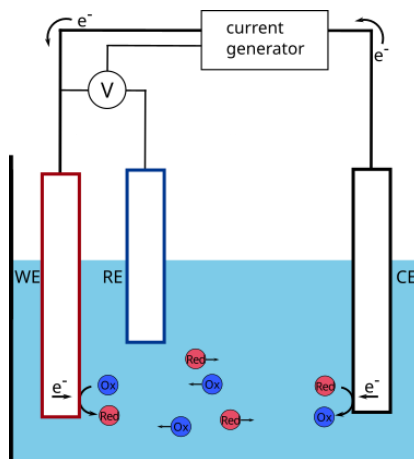
Figure 2.4. Diagram of a three-electrode electrochemical cell. The WE is controlled with the potentiostat relatively to the RE. The current flows via ionic conduction between the WE and the CE. The electrochemical reactions transfer the charge from the electrolyte and the electrode.

In a three-electrode configuration, the working, reference, and counter electrodes are connected to an external device which controls voltage and current: the potentiostat/galvanostat (Figure 2.5).
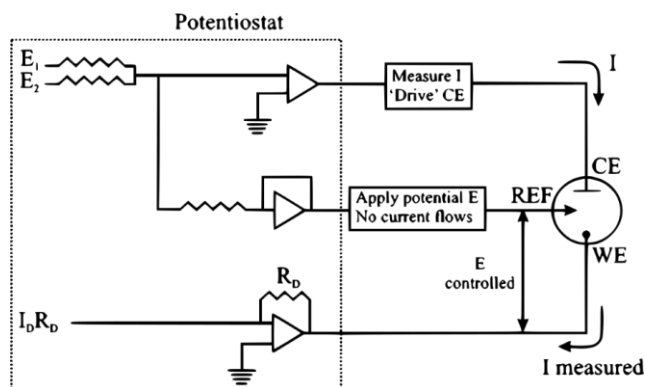
Figure 2.5. Block diagram of the potentiostat connected to a 3-electrode setup in the electrochemical cell (circle). All the resistances are equal but R_D, which is variable. Adapted.[70]

In potentiostatic mode, the voltage is controlled and measured between the WE and RE using a control amplifier and the resulting current flows between the WE and CE is measured. The voltage is controlled through a negative feedback loop within the control amplifier which adapts its output based on the potential measured at the RE, enabling accurate measurements of current at set voltage conditions. In contrast, the galvanostatic mode controls the current flow and measures the voltage output.

The resistance of the electrolyte solution R_s between WE and RE is responsible for the *ohmic drop*, resulting in a difference between applied and measured potentials

$$E_{applied} = E_{meaured} + IR_s$$

(2.40)

with I the current flowing between the WE and RE.

In a two-electrode setup the ohmic drop contribution is generally substantial, whereas its effect is usually negligible in a three-electrode configuration for WE and RE in close proximity (Figure 2.4). Impedance spectroscopy allows to measure directly the value of the solution resistance.

The techniques used in this work are based on potentiostatic modes, including open circuit voltage (OCV), cyclic voltammetry (CV), chronoamperometry (CA), and electrochemical impedance spectroscopy (EIS).

2.1.8 Cyclic voltammetry

Cyclic voltammetry is an electrochemical technique used to investigate the redox behaviour of chemical species in solution. The method involves sweeping the potential of the working electrode linearly between two limits, initial E_i and final E_f potentials, while recording the current response. The direction of the potential sweep determines whether oxidation or reduction reactions are promoted, upon reversing the scan direction, the opposite reduction or oxidation reaction being promoted. The current generated is influenced by time and the scan rate v of the applied potentials, their control allows to obtain information about the kinetics of the redox reaction

$$E(t) = E_i \pm vt$$

(2.41)

The current resulting from a CV experiment is measured and plotted against the potential applied. The area under the CV curve, which is proportional to the scan rate, provides information about the charge transferred during the redox reaction. The cyclic voltammogram gives insights about the redox behaviour of species in a solution, providing information on the oxidation potential, reduction potential, and the number of electrons involved in the reaction. Moreover, the peak currents and potential positions of

the oxidation and reduction peaks allow to determine information on the kinetics and thermodynamics of the redox process. Figure 2.6 shows a generic CV for a redox reaction at different scan rates and the effect of stirring (constant diffusion layer vs. time-dependant decrease of the diffusion layer).
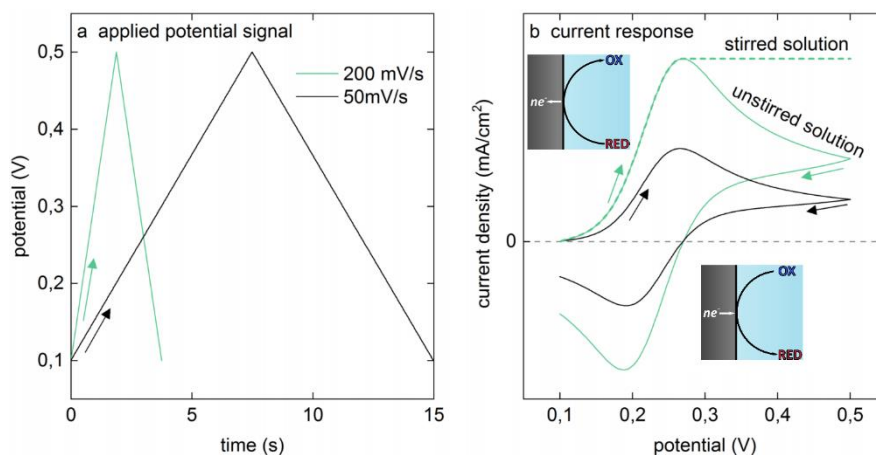
Figure 2.6. Cyclic voltammograms of a redox reaction at two different scan rates (green 200 mV/s, black 50 mV/s). a) Applied potential signal and b) Faradaic current response for stirred solution (green dashed line) with constant diffusion layer thickness and resulting current limit; and unstirred solutions (solid lines) with time-dependent decrease of diffusion layer thickness and subsequent current peaks.

Cyclic voltammetry can also provide valuable insights not only into Faradaic processes, which involve electron transfer, but also into non-Faradaic processes. These processes include a variety of reactions and changes that occur at the electrode surface, such as adsorption/desorption of species, morphological changes, and variations in electrolyte concentration or pH. Non-Faradaic processes can contribute to the current-voltage response obtained from a CV experiment, especially at low scan rates. To distinguish the contribution between Faradaic and non-Faradaic processes, ones may perform experiments at different scan rates. Non-Faradaic processes tend to produce broad, featureless background currents that do not vary significantly with scan rate, making them distinguishable from the sharper and more pronounced peaks of Faradaic processes.

2.1.9 Electrochemical impedance spectroscopy

Electrochemical impedance spectroscopy (EIS) is an alternating current (AC) technique useful for the description of the surface interface and the electrochemical

processes occurring on it. In a potentiostatic EIS experiment, on the assumption the system remains stable (i.e., steady-state or time-invariant), a small amplitude AC signal is superimposed to the DC potential perturbation applied to the electrochemical cell. The resulting AC current response is related to the AC potential perturbation. The analysis of the impedance spectra as a function of the AC frequency with a suitable model provides quantitative parameters of the process occurring on the studied electrode surface, which can be further characterised by studying the evolution of these parameters with the DC potential.

The transition from the time domain of the classical direct current (DC) techniques to the frequency domain of the EIS allows to overcome some limitations by separating the different contributions to the electrochemical response of the interface, such as double layer charge, mass transport, and any other electrical process including electron transfer and chemical reactions. The EIS is therefore capable of differentiating between the kinetics of an electrode reaction from experimental artifacts, such as ohmic drop.[71, 72, 73]

The sinusoidal potential $E(t)$ applied during a potentiostatic EIS measurement is

$$E(t) = E_0 \sin(\omega t)$$

(2.42)

with E_0 potential sine wave amplitude, $\omega = 2\pi f$ angular/radial frequency, t time. The amplitude and the frequency of the input potential signal are controlled with a potentiostat or frequency response analyser (FRA). The measured output current signal $i(t)$ has the same frequency as the input signal but the phase of the waveform ωt shifted by a finite amount ϕ, phase shift/angle.

$$I(t) = I_0 \sin(\omega t - \phi)$$

(2.43)

The EIS measures the impedance response of a system to an applied sinusoidal potential signal. This potential signal is centred around a fixed potential value, and a sequence of sinusoidal signals with constant amplitude is applied. The frequency of each signal is then varied, typically using an equally spaced descending logarithmic scale. The frequency range for EIS measurements typically ranges from 10^6 Hz to 10^{-2} Hz, although the exact upper and lower limits may be influenced by factors such as the system

under investigation, the diffusion properties, and the sensitivity of the instrumentation used. The time dependant potential and current data for each frequency are converted with a fast Fourier transform (FFT) to frequency dependant potential and current magnitude.

Analogous to Ohm's law the impedance $Z(\omega)$ is

$$Z(\omega) = \frac{E(t)}{I(t)} = |Z|e^{j\phi} = |Z|(\cos\phi + i \cdot \sin\phi) = Z_r + iZ_i$$

(2.44)

With i imaginary unit ($i^2 = -1$), the impedance magnitude $|Z| = \frac{E_0}{I_0}$, the real (Z_r) and imaginary (Z_i) separated components of the impedance.[74, 75]

The impedance, as is a transfer function, allows comparison between different system, i.e. electrochemical system and electrical circuits, as they behave similarly. Therefore, is possible to model the different parts of an electrochemical system with simpler circuit elements where the impedance is well-characterised. The main passive element, as they do not generate current or potential, are:

The impedance for a *resistor* (R) (2.45) is not affected by the phase, it is equal to the value of the resistance R

$$Z_R = R$$

(2.45)

Figure 2.7. Resistor element for an equivalent circuit.

Example of common resistor for electrochemical system are the uncompensated solution resistance, or the charge transfer resistance from the electron transfer across an interface associated with Faradaic processes.

The impedance for a *capacitor* (C) (2.46) is inversely proportional to the frequency

$$Z_C = \frac{1}{j\omega C} = \frac{-j}{\omega C}$$

(2.46)

Figure 2.8. Capacitor element for an equivalent circuit.

It is usually associated with non-Faradaic processes such as double layer capacitance.

The *Warburg element* (W, Wb) (2.47) impedance is

$$Z_{W_b} = \frac{W}{(j\omega)^{0.5}}$$

(2.47)
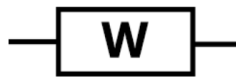
Figure 2.9. Warburg element for an equivalent circuit.

The Warburg element it is usually associated to the diffusion of electron or ions in solid or liquid phases.

The impedance for an *inductor* (L) (2.48) is function of the frequency

$$Z_L = j\omega L$$

(2.48)

Figure 2.10. Inductor element for an equivalent circuit.

It represents magnetic inductance therefore is generally not present in electrochemical system, however the wires connecting the cell to the potentiostat can generate inductance artefacts.

The *constant phase element* (CPE, or Q) (2.49) describes the behaviour of non-ideal equivalent elements. The impedance for a CPE is

$$Z_{CPE} = \frac{1}{(j\omega)^{\alpha}Q}$$

(2.49)

Figure 2.11. Constant phase element for an equivalent circuit.

The CPE becomes equal to a resistor when $\alpha = 0$, a capacitor when $\alpha = 1$, a Warburg element for $\alpha = 0.5$, and inductor when $\alpha = -1$.

The impedance of a redox couple in solution in presence of a planar electrode is represented by a simple RC model, the Randles equivalent circuit. From the surface of the electrode, two contributions to the current are distinguished, the non-Faradaic double layer capacitance originated from the adsorbed species on the surface and the Faradaic current contribution associated with the electron transfer reaction. These are represented respectively with a capacitor in parallel to the resistor. Often a Warburg element is added in series to the resistor to account for diffusion of the redox species from the electrode. Last, the solution resistance is accounted with a resistor connected in series to the other elements (Figure 2.12).
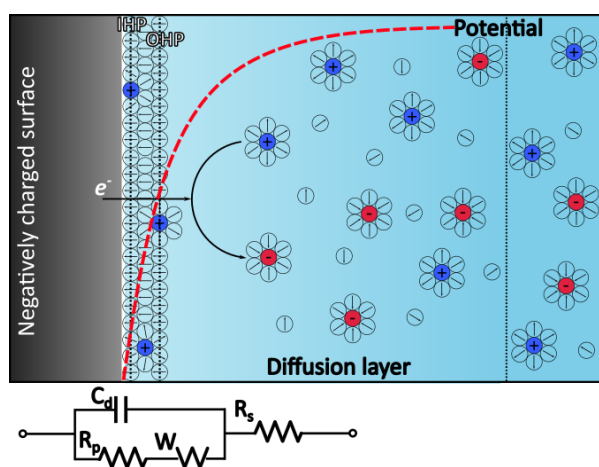
Figure 2.12. Schematic of the redox process occurring at the electrode and associated Randles equivalent circuit. The positively charged oxidants (blue) are diffusing towards the negatively charged electrode, they accept the electrons from the electrode at the interface and become reductants (red). The negatively charged species diffuse to the bulk of the solution. The inner (IHP) and outer Helmholtz-plane (OHP) are represented alongside the potential drop from the electrified interface. The physical components in the equivalent circuit represent the relative process occurring at the interface and in the solution during the electrochemical reaction. Double layer capacitance (C_d), charge-transfer resistance (R_p) Warburg impedance (W), and solution resistance (R_s). Adapted.[74]

2.1.10 Pourbaix diagrams

Pourbaix (or potential-pH) diagrams are graphical representation of the thermodynamic stable phases for an aqueous electrochemical system as a function of pH. The boundaries, represented with lines, identify the equilibrium of a redox or an acid-base reaction between two species. As they describe the thermodynamic system, no kinetic aspects are considered. Pourbaix diagrams are generally used to predict the behaviour of metals (and their alloys) in the aqueous environment (i.e., condition for corrosion or electrochemical experiments). Figure 2.13 shows the qualitative plot for tungsten and molybdenum (more detailed diagrams of the metals are in shown in Figure 2.15 and Figure 2.18).
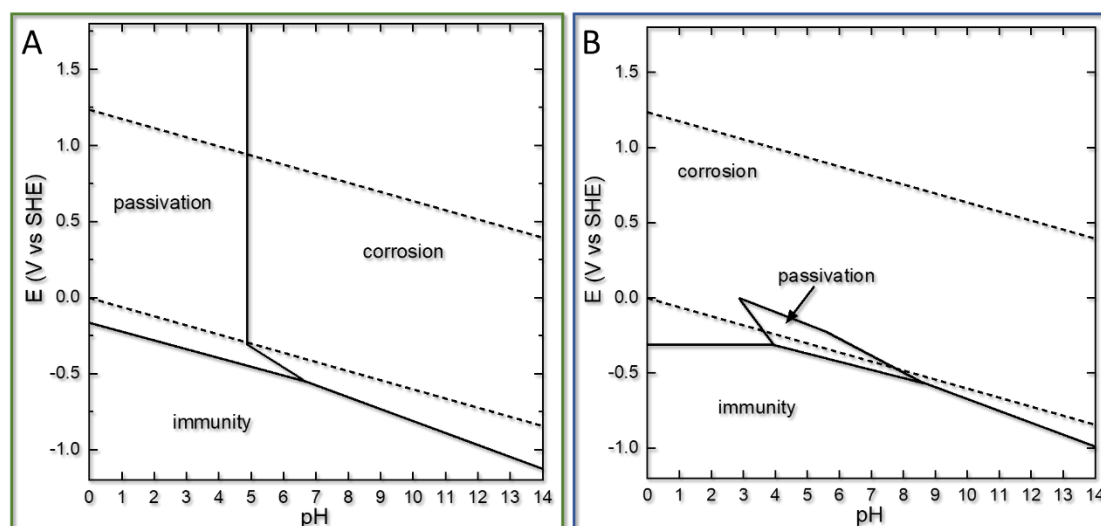
Figure 2.13. Pourbaix diagrams of (A) tungsten and (B) molybdenum (calculated for an analytical concentration in the respective solution of 10^{-4} M). Dashed black lines indicate the thermodynamic stability region of water. The continuous black lines define the boundaries in which the outlined process is thermodynamically favoured. Adapted.[76]

2.2 Experimental details

The electrolyte solutions were prepared by dilution using Milli-Q® ultrapure water (resistivity 18.2 MOhm·cm, total organic carbon 2 ppb). Perchloric acid (70%, purity 99.99%, Thermo Fisher), sulfuric acid (Suprapur 96%, Supelco), formic acid (98%, Honeywell), sodium perchlorate monohydrate (Normapur 99.1%, VWR), sodium hydroxide solution (5 M, Sigma-Aldrich), ammonia solution 25% (Emsure ISO, Reag Ph Eur, Supelco) were used as received.

As working electrode, tungsten (99.95%, annealed, diameter 0.25 mm, Advent UK) or molybdenum (99.95%, annealed, diameter 0.25 mm, Advent UK) wires were used after polishing with sandpaper (grit P8000) and rinsing with Milli-Q® ultrapure water using filter paper (grade 1, Whatman) to remove any residue.

As reference electrode, it was used either a reversible hydrogen electrode ($E_{RHE} = (-0.059 \times pH)\, V\, vs\, SHE$) or a silver/silver chloride (in NaCl 3 M) $E_{Ag\,AgCl} = 0.209\, V\, vs\, SHE$.

The three-electrode cell configuration was finalised with a gold wire as counter electrode. All the glassware was cleaned using boiling nitric acid 20% (diluted from >65% reagent grade, Sigma-Aldrich), followed by a thorough rinsing with Milli-Q® ultrapure water.

All electrochemical measurements were carried with a BioLogic BP-300 potentiostat controlled with its proprietary software (EC-Lab v11.43). All electrochemical potentials are reported versus the silver/silver chloride (in NaCl 3 M).

Impedance spectra were measured with a BioLogic BP-300 potentiostat in single sine mode at E=0 V vs OCP, a scan range from 100 kHz to 50 mHz with 8 points per decade in logarithmic spacing. Impedance spectra were fitted with EC-Lab (v11.43, BioLogic) and AfterMath (v1.6, PINE research) software.

2.3 Results and discussion

In this section, the electrochemical behaviour of metallic tungsten and molybdenum are discussed. As polycrystalline tungsten in aqueous environment has been investigated previously,[77, 78, 79, 80] the results were used to validate the method and to establish the ideal approach for the investigation of the molybdenum in the same conditions. According to computational investigations and the findings discussed later (4.4), molybdenum oxide clusters are expected to have similar characteristics and properties to those of tungsten oxide. Therefore, the conditions required to generate these clusters in an aqueous environment were investigated, starting from the experimental conditions of EC-STM (chapter 4). The behaviour of tungsten and molybdenum in alkaline environments are

addressed in the following chapter, when the electrochemical etching and the complete dissolution of the oxides are discussed (section 4.2.2).

2.3.1 Tungsten

The surface of metallic tungsten oxidises when exposed to the atmosphere, in aqueous environment the oxide is spontaneously hydrated. The oxide film can be distinguished in an inner layer, formed by more compact anhydrous WO_3 and an outer layer, in direct contact with the water molecules, consisting of hydrated oxides $[WO_3(H_2O)_x]$ loosely bound to the surface. Despite the exact dissolution mechanism occurring is not fully established, it is believed that the outer layer keeps dissolving in solution releasing oxide molecules following the (simplified) equilibrium[79, 81]

$$WO_{3\,(s)} + xH_2O \rightleftharpoons WO_3 \cdot xH_2O_{(s)} \rightleftharpoons H_2WO_4 \cdot yH_2O_{(aq)}$$

(2.50)
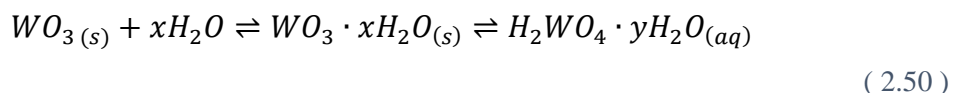
The cyclic voltammogram of the polycrystalline tungsten wire in 0.1M $HClO_4$, measured with a sweep rate of 50 mV/s, is shown in Figure 2.14. After two successive CV cycles, the system was left to rest at open circuit potential (OCP) for progressively longer equilibration times before measuring the next CV.

Figure 2.15 shows the OCP evolution of the pristine tungsten wire before any CV measurements (dashed trace) and after a CV is recorded (black trace). The markers highlight when the CVs were measured. The peaks of the first cycle of any CV increases proportionally over time until a plateau is reached after approximately 10 minutes of equilibration. Any successive CV cycle (not shown) is always equal to the shortest resting time (light green trace). Once the steady state is reached, longer resting times effects becomes negligible, as it follows from the OCP evolution.

The electrochemical investigation was carried out in the region where the tungsten oxide is expected to remain the thermodynamical favoured species, as it is highlighted (vertical green trace) in the Pourbaix diagram of the tungsten in an aqueous solution (calculated for a concentration of 10^{-4} M) in Figure 2.15. The metallic tungsten stability region lies outside the water stability region (delimited by dashed parallel traces). Therefore, the thermodynamic instability of the metallic tungsten under all experimental

conditions leads to spontaneous passivation or corrosion, depending on the acidity of the aqueous environment.[82]

In acidic environment, anodic oxidation promotes the formation of a thicker oxide layer on the surface of tungsten. Although the oxide layer should protect the metal and prevent further corrosion, the tungsten thermodynamical instability promotes the continuous dissolution of its oxides which are followed by generation of additional species in a cyclic process.[76, 77, 78, 81, 83]
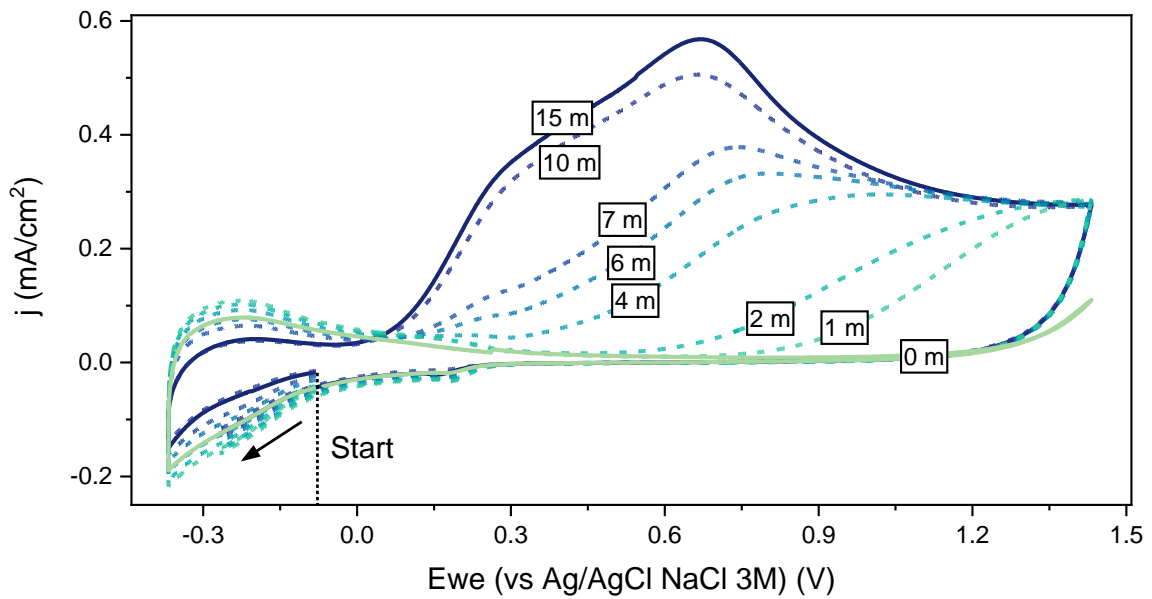
Figure 2.14. Cyclic voltammogram of polycrystalline tungsten wire in 0.1 M HClO$_4$ at 50 mV/s scan rate. The first two cycles (respectively, dark blue and light green solid traces) after equilibration for 15 minutes are followed by measurements at progressively shorter equilibration times at OCP (dashed traces). Hydrogen intercalation into the tungsten generates a small cathodic peak at 0.15 V.
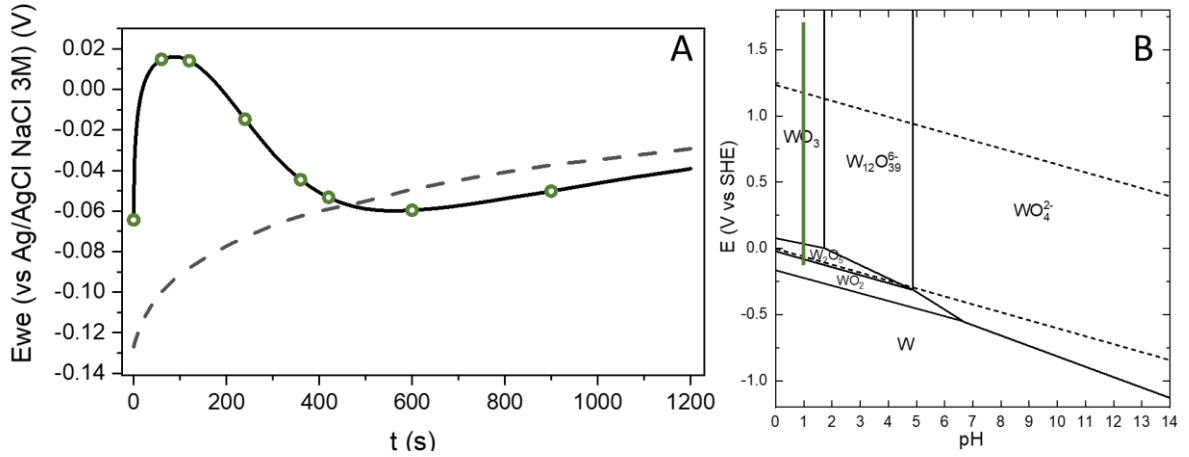
Figure 2.15. (A) Evolution of the open circuit potential before any measurements (dashed trace) and following the initial two CVs in (Figure 2.14). Markers represent the following CV measurements in (Figure 2.14, dashed). (B) Adapted Pourbaix diagram of W (calculated for an analytical tungsten concentration in solution of 10^{-4} M).[76] The thermodynamic stability region of water is indicated with the dashed parallel lines. The green vertical line shows the potential range of the CVs in Figure 2.14.

The generation of the oxide layer on the surface is responsible for the anodic current measured during the CV, from which the signal can be attributed to the contribution of three convoluted peaks resulting from successive tungsten oxidative states:[82]

$$0 \rightarrow +4, \quad W + 2H_2O \rightleftharpoons WO_2 + 4H^+ + 4e^-,$$
$$E^0 = -0.119 - 0.0591 \, pH \, (vs \, SHE)$$

$$(\,2.51\,)$$

$$+4 \rightarrow +5, \quad 2WO_2 + H_2O \rightleftharpoons W_2O_5 + 2H^+ + 2e^-,$$
$$E^0 = -0.031 - 0.0591 \, pH \, (vs \, SHE)$$

$$(\,2.52\,)$$

$$+5 \rightarrow +6, \quad W_2O_5 + H_2O \rightleftharpoons 2WO_3 + 2H^+ + 2e^-,$$
$$E^0 = -0.029 - 0.0591 \, pH \, (vs \, SHE)$$

$$(\,2.53\,)$$
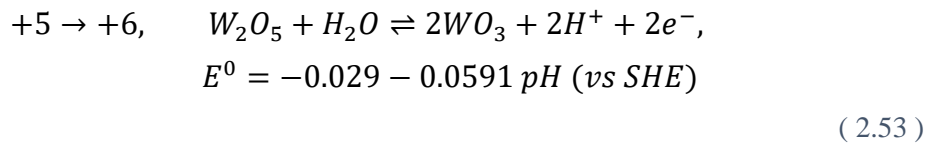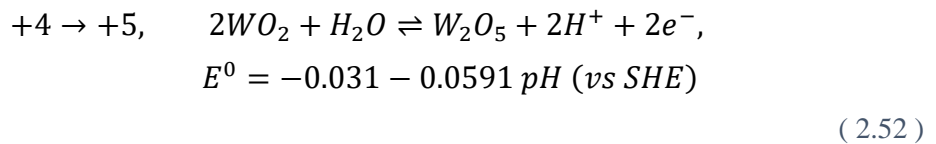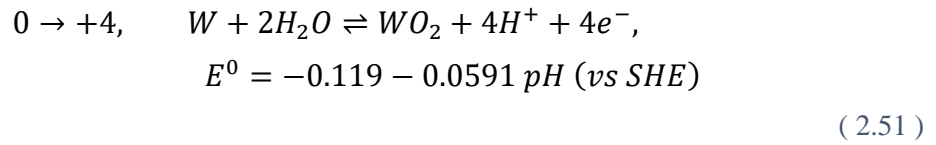
As the additional oxide layer formed during the first cycle prevents further oxidation of the surface, every following cycle is characterised by the absence of current. As mentioned, the layer dissolves within 10 minutes and for shorter equilibration times, partial dissolution leads to a CVs with smaller peak intensities. Further, the intensity of the hydrogen evolution signal is inversely proportional to the tungsten anodic peak, more

37

oxide surrounding the electrode reduces the conversion rate. Lastly, the small cathodic peak visible at 0.15 V is due to hydrogen intercalation into the tungsten oxide[78, 79, 80].

The thickness of the layer anodically formed on the metal and its dissolution rate were estimated. First, the charge associated with the process is determined by integration

$$Q = \frac{1}{v} \int I dv = \int I dt$$

(2.54)

Figure 2.16 shows the graphical integration of the current density as a function of time (from CV measurements). To distinguish between the charge associated with the anodic oxidation and any other contribution, we considered only the difference between the positive contribution of two successive cycles. The process was repeated for each voltammogram to estimate the evolution of the oxide thickness and its dissolution rate over time.
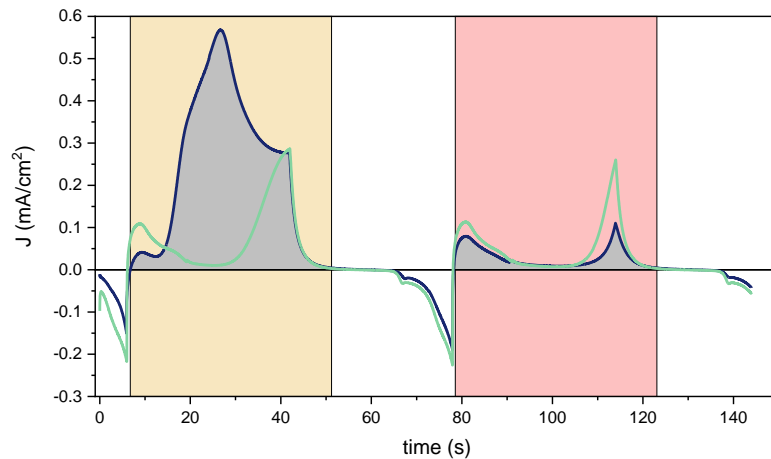
Figure 2.16. Current density vs. time obtained from the CV measurements of polycrystalline tungsten wire in 0.1 M HClO$_4$ at 50 mV/s scan rate (Figure 2.14). Two cycles measured after 15 minutes (blue) and 0 minutes (green) of equilibration times at OCP (Figure 2.15) (integration boundaries in yellow and pink).

By assuming the anodic oxidation generates a uniform film composition of WO$_3$ species, hence the process involves an exchange of 6 electrons (n_e) to oxidise the metallic W to W(VI), the amount in moles is

$$n = \frac{Q}{n_e F}$$

(2.55)

38

which allows to determine the thickness of the layer as

$$d = \frac{n\,MM}{\rho}$$

(2.56)

with molecular mass MM, and density $\rho = 7.2$ g/cm³.[84]

Table 1 summarises the evolution of the estimated tungsten oxide thickness over time and its dissolution rate. The confidence intervals reflect the reproducibility of the procedure. The results are in agreement with literature reports under similar conditions, where the dissolution is limited by diffusion.[85, 86]

Additional investigation was carried out by electrochemical impedance spectroscopy. Figure 2.17 shows the impedance recorded at anodic potential (1.4 V vs AgAgCl), where the tungsten is passivated (virtually no current). The data were fitted in accordance with the proposed bilayer oxide formation on the metallic tungsten.

t (min)	Q (mA·s/cm²)	d (nm)	dissolution rate (nm/min)
15	9.30	5.17 ± 0.05	0.345
10	8.55	4.76 ± 0.08	0.476
7	6.29	3.50 ± 0.12	0.499
6	5.51	3.07 ± 0.17	0.511
4	4.35	2.42 ± 0.18	0.605
2	2.06	1.15 ± 0.21	0.574
1	1.06	0.59 ± 0.14	0.588
			(avg 0.514 ± 0.047)

Table 1. Dissolution rate and thickness values of the tungsten oxide over time determined with cyclic voltammetry.

The fitting model is made with two RC combinations in series where the element R_s represents the uncompensated electrolyte resistance; R_1 and R_2 accounts for the Ohmic resistance of the inner and outer oxide layers; Q_1 and Q_2 describe the capacitance associated with the variation in the Faradaic charge on the surface under AC conditions. As measuring the individual data points takes increasingly long as the frequency becomes lower, the risk of spontaneous changes to the system and artefacts increases. This is the likely reason for the slow drift of the data points below 1 Hz, which were excluded from the fitting.
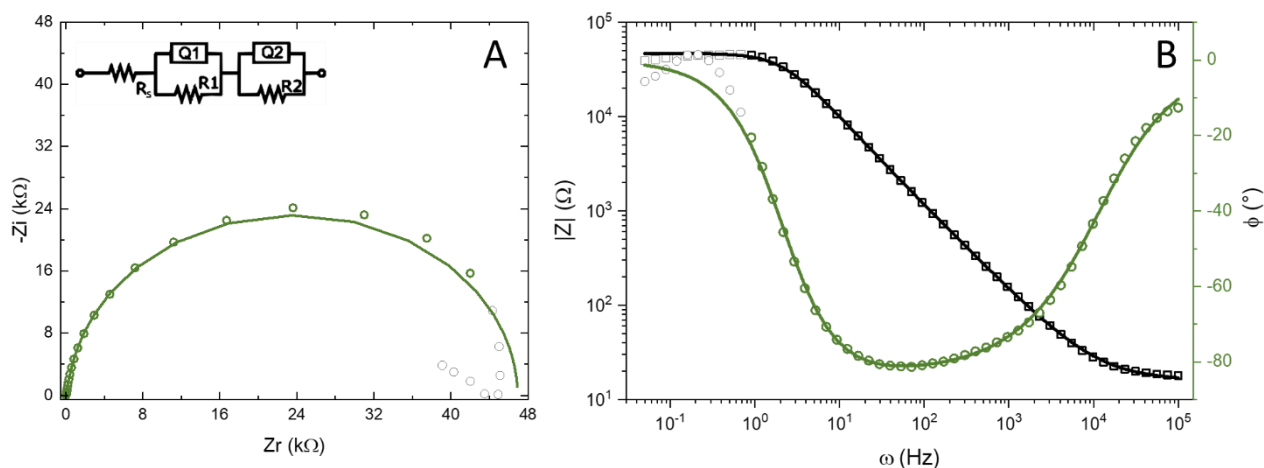
Figure 2.17. Nyquist (A) and Bode (B) plots of the EIS of metallic tungsten recorded at 1.4 V vs Ag/AgCl (after 5 minutes of equilibration) in HClO$_4$ 0.1 M. Inset shows the equivalent circuit used to fit (traces) the experimental data (markers). Low frequency experimental data (grey) excluded from the fitting.

Table 2 summarises the value resulting from the impedance fitting of the plot shown in Figure 2.17. The errors associated with the values are related to the confidence intervals of the algorithm used to fit the data.

	Value	Δerr %
R_s ($\Omega \cdot cm^2$)	3.13	10.4
R_1 ($\Omega \cdot cm^2$)	178.3	364.5
R_2 ($\Omega \cdot cm^2$)	9201.4	14.7
Q_1 ($\mu s^\alpha / \Omega\ cm^2$)	223.1	195.5
α_1	0.686	18.2
Q_2 ($\mu s^\alpha / \Omega\ cm^2$)	8.08	18.6
α_2	0.998	8.1
C_1 ($\mu F/cm^2$)	90.5	
C_2 ($\mu F/cm^2$)	8.0	
C_{tot} ($\mu F/cm^2$)	**7.36**	

Table 2. Parameters of the equivalent circuit used to fit the W impedance spectra in Figure 2.17.

As the equation of the CPE (2.49) does not directly provide capacitance values, the effective capacitances (C_1, C_2) are derived mathematically. As the alpha associated with the CPEs obtained from the fitting displayed a behaviour that tends to that of a pure capacitor ($\alpha = 1$). The CPE values were converted in effective capacitances following the formula proposed by Hsu and Mansfeld[87, 88]

$$C = Q(\omega_m'')^{\alpha-1}$$

(2.57)

with ω_m'' the frequency at which the imaginary part of the impedance $(-Z_i)$ has a maximum. The total capacitance for capacitor in series is calculated as

$$\frac{1}{C_{tot}} = \frac{1}{C_1} + \frac{1}{C_2}$$

(2.58)

The total effective capacitance (C_{tot}) was used to calculate the oxide layer of thickness d by approximation from a parallel plate capacitor, therefore

$$C = \varepsilon_0 \varepsilon_r \frac{A}{d}$$

(2.59)

with ε_0 the vacuum permittivity (8.85×10^{-12} F/m), A the surface of each plate in square meters, ε_r=43 the WO_3 relative permittivity in $HClO_4$.[89, 90] The final results (d = 5.56 nm) are in agreement with the estimated values obtained from cyclic voltammetry (d = 5.17 nm).

2.3.2 Molybdenum

Analogous investigations were carried out using metallic molybdenum to describe its behaviour in acidic aqueous environment. The molybdenum Pourbaix diagram shows a thermodynamic tendency to undergo corrosion, its passivation region is much more limited compared with that of tungsten. However, the similarity of tungsten and molybdenum clusters obtained from computational results and reports in literature support their generation in aqueous solution, despite a smaller stability range.[59, 91, 92]

Figure 2.18a compares the first two CV cycles of tungsten and molybdenum obtained after an equilibration time of 10 minutes. The stability window of the molybdenum is much more limited compared to tungsten, as an exponentially increase in anodic current is already observed at 0.3V above OCP. If the oxidative potential is held for few seconds, other than the darkening of the electrode, a pale dark blue plume diffuses in solution from the molybdenum electrode, suggesting the significant formation of soluble Mo(VI) species, a mixture of MoO_2, $MoO(OH)_2$, Mo_2O_5, and MoO_3 (2.62).[93, 94]

41

Contrary to the tungsten, the oxide layer on the molybdenum is not affected by the aqueous environment, and it does not change over time. Any additional CV cycle is practically identical to the first, even if the system is left resting to reach a steady state OCP for longer time.
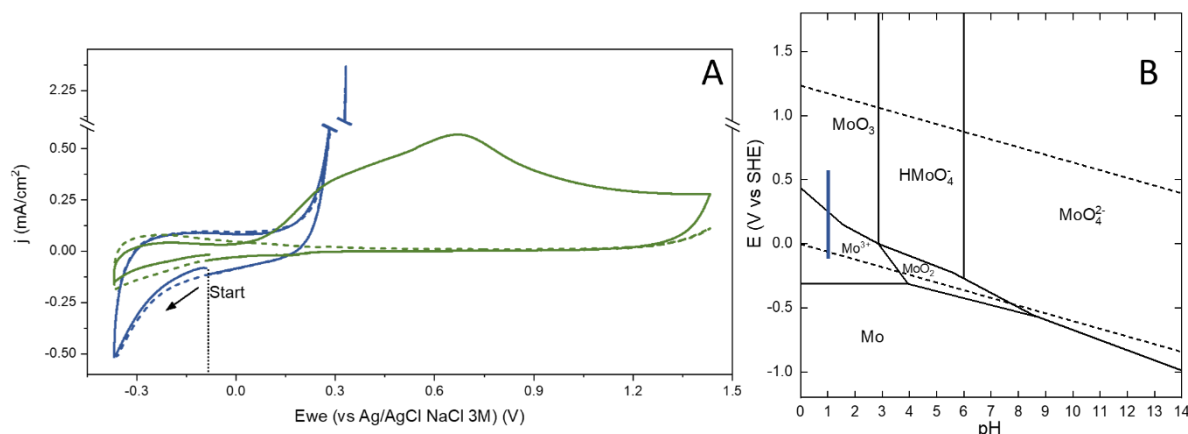
Figure 2.18. (A) CV of polycrystalline molybdenum wire in 0.1 M HClO$_4$, 50 mV/s scan rate. The first two cycles (solid and dashed blue traces) after equilibration for 10 minutes, compared with two cycles of W in the same condition (Figure 2.15, green traces). (B) Adapted Pourbaix diagram of Mo (calculated for an 10^{-4} M analytical molybdenum in solution).[76] The thermodynamic stability region of water is indicated with the dashed parallel lines. The blue vertical line shows the potential range of the CVs in (A).

The limited passivity region of molybdenum (Figure 2.13) required additional investigation in different pH condition (Appendix A). The CVs were carried in progressively less acidic solution up to neutrality, where the passivation is favoured in a limited interval. The behaviour did not significantly change over the interval studied, for which the oxidation was readily reached, and no change was recoded between cycles. However, the OCP evolution for the molybdenum showed significative difference when the anodisation was promoted. Figure 2.19 shows the difference of OCP for the processes occurring at pH 4 when the molybdenum is oxidised during the CV. If the oxidative peak is reached (referred to as 'irreversible' transformation due to the dark layer formed on the electrode, which requires physical removal (re-polishing) to restore its initial state), it is followed by a similar OCP trend observed with tungsten but much faster, suggesting a similar release of species into solution.

The overall electrochemical reaction involves the oxidation of metallic molybdenum to the hexavalent state:

$$Mo_{(s)} \rightarrow Mo(VI)_{aq} + 6e^-$$

(2.60)
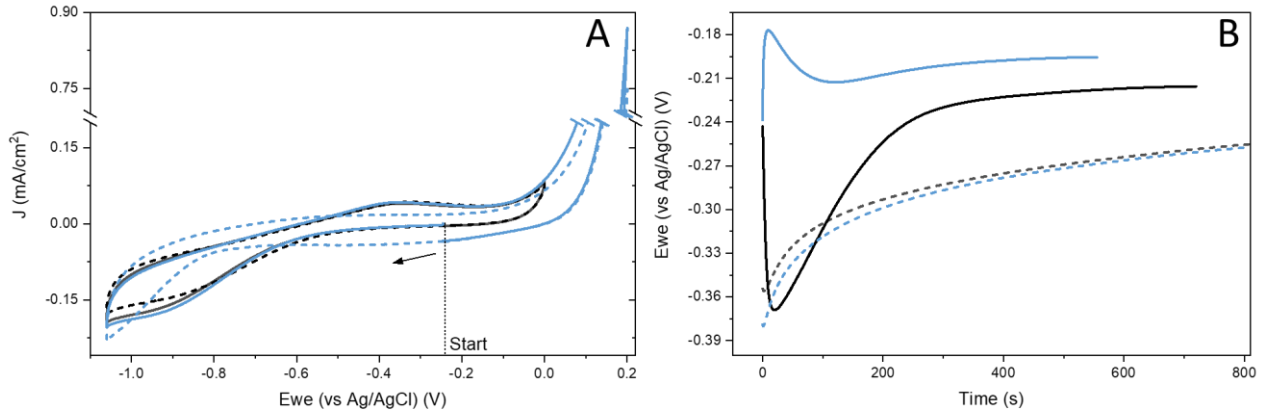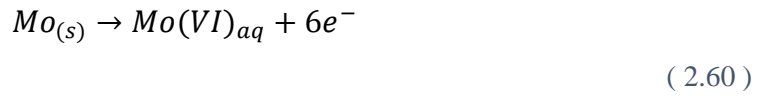
Figure 2.19. (A) Cyclic voltammogram of polycrystalline molybdenum wire in 0.1 M NaClO$_4$ (acidified to pH 4 with HClO$_4$), 50 mV/s scan rate. The first two cycles (black solid traces) after equilibration for 10 minutes, compared with two cycles of Mo where the oxidation in reached (red solid traces) after equilibration for 10 minutes. (B) Evolution of the open circuit potential before any measurements (dashed trace) and following the CVs in (A).

As for the tungsten, the stability region of metallic molybdenum lies outside the water stability region for every pH. In acidic environment the significant difference between the two metals is the "favoured" reaction, molybdenum spontaneously generate species responsible for corrosion processes rather than its passivation. In aqueous environment, the rapid formation of a relatively insoluble surface oxide that acts as a protective layer for the underlying metal from further corrosion is promoted.

$$2Mo_{(s)} + 5H_2O \rightarrow Mo_2O_{5\,(s)} + 10H^+ + 10e^-$$

(2.61)
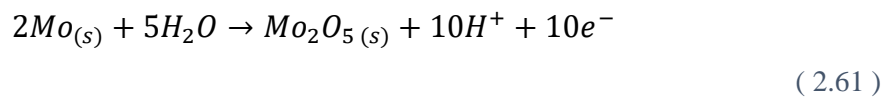
However, the high electrical conductivity of the oxide promotes formation of soluble species for small potential increments. The species generated from anodisation therefore are quickly lost from the metal despite the inert oxide on the surface. The main reaction steps resulting in the formation of the soluble species are summarised

$$Mo_2O_{5\,(s)} \rightarrow Mo_2O_{5\,(s)}^+ \rightarrow Mo_2O_5 \cdot xH_2O_{(s)} \rightarrow MoO_{3\,(s)} + H_2O \rightarrow H_2MoO_{4\,(aq)}$$

(2.62)
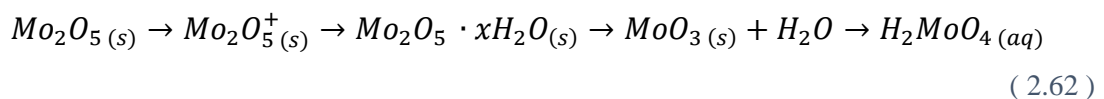
Hence, the presence of the oxide layer with conductive properties promoting the dissolution of the metal accounts for the quick exponential current growth and the similarity of successive CV cycles in Figure 2.18, Figure 2.19. The apparent resistance to corrosion and/or oxidation of molybdenum in the absence of applied potentials, given its inherent reactivity, suggests a lack of direct contact between the metal and the aqueous electrolyte.[93, 95, 96]

In contrast with the tungsten, the molybdenum undergoes transpassive oxidation as the metal oxide rapidly dissolves for small increment in the electrode potential. The current density function of time (from CV measurements) in Figure 2.20 shows the repetitive exponential anodic current generated at every cycle (only the first two cycles are shown). As most of the oxide dissolve in solution, the current does not contribute on additional oxide layer therefore no additional information was calculated.
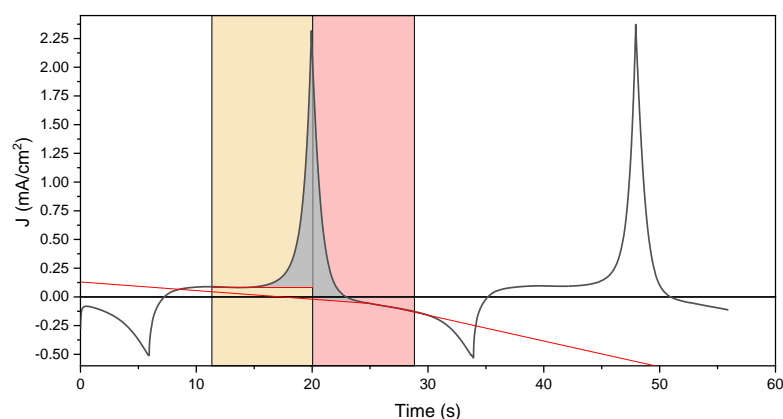
Figure 2.20. Current density vs. time obtained from the CV measurements of polycrystalline molybdenum wire in 0.1 M HClO$_4$ at 50 mV/s scan rate (integration boundaries in yellow and pink).

Figure 2.21 shows the impedance spectra of molybdenum in 0.1 M HClO$_4$ recorded at anodic potential (0.2 V vs Ag/AgCl) fitted using a simple Randles equivalent circuit. The element R_s in the circuit represents the uncompensated electrolyte resistance, R_p is the resistor associated with the charge transfer resistance at the interface and Q_d is related to the capacitance of the molybdenum/electrolyte interface.
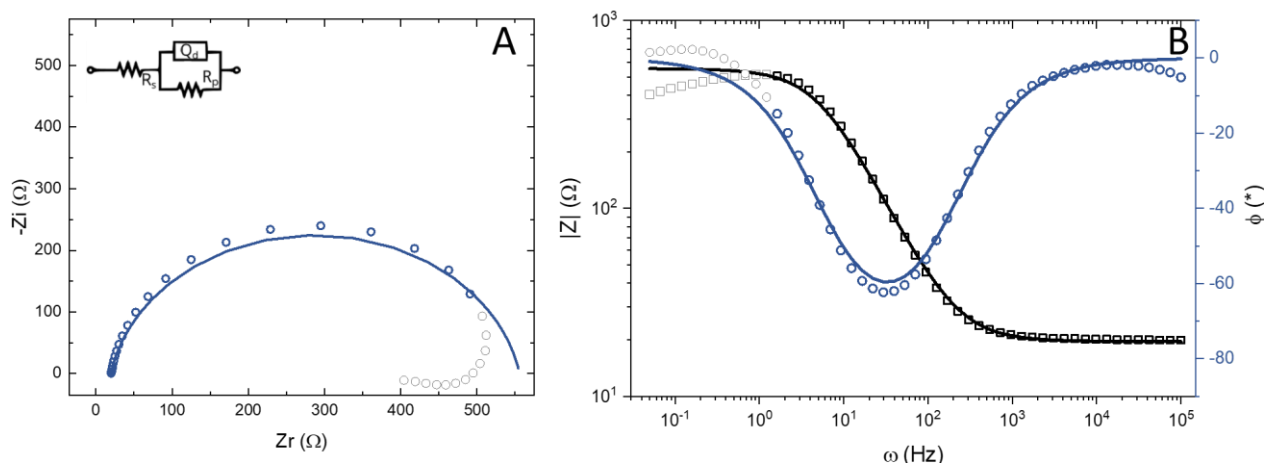
Figure 2.21. Nyquist (A) and Bode (B) plots of the EIS of metallic molybdenum recorded at 0.2 V vs Ag/AgCl (after 5 minutes of equilibration) in HClO₄ 0.1 M. Inset in (A) shows the equivalent circuit used to fit (traces) the experimental data (markers). Low frequency experimental data (grey) excluded from the fitting

The parameters resulting from the fitting are summarised in Table 3. The errors associated with the values are related to the confidence intervals of the algorithm used to fit the data. The value of capacitance obtained is an order of magnitude larger than the pure double-layer capacitance expected for a metal(oxide)/solution interface, however, it is in agreement with literature reports (200-600 $\mu F\ cm^{-2}$). This large capacitance is caused by hydrogen diffusion which is ultimately responsible for electroactive intermediates produced during the electrochemical oxidation of molybdenum and must therefore be seen as a pseudo-capacitance (reactions (2.61), (2.62)). The presence of hydrogen and other species is responsible for the production of an oxide-hydroxide film which is easily polarised at negative potential, increasing its conductivity as more protons and ions are incorporated in the oxide.[93]

	Value	Δerr %
R_s ($\Omega \cdot cm^2$)	3.91	5.3
R_p ($\Omega \cdot cm^2$)	107.2	7.1
Q_d ($\mu s^{\alpha}/\Omega\ cm^2$)	438.5	13.5
α_d	0.887	2.0
C_d ($\mu F/cm^2$)	366.0	

Table 3. Parameters of the equivalent circuit used to fit the Mo impedance spectra in Figure 2.21.

In summary, we have shown different electrochemical behaviours of tungsten and molybdenum in acidic environment. We aimed to find common conditions for the

45

passivation of the two metals as a function of pH and electrolyte composition. However, the molybdenum systematically showed transpassive behaviour, while tungsten easily passivated under all conditions. Impedance measurements in combination with mechanisms proposed in the literature, allowed to describe the oxide formation at the metal surface and estimate the rate of the oxide dissolution for tungsten. Ultimately, the electrochemical behaviour described for the two metals allowed to define the operational to be considered during EC-STM imaging.

3 Non-electrochemical characterisation of tungsten and molybdenum oxides

In this chapter we study the oxide clusters generated from the tungsten and molybdenum metals. We employ spectrometric measurements to quantify and speciate the oxides in solution. The cluster deposited on the boron nitride nanomesh are investigated with spectroscopic methods.

3.1 Theoretical background

In this section we introduce the fundamentals and the instrumentation of the non-electrochemical techniques employed in this work. A more comprehensive and detailed overview is provided in the references for ICP[97] and mass[98, 99] spectrometry, X-ray photoemission[100, 101, 102, 103] and Raman[104] spectroscopy.

3.1.1 Inductively coupled plasma - optical emission spectrometry

ICP-OES is an analytical tool that can detect a multitude of elements, typically in liquid form, that are dissolved in a range of matrices. However, it is also capable of analysing gases and solids. The analyte, fully dissolved in the liquid, is introduced in the ICP where it is heated up in a plasma flame. The elevate temperatures reached in the plasma (5000-8000 K) break down the analytes into individual charged species, excited atoms and ions. These charged species emit electromagnetic radiation, which corresponds to the discrete atomic emission lines characteristic of each element.

The emission lines are separated based on their wavelength by the diffractive optics and optical sensors within the OES to detect and quantify the species. The measurement is rapid, as all elements are excited in the plasma simultaneously, and they can be detected very rapidly one after another or simultaneously, depending on the instrument and procedure. The nature of the chemical bond in the analytes does not typically affect the analytical result, as it is destroyed completely in the plasma. ICP-OES has a broad working range that typically spans six orders of magnitude (from µg/L up to g/L). The ICP-OS can be divided in the sample introduction and analysing systems.
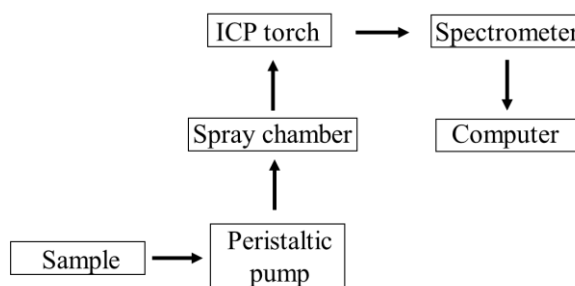
Figure 3.1. Schematic of the main components of an ICP-OES instrument.

The nebuliser converts the solution into an aerosol, to guarantee uniformity of the droplets and avoid to negatively affect the plasma. There are two main types of nebulisers: pneumatic and ultrasonic, each with various subtypes, chosen based on specific experimental requirements. In pneumatic nebulisers, a carrier gas flow creates a negative pressure zone to generate a fine aerosol mist. Ultrasonic nebulisers, on the other hand, rely on vibrating the sample on a small plate at ultrasonic frequencies for nebulisation.

To ensure the stability of the plasma and prevent larger droplets from entering, a spray chamber is connected to the nebuliser. The variation in the aerosol flow direction in the chamber allows to control and regulate the size of particles entering the plasma while directing residue to waste. The most common geometries are the Scott and cyclonic chambers. The flow of analytes and waste is controlled with a peristaltic pump to guarantee a constant rate, especially with samples of varying viscosities. The choice of tubing material and size depends on the properties of the analyte and matrix.

The ICP torch (Figure 3.2) consists of three concentric quartz tubes surrounded by a radio frequency (or induction) coil. Each tube serves a different purpose, with the inner tube transporting the aerosol, the intermediate channel maintaining gas flow, and the outer tube cooling the torch wall. The operating gas is typically argon but additional gases like nitrogen, oxygen, or hydrogen can be mixed with it for specific applications.

The induction coil surrounding the torch generates an electromagnetic field when supplied with alternating current. This field maintains the ionised gas which by chain reactions of collisions (leading to resistive heat) and further ionisation reaches a stable, high-temperature plasma state into which the aerosol is introduced for analysis. In the plasma the analytes undergo a series of processes: the solvent is stripped, leaving

microscopic solid particles (desolvation); the particles are vaporised into gas phase (vaporisation) and broken into atoms (atomisation). The atoms are then excited and/or ionised so the resulting emitted light is collected using a sensor for analysis.
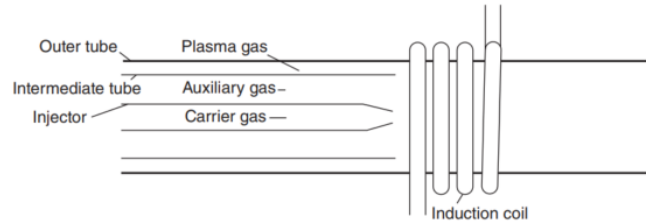
Figure 3.2. Schematic of the ICP torch.

The excited and/or ionised atoms in the plasma produce intense emission at several wavelengths. The emission line intensity I_e is proportional to the fraction of species populating the excited state N^*, related to the total amount of species N by the Boltzmann distribution

$$I_e = kN^*, N^* \propto e^{\frac{-E_1}{k_b T}}$$

(3.1)

with k efficiency of the transition, E_1 energy of the excited state relative to the ground state, k_b Boltzmann's constant, T temperature in Kelvin.

Depending on specific experimental requirements, the emitted plasma radiation can be collected from two different path lengths, either radial (lateral) or axial configuration, affecting sensitivities and detection limits. In the axial mode, the path is longer, hence detection limits are usually increased as the operating gas background is reduced. However, the optics can be easily damaged and matrix effects are more severe. The radial viewing mode is therefore preferred with more complex sample matrices and to achieve the best performance in terms of analytical figures of merit.

The optics are protected from the heat and any vapours generated from the plasma with a quartz window, transparent to the emitted radiation, which is collected and focused with a spectrometer. The radiation is separated spectrally by the optics, and the respective emission wavelengths are measured by one or more detectors; monochromatic sensor, which can observe a small range of wavelengths, or polychromatic sensor which allows to measure the wavelength in the spectrum at once. The polychromatic sensor can perform

multielement analysis of the sample and observe several emission lines for the same element at once, increasing the detection limit. The emission spectra of most elements are populated with numerous lines, their spectral interferences can result in erroneous measurements, to reduce the risk of errors it is therefore necessary to equip optics capable of optimal separation of neighbouring emission lines.

3.1.2 (High-resolution) mass spectrometry

Mass spectrometry is an analytical technique used for the identification and quantification chemical compounds based on their mass-to-charge ratio (m/z). High-resolution mass spectrometry (MS) can resolve ions with small differences in m/z. MS is often combined with other instruments like chromatographic columns (i.e. LC/MS, GC/MS) or ionising sources (i.e. ICP/MS) to enhance detection limits and analytical capabilities. A typical MS system comprises a vacuum system, ion source, mass analyser, and ion detector.
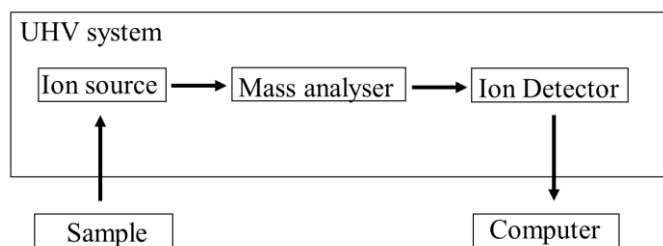
Figure 3.3. Schematic of the main components of a MS instrument.

Sample introduction methods vary depending on coupling requirements with other instruments. Modern systems can use atmospheric pressure ionisation interfaces to accommodate higher flow rates common in liquid chromatography (LC).

Different ionisation techniques are available depending on the sample introduction and the energy of ionisation (hard or soft techniques). The most employed under vacuum conditions are the electron and chemical ionisation, and electrospray or atmospheric pressure chemical ionisation under ambient conditions typical for LC-MS systems. Electron ionisation (EI) is a hard method. EI employs high-energy electrons to form positively charged samples in the gas phase. While it provides structural information, it generates small ions that are challenging to detect and interpret due to fragmentation.

Electrospray ionisation (ESI) is a soft ionisation technique at atmospheric pressure, it produces multiply charged ions suitable for analysing non-volatile molecules.

Fragmented ions are accelerated and separated by their mass-to-charge ratio (m/z) with various mass analysers, such as time-of-flight (TOF), quadrupole, ion trap, orbitrap, and tandem MS/MS. TOF analysers measure ions drift times to determine their m/z ratios, with smaller ions reaching the detector faster. Quadrupoles selectively transmit ions within a specific m/z range using controlled radiofrequency and direct current parameters.

The signal from the mass analyser is amplified with the detector. The most common MS detector is the electron multiplier, known for its reliability and signal amplification capability. It emits secondary electrons when impacted by energetic ionic analytes, enhancing the signal through a cascade of multiple electron collisions and emissions. The mass analyser and the detector influence the resolving power (defined as the full width at half maximum (FWHM) of a peak in the spectrum) of the MS system.

3.1.3 X-ray photoelectron spectroscopy

X-ray photoelectron spectroscopy (XPS), formerly known as electron spectroscopy for chemical analysis (ESCA), is a surface analysis non-destructive technique that excite the material core electrons with X-rays and measures the resulting energy and number of electrons emitted. XPS provides information about the elemental composition, their chemical and electronic states, chemical bonding, and electronic structure of the surface of a material. The spectra are recorded by irradiating the analytes with X-rays while measuring the kinetic energy and number of electrons escaping from the surface. The photoelectron is emitted following the collision of a photon with the atom. As the photons are annihilated during the process, the energy is fully transferred to the electron. If the energy is sufficient, the process can take place with solids.
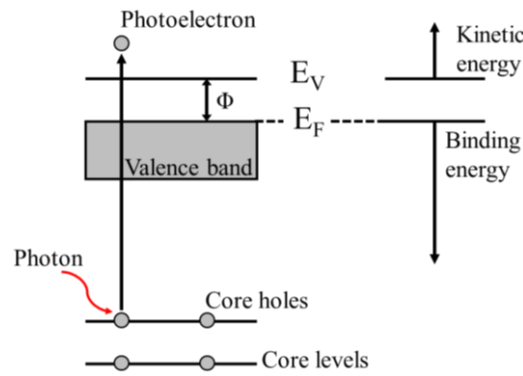
Figure 3.4. Simplified diagram of photoelectron emission following the absorption of a photon in the atom core levels.

The kinetic energy (KE) of the emitted electron is measurable, and it is function of the electron binding energy (BE), which is related to the nature of the species and their specific environment. The BE for each of the emitted electrons can be determined with the photoelectric effect equation

$$BE = E_{ph} - (KE + \phi)$$

(3.2)

with ϕ work function related to the specific material used for the spectrometer, E_{ph} X-Ray photon energy ($E_{ph} = h\nu$, h Plank's constant, ν X-ray frequency).
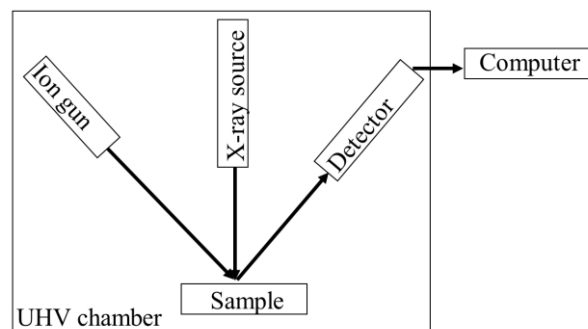
Figure 3.5. Schematic of the main components of a XPS instrument.

The XPS main components include a high vacuum chamber, an X-ray source, electron and ion sources, and an energy analyser schematised in Figure 3.5. The UHV chamber is crucial for accurate data acquisition as it prevents contamination and oxidation of the sample surface during analysis. High vacuum also increases the detection limit by allowing emitted photoelectrons to travel freely without interactions, resulting in more accurate signals.

The energy required to access core electron levels is within the X-ray region of the electromagnetic spectrum. The main X-rays sources for XPS instrument are classified as conventional, monochromatic, and synchrotron. Conventional sources use magnesium or aluminium anodes, their characteristic MgK_α or AlK_α radiation have energy suitable for core-level excitation. However, they produce minor lines at higher binding energies, affecting resolution and causing distortion. Monochromatic sources allow to mitigate the drawbacks of the conventional source by increasing the resolution and removing some of the background noise with a monochromator to select a narrow line from the radiation emitted from the source. The resulting photon flux is reduced but it can partially be compensated by an increase of the emission brightness with a fine-focused electron beam, which, however, reduce the area scanned of the sample. Synchrotron sources offer powerful and tuneable photon energy, enabling higher brightness and resolution in X-ray applications. They allow for variable kinetic energy, providing a detailed description of the sample surface.

Electron and ion sources within X-ray tubes are used for charge compensation, particularly when analysing insulating samples. Energy analysers filter photoelectrons based on their kinetic energy, passing only those with specific energy to the detector. The analyser needs high energy resolution for peak separation and high transmission for sensitivity. The energy resolution ΔE, in XPS measurements, results from the convolution of three parameters that exhibit a Gaussian line shape

$$\Delta E = \left[\left(\Delta E_p \right)^2 + \left(\Delta E_n \right)^2 + \left(\Delta E_a \right)^2 \right]^{1/2}$$

(3.3)

With ΔE_p full width at half maximum (FWHM) of the source, dependent on the photon source, ΔE_n line width of the photoelectron emission, dependant on the sample, ΔE_a energy resolution of the energy analyser.

Detectors measure the number of photoelectrons produced by the sample and require high sensitivity to detect individual electrons. The signal is amplified with electron multipliers which generate a current. The current response measured is represented in counts per second.

3.1.4 Raman spectroscopy

Infrared spectroscopy (IR) is an analytical technique that relies on the electromagnetic radiation absorption by the vibrational modes of molecules, allowing to characterize the chemical composition and the structural arrangement of the sample. A complementary technique is Raman spectroscopy (RS), which is based on the phenomenon of inelastic light scattering.

The energy of the photon E is inversely related to the radiation wavelength λ

$$E = \frac{hc}{\lambda}$$

$$(3.4)$$

with h Plank's constant, c light speed in vacuum. The photons of the light irradiating the matter can be absorbed, scattered or pass through without interacting.

When the photons are scattered, an elastic distortion (polarisation) of the electron cloud of the nuclei occurs. As the energy of the photon does not match the difference between two energy levels, it reaches an unstable virtual state and quickly released. Generally, the transition is too quick to induce any movement in the nuclei, it affects only the electron cloud and the energy of the photons adsorbed and scattered is equal, this process is known as Rayleigh (or elastic) scattering. In much more rare cases (once every 10^6-10^8 photons) the transition to a virtual state generates a variation in the energetic state of the species, resulting in the emission of photons with different energies, known as Raman (inelastic) scattering. Depending on the original state of the species before the excitation, two mechanisms occur. Stokes scattering involves photons with lower energy as the transition occurs from the ground electronic states and relaxes to a higher vibrational state of the same ground state. On the contrary, anti-Stokes scattering generates photons with higher energy as the electron is promoted from an exited vibrational level of the ground state and it relaxes to the lowest vibrational level of the ground state. Figure 3.6 shows the interaction of the radiation with the vibrational levels of a generic molecule resulting in an IR absorption and scattering processes.
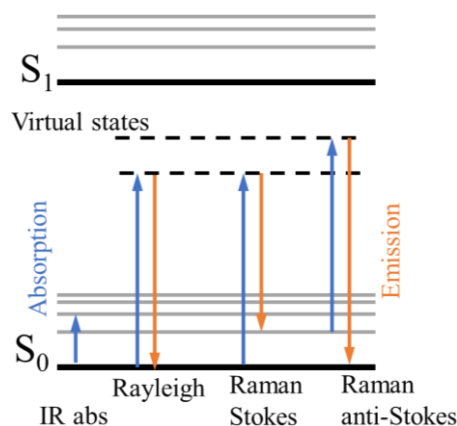
Figure 3.6. Diagram of the Rayleigh and Raman scattering processes following the absorption of a photon with the same energy and the infrared absorption. In the case of Raman scattering the emitted photons have respectively lower (Stokes) and higher (anti-Stokes) energies.

The relative intensity of the Stokes and anti-Stokes scattering depend on the population of the states of the species, related to Boltzmann distribution (equation (3.1)) and symmetry selection rules. Generally, at room temperature the species at an excited vibrational state is small, therefore Stokes scattering is preferred, however anti-Stokes scattering is used to avoid interferences (i.e. fluorescence).

When the frequency of the incident radiation closely matches the frequency of an electronic transition within the molecule, the intensity of Raman signal undergoes a substantial enhancement, and it is referred to as resonance Raman (RR). RR is a faster process compared to absorption, however, the relaxation to the ground state may involve emission which could overlap Raman signals. Additionally, surface-enhanced Raman scattering (SERS) is a process that can occur in specific conditions (i.e. molecules adsorbed on rough metal surface) and is capable of enhancing by order of magnitude the Raman signal, allowing detection up to single molecules.

Both Raman and infrared (IR) spectroscopy provide information about chemical composition from changes in the vibrational modes of molecules. However, these techniques rely on different molecular changes induced as a result of the interaction with the radiation: IR-active vibrations are generated from the variations in the molecular dipole moment, while Raman-active vibrations result from the alterations in the molecular polarizability. IR and Raman spectroscopy are therefore complementary as they are related to the symmetry of the molecules, expressed in terms of rule of mutual exclusion.

Molecules having a centre of symmetry can show either Raman-active or IR-active vibrations. This rule does not apply to molecules without a centre of symmetry allowing for modes that are both Raman and IR active.

As Raman scattering is an inherently weak phenomenon which relies on photon-phonon interactions, the laser source allows to increase the intensity of the signal. However, the spectroscopy can be limited by fluorescence. This phenomenon occurs when the absorbed energy is not completely dissipated through internal vibrations, and the excited molecules return to its ground state following different mechanisms which involves the emission of photons with lower energy during the process. Depending on the spin multiplicity of the ground and exited states the (stimulated or spontaneous) emission leads respectively to fluorescence or phosphorescence processes, the pathways are schematised in Figure 3.7.
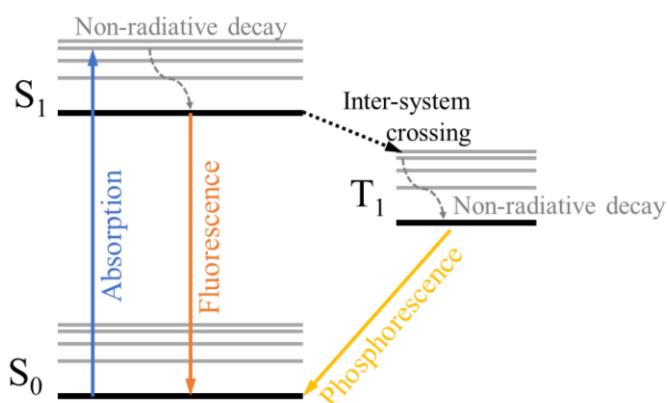
Figure 3.7. Simplified Jablonski diagram of fluorescence and phosphorescence processes following the absorption of photons. (Fluorescence occurs when the photons are generated from the radiative decay between states with the same spin multiplicity. In the case of phosphorescence, the adsorbed photon undergoes an additional non-radiative process occurs due to the partial overlap between singlet and triplet states (intersystem crossing) prior to radiative decay. Consequently, the emission has lower energy, but its lifetime is longer as the transition to the ground state is spin-forbidden due to the change in multiplicity. In both processes, part of the adsorbed energy is rapidly lost due to non-radiative internal rearrangements (vibrations) in the upper states).

Figure 3.8 shows the main components of a Raman spectrometer. The light source adopted is a monochromatic laser. In general, the use lasers in the visible region are limited by the tendency of numerous species to exhibit fluorescence. Such limitation can

be avoided by employing lasers operating in the near-infrared frequencies, a spectral region less susceptible to fluorescence interference. On the other hand, ultraviolet lasers are more costly and could have detrimental effects on the sample. The incident laser light is directed onto the sample, where it is scattered and filtered to block all non-frequency shifted radiation before it reaches the monochromator. Within the monochromator, a diffraction grating is used to spectrally disperse the radiation.
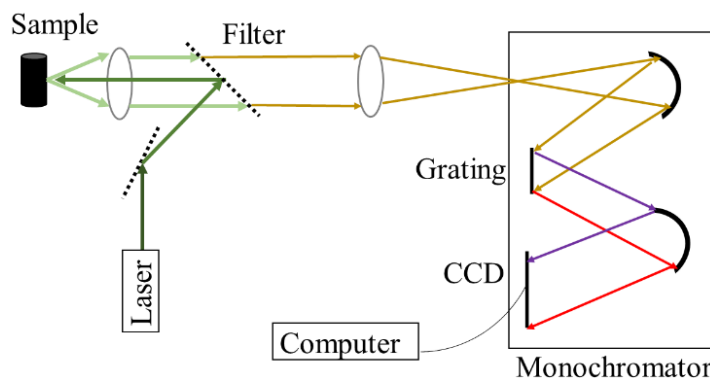
Figure 3.8. Outline of the main components of a dispersive Raman spectrometer.

The frequency components are subsequently detected and amplified with a charge-coupled device (CCD), a photomultiplier tube (PMT), or an avalanche photodiode (APD). Alternatively, an interferometer can be used in lieu of the monochromator. In this configuration, the scattered radiation, is divided and recombined using either a fixed or a moving mirror. The intensity of the resulting interference pattern is transformed with a Fourier transform (FT) to a conventional frequency-intensity spectrum. The spectrometer can be coupled to a microscope, combining its capability to control the sample location precisely with *in situ* Raman measurements. Raman spectroscopy can be integrated with other techniques and instrumentation (i.e. SEM, STM, LC).

3.2 Experimental details

The electrolyte solutions were prepared by dilution using Milli-Q® ultrapure water (resistivity 18.2 MOhm·cm, total organic carbon 2 ppb). Perchloric acid (70%, purity 99.99%, Thermo Fisher), sulfuric acid (Suprapur 96%, Supelco), formic acid (98%, Honeywell), sodium hydroxide solution (5 M, Sigma-Aldrich), ammonia solution 25% (Emsure ISO, Reag Ph Eur, Supelco) were used as received.

All electrochemical measurements were carried with a BioLogic BP-300 potentiostat with its proprietary software (EC-Lab v11.43). All the potentials are referred to silver/silver chloride (in NaCl 3 M).

Impedance data are fitted with EC-Lab (v11.43, BioLogic) and AfterMath (v1.6, PINE research) software.

3.2.1 Inductively coupled plasma - optical emission spectrometry

The tungsten and molybdenum oxides were prepared directly in 0.1 M hydrochloric acid solutions using tungsten (99.95%, annealed, diameter 0.25 mm, Agilent UK) and molybdenum (99.95%, annealed, diameter 0.25 mm, Agilent UK) wires. The metals were polished with sandpaper (grit P8000) and cleaned with Milli-Q® ultrapure water and filter paper (grade 1, Whatman). To simulate EC-STM conditions, in a two-electrode configuration cell with tungsten (or molybdenum) wire used both as reference and working electrode, the oxide were generated for roughly 4 hours by a repetition of cyclic voltammetry, and resting at open circuit potential were carried with a BioLogic BP-300 potentiostat. The sample as prepared was immediately analysed with the ICP-OES.

Additional solutions were prepared using tungsten(VI) oxide powder (99.995% trace metal basis, Sigma-Aldrich) and molybdenum oxide powder (99.995% trace metal basis, Sigma-Aldrich). The oxide was dissolved in a sodium hydroxide solution which was then neutralised and acidified with hydrochloric acid to a pH 1. The calibration solutions were prepared using tungsten standard for ICP (1002 ± 5 mg/l in HNO_3 5% and HF 2%, Sigma-Aldrich) and molybdenum standard for ICP (1000 ± 2 mg/l in HCl 10%, Sigma-Aldrich). Three different characteristic emission wavelength with different intensities (strong, medium and low) for each metal were used to verify the linearity of the response with different detection limits. The solutions for the calibration curves in the range of 2-80 ppm were prepared in HCl 0.1M. Each measurement was averaged three times per point and the two metals were used together, as the matrices does not interfere with either (website). Before every measurement, a blank sample was measured to confirm that no memory effect persists.

The ICP-OES analysis was conducted with an Agilent 5100 (Agilent Technologies) in axial mode after a wavelength calibration. The signal drift was corrected automatically with the ICP software. The RF coil power was 1.2 kW, the argon (plasma) flow was 12 L/min, the nebuliser flow was 0.7 L/min, the direct injection flow was 1.0 L/min. intensity of the emission lines was recorded for 1 second.

3.2.2 (High-resolution) mass spectrometry

The tungsten oxide samples were prepared with the same protocol as in (3.2.1), however different electrolytes were used to guarantee compatibility with the system (volatile electrolyte, and not capable of completing the metals. The tungsten oxide was generated using the wire in 0.1 M formic acid, for roughly 4 hours by a repetition of cyclic voltammetry and resting at open circuit potential. Additional samples from the tungsten oxide powder were obtained by dissolving it in NH4OH (20%, Emsure ISO, Reag Ph Eur, Supelco) followed by neutralisation with formic acid. Additional samples for comparison were prepared as in (3.2.1). The samples were analysed using a Shimadzu LCMS 8030 LCMS-IT-TOF mass spectrometer (the instrument combines QIT (ion trap) and TOF (time-of-flight)) by Dr David Rochester.

3.2.3 X-ray photoelectron spectroscopy

The tungsten and molybdenum oxides were generated on the hBN sample in 0.1M perchloric acid, simulating the setup of the EC-STM cell (as 4.3.2). The metal wires (tungsten or molybdenum), used as reference and working electrode in a two-electrode configuration, were positioned above the surface and connected to the BioLogic BP-300 potentiostat. the oxide was generated for approximately 2 hours by a repetition of cyclic voltammetry, chrono amperometry and resting at open circuit potential. The electrolyte solution was then removed, and the sample dried under nitrogen gas.

XPS measurements were performed with a Thermo Scientific K-Alpha X-ray photoelectron spectrometer at Institut de Science et d'Ingénierie Supramoléculaires (ISIS - CNRS/Unistra), Strasbourg, France, by Luca Cusin. The base chamber pressure was 10^{-9} mbar, the X-ray source was an aluminium anode (Al K_α radiation of 1486.6 eV) with a

beam spot size of 0.4 mm. Data processing was carried out with Termo Avantage (Thermo Fisher Scientific, v5.99).

3.2.4 Raman spectroscopy

Similar to samples for XPS (3.2.3), Raman samples were prepared by tungsten and molybdenum oxides deposition on gold and boron nitride surfaces by dissolution in different electrolytes (sulfuric acid, perchloric acid, formic acid). The surfaces were kept in the solution during the oxide generation and dried with N_2 before the measurements. In a separate series of experiments, tungsten(VI) oxide powder (99.995% trace metal basis, Sigma-Aldrich) and molybdenum oxide powder (99.995% trace metal basis, Sigma-Aldrich) were deposited directly on the sample after dissolution from alkaline environment followed by acidification as reported in 3.2.1 and 3.2.2.The electrolyte was removed, and the sample dried under nitrogen gas before the measurements.

The Raman measurements were carried at standard room temperature and pressure (298 K and 1 atm) with an inVia confocal Raman microscope (Renishaw plc) with 532 and 785 nm wavelength lasers (respectively, 15 mW and 20 mW when operating at 100%) and a 50x optic. Data processing was carried out with Spectragryph (v1.2), baseline correction was performed with adaptive method and smoothing with triangular moving average of 4 intervals.

Additional measurements were carried out by Dr. Josh Lea at Oxford Instruments WITec and NanoAnalysis, UK, using a WITec alpha300r (Oxford Instruments) confocal Raman microscope equipped with 532 nm and 785 nm lasers coupled to a WITec spectrometer, integrated with SEM microscopes (RISE).

3.3 Results and discussion

3.3.1 Inductively coupled plasma - optical emission spectrometry

ICP-OES was employed for the detection and quantification of the tungsten and molybdenum oxide generated in the electrolyte. The aqueous environment and the order of magnitude of the oxide concentration in the electrolyte are particularly suitable for the detection limits of the ICP. Additionally, the instrument allows for on-line measurements,

useful in case of further investigations.[105] For a comparison with the oxide generated in the electrochemical environment from the tungsten or molybdenum metals, the respective oxide powders were used. However, the tungsten oxide powder is insoluble in acidic environment and molybdenum oxide powder has a very limited solubility in the same conditions.[84] Therefore, both oxides were first dissolved in a strong alkaline environment overnight (4.7), and then acidified before the dilution to the required concentrations. To limit the loss of analyte, as the acidification was followed by immediate flocculation, the sample were prepared with small concentration and immediately analysed.

The analysis was conducted by recording the signal from three wavelengths with different intensity response (low, medium, and high) for each metal. Table 4 shows the final metal concentration in the sample analysed calculated from the initial calibration with the standard solutions. A blank was measured before any sample to ensure no uptake was occurring. The measures were averaged over three repetitions and the final values provided are reported only if they were within a confidence interval minor than 3%.

	W (nm)			Mo (nm)		
	203.59	207.91	209.47	202.03	203.85	284.82
	C (ppm)					
Blank*	-	-	-	-	-	-
WO$_3$ (5ppm)	2.32	2.42	2.4	-	-	-
WO$_3$ (50 ppm)	22.38	23.05	22.88	-	-	-
WO$_x$	3.79	3.96	3.89	-	-	-
MoO$_3$ (5 ppm)	-	-	-	2.39	2.36	2.32
MoO$_3$ (50 ppm)	0.31	-	-	23.22	22.75	22.36
MoO$_x$	0.12	-	-	10.73	10.44	10.33

Table 4. Concentration of W and Mo sample obtained by measuring 3 different wavelengths for each metal (values not reported when below the limit of detection). Results reported within a confidence interval minor than 3%.

The flocculation observed immediately after the acidification of the sample prepared by oxide powder dissolution affected their final concentrations, which proved to be lower than the expected values from theoretical calculations.

For the oxide samples generated electrochemically from the metal electrode, the final results lie in the interval estimated of 10 ppm (± 4 ppm). More significantly, the obtained results allowed to validate the protocol for the sample preparation by confirming the presence of both the oxide metals from the powder dissolution and the oxides generated in the electrochemical cell. A precise statistical analysis with a higher number of samples and by using internal standards would increase the reproducibility of the results. However, this was beyond the purpose of the current work, and it could be further developed especially in the case of on-line investigations.

Although ICP-OES analyses confirmed the presence of both metals in solution – regardless of their origin (i.e. electrochemical generation, dissolution from the oxide powder) – the technique does not provide information about their composition. Hence, the samples were further investigated with high-resolution mass spectroscopy.

3.3.2 (High-resolution) mass spectrometry

Following ICP-OES results, MS measurements were carried to speciate the oxide samples. Before any molybdenum samples, only tungsten oxides were analysed. The distinctive isotopic pattern and bigger molecular mass of tungsten allow for easier identification of its oxide and adducts. Figure 3.9 shows the comparison between the theoretical isotopic pattern of W and Mo.
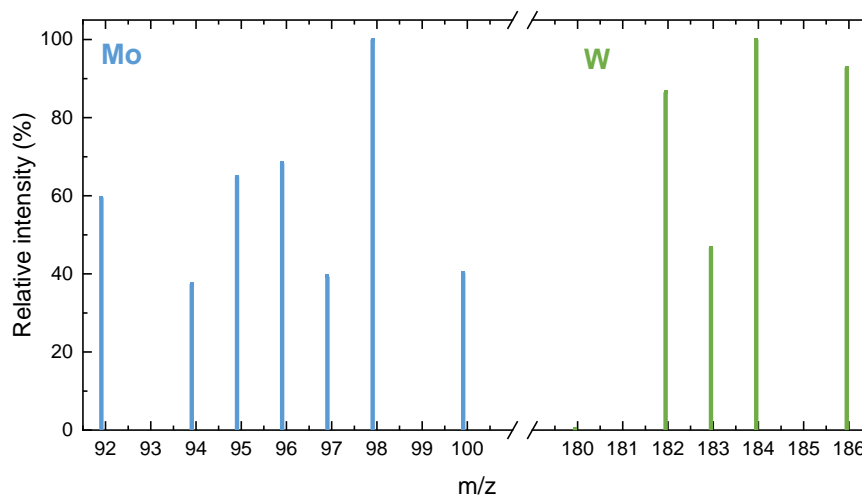
Figure 3.9. Theorical isotopic fragmentation patterns of Mo (blue trace) and W (green trace).

The results from the analysis of the tungsten oxide dissolved from the powder and the oxide generated electrochemically, both positive and negative adducts are reported in Appendix B. For all the measurements, no characteristic fragmentation was observed as the only spectrometric patters observed originated from contaminants in the solution and the instrument column. To investigate the lack of tungsten signal, samples of the oxide powder in alkaline solution (prepared following the same protocol as the other sample but without acidification step) were analysed. The alkaline environment guarantees the presence of the tungstate (reaction (4.7)) and increases the probability of its identification. However, no characteristic fragmentations were recorded, but only signals from contaminants and the electrolyte.

As other reports in literature showed the characterisation of tungsten oxides with mass spectrometry,[106, 107] we conclude that the ionisation adopted (i.e. electrospray ionisation) was not suitable to generate ionic species efficiently, which resulted in the loss of any oxides before the detection.[108, 109]

3.3.3 X-ray photoelectron spectroscopy

The hBN nanomesh samples, exposed to conditions which simulated an EC-STM experiment, were analysed with XPS. The solution was removed, the surface dried with nitrogen and placed on the UHV sample holder for the analysis without any further treatment.

Figure 3.10 shows the survey spectra of the nanomesh samples exposed to tungsten, molybdenum or only the electrolyte. Despite the low resolution and low intensity of the peaks within the initial 300 eV, the differences between the two metals are sufficient to distinguish between the contribution of the associated peaks (respectively, W4f, W4d (and W4p, at higher energy) and Mo3d).
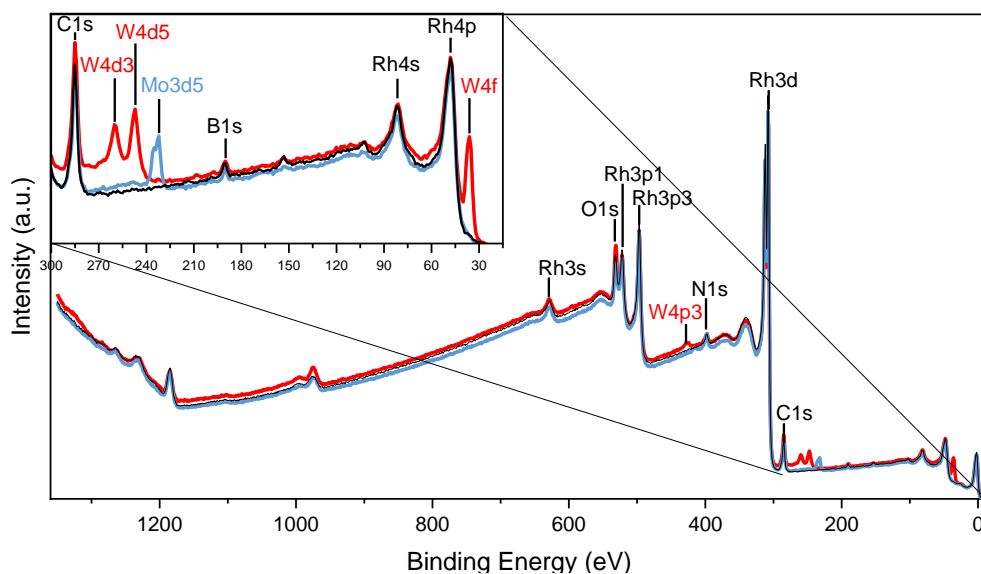
Figure 3.10. Survey XPS of tungsten (red trace) and molybdenum (blue trace) deposited on the nanomesh sample following electrochemical generation, and bare nanomesh (black trace). The inset shows a magnification for the low binding energies.

Additionally, signals related to the BN monolayer (B1s and N1s) can be observed, however it is affected by physisorbed contaminants (i.e. atmospheric nitrogen).[30, 110] The organic contamination, due to sample exposure to the atmosphere, provides an indication of the signal deviation from the reference, the experimental value (284.92 ± 0.57 eV, averaged with all the survey spectra) does not deviate significantly from the literature value (284.8 eV).[111, 112]

High-resolution spectra allow to describe the specific signals with greater details, Figure 3.11a shows the spectra related to tungsten (W4f) for the three samples, which confirm its presence only in one sample. It is possible to describe further the species (i.e. oxidation state) and determine if there are more than one type present. The binding energies obtained from curve fitting are summarised in Table 5, the two well-separated peaks are the result of spin-orbit coupling, and the energy difference coincides with the literature for WO_3 species.[102, 113]
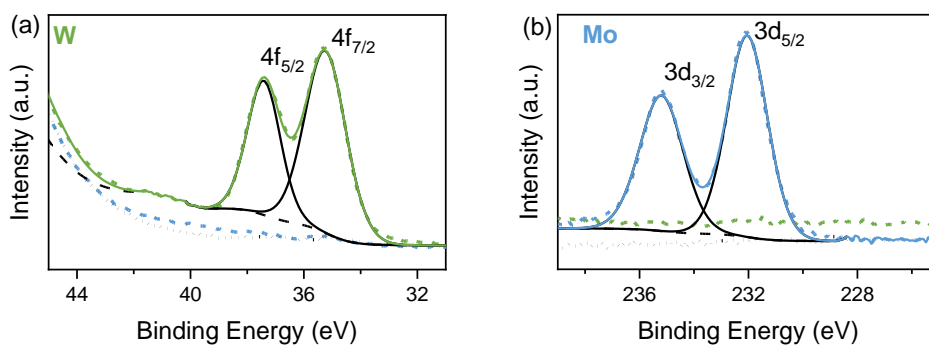
Figure 3.11. High resolution spectra of tungsten (a) and molybdenum (b) of the sample analysed (nanomesh exposed to tungsten (green traces), molybdenum (blue traces), and only the electrolyte (black traces)).

	Peak BE (eV)	FWHM (eV)	Atomic %	Δ BE (eV)
W4f A	37.41	1.39	17.93	
W4f B	35.24	1.71	29.95	2.17
Mo3d A	235.2	1.89	15.28	
Mo3d B	232.04	1.75	21.05	3.16

Table 5. Values resulting from the fitting of the high-resolution spectra for tungsten and molybdenum.

It is possible to assume that the contribution to the tungsten signal comes only from WO_3 as its shape and binding energy allows to exclude any other oxidation states, which would have lower binding energies values, by at least 2 eV and 3 eV, other than generally less symmetric curves. Small deviation from the value of the BE for WO_3 is attribute to the different origins.[64] The XPS experimental results for tungsten oxide are commonly referred to species generated in UHV where the property and thickness are responsible for deviation in the BE: increased thickness correlates with a progressive decrease in binding energy by approximately 2 eV, however the shape of the curves or the energy difference from the spin-orbit coupling remain constant.[59, 114]

The high-resolution spectra for molybdenum (Mo3d) in Figure 3.11b is qualitatively identical to the tungsten as the similar electronic configuration generates a doublet from the spin-orbit coupling. However, the much smaller distance between the nucleus and orbitals results in higher binding energies, with an energy difference of 3.16 eV. The spectra confirm the presence of MoO_3 species only as binding energies for other oxides or metallic molybdenum are approximately 5 eV lower and exhibit asymmetrical peaks.[115, 116, 117]

3.3.4 Raman spectroscopy

Before measuring the Raman signal of the metal oxides layer on the sample, the instrumental parameters were optimised. Additionally, the suitable electrolyte and concentration were investigated using gold on glass (GoG) and single crystal gold samples as they provide a reusable and surface easy to clean by simple rinsing and flame annealing (or electropolishing in some cases).

Figure 3.12a,b shows the spectra obtained by measuring small amounts of WO_3 and MoO_3 powders directly deposited on the hBN nanomesh. The measurements provided references values for the system studied, a comparison between the two metal (even when they are co-deposited on the same surface) and literature values. Two laser sources (785 nm and 523 nm) were used; however the resulting spectra were practically identical except for the background noise. With the 532 nm laser, the background of the gold and hBN samples, showed a broad fluorescence signal, while the 785 nm laser showed a more localized fluorescence signal between 1000 and 2000 cm^{-1}. Generally, for the excitation source used, the signal of any species detected was enough to overcome the fluorescence signal. Hence, only one source is presented and discussed in the chapter, unless specified differently.

The spectrum of the WO_3 powder in Figure 3.12b shows major vibrational modes at 808, 718, and 275 cm^{-1} assigned respectively to the stretching of O-W-O and O-W bonds, and the bending of O-W-O bonds. The values are with an error margin of ± 1 cm^{-1} are comparable to the characteristic frequencies of m-WO_3, excluding as expected the presence of more hydrated forms ($WO_3 \cdot xH_2O$) as in such case the value of the characteristic Raman signal differ by at least 10 cm^{-1} and additional signals related to the vibrational modes and bending generated by water bonds are observed.[114, 118, 119]

The MoO_3 spectrum in Figure 3.12a shows major vibrational modes at 996 (s), 819 (vs), and 667 (m) cm^{-1} for O-Mo-O stretching, 338 (m), 284 (m), 246 (w), 218 (w), and 199 (w) cm^{-1} for bending modes having different symmetries, and at 159 (m), 131 (m), and 117 (m) cm^{-1} for other deformation modes. Analogously to the tungsten the values are within a small error (± 1 cm^{-1}), comparable to literature data of characteristic frequencies of o-MoO_3. Additionally, the hydrated forms ($MoO_3 \cdot xH_2O$) differ

significantly from the experimental values, showing deviations of more than 15 cm^{-1} and additional signals related to the interaction with water molecules.[92, 120]
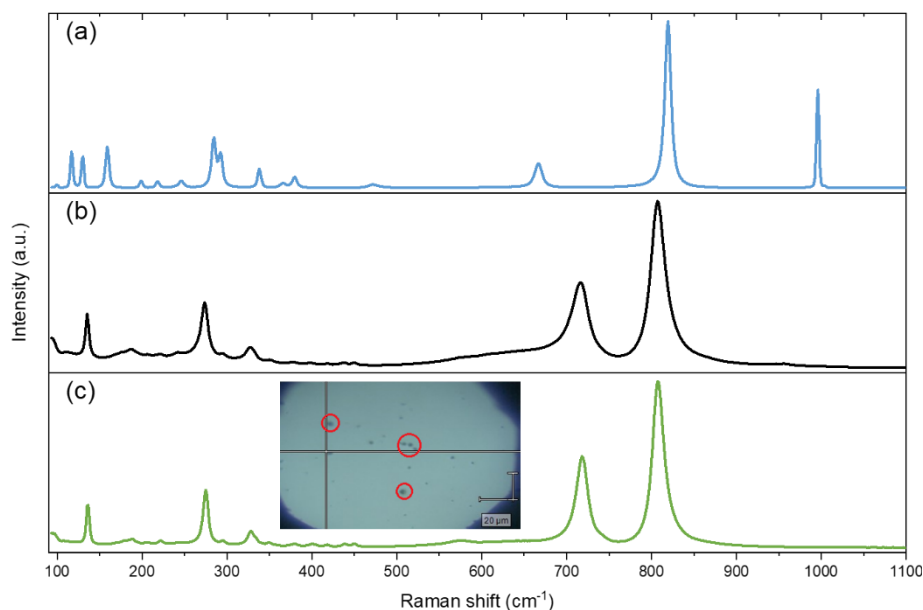
Figure 3.12. Raman spectra of MoO$_3$ (a) and WO$_3$ (b) powders (standards). (c) Spectra of the visible impurities (red circles in the inset) on the sample.

As a next step, the tungsten oxide powder was dissolved (following the same method as in 3.2.1 and 3.2.2) in two different solution: sodium hydroxide neutralised with sulfuric acid, and ammonia solution neutralised to a mild acidic buffer with formic acid. Different concentrations (5 to 5000 ppm) were deposited on the gold surface (used for testing before the nanomesh) by evaporating the with nitrogen gas before the Raman measurements. Only signals from the electrolytes used or impurities deposited on the samples were detected (Appendix C). However, sample obtained with the most concentrated solution generated a crust visible with the optical microscopy, which for long laser exposure (i.e. surface mapping with a small grid) produced oxides signals. The intensity of the beam is responsible for a localised increase in the temperature which degraded the top layer of the crust, exposing the oxide inside which become measurable. In these cases, the samples concentrations were three orders of magnitude higher than the estimated concentration achieved during the electrochemical oxide generation, hence we did not investigate further (Appendix C).

Eventually, nanomesh samples were measured after the deposition of electrochemically generated tungsten oxides. As for the diluted samples, no boron nitride[121, 122] nor metal

oxide signals were observed. However, only by focusing the beam on the visible impurities on the sample surface, the Raman signal identical to the measured oxide powder was measured (Figure 3.12c and inset). Their particular nature combined with the lack of signal from hydrated forms suggests that they could be impurities released from the metallic wire (i.e. residues of the polishing process) which tends to deposit during the electrochemical generation, excluding the detection of the monolayer formed on the surface.

Additional tests were carried by using gold samples to investigate the effect of the surface in combination with further analysis with Raman microscopy coupled with SEM (RISE) by Dr Josh Lea. The samples were mapped in different areas and studied with a principal component analysis (PCA) to seek for any possible information from the surface. However, the analysis did not provide useful information as only signals originated from contaminants on the sample were detected. The background noise generated from sample fluorescence prevented the better detection limit of the instrument (Appendix C).

In summary, in this chapter we have used non-electrochemical techniques to provide complementary information about the system studied with EC-STM. Both tungsten and molybdenum were investigated with spectrometric techniques and ICP-OES confirmed the presence of the metals in solution generated both electrochemically and following dissolution from oxide powders. Mass spectrometry did not provide information about the oxides in solution likely because the ionisation conditions were not suitable. With Raman spectroscopy we could not detect the presence of the oxides on the nanomesh surface due to the strong fluorescence of the sample and the low density of the deposited clusters. However, XPS confirmed the presence of the tungsten and molybdenum oxide clusters deposited on the nanomesh.

4 Scanning tunnelling microscopy of W and Mo oxide clusters on hBN nanomesh

In this chapter we optimise the scanning tunnelling microscope to reduce external interferences and increase the resolution of the final images. We employ for the first-time molybdenum as a probe for imaging in electrochemical conditions. We study the tungsten and molybdenum oxide clusters deposited on the boron nitride nanomesh.

4.1 Theoretical background

In this section the instrumental aspects and the principles of quantum physics on which (EC-)STM is based are introduced following the outline of Voigtländer[123], where a more comprehensive and detailed overview is provided.

4.1.1 Scanning tunnelling microscopy

Scanning tunnelling microscopy (STM) is an imaging technique used to study surfaces at the atomic scale. It was invented in 1981 by Gerd Binnig and Heinrich Rohrer, who were later awarded the Nobel Prize in Physics for their contributions to its development.[124] STM images are generated by scanning a sharp tip, typically made of tungsten or platinum, over the surface of a sample. A small voltage is applied between the tip and the surface, which are very close (within a few Ångström), creating a tunnelling current between the tip and the surface that is highly sensitive to the distance between them.

Figure 4.1 shows the main component of an STM. The piezo element in the scanner finely controls the tip used for imaging. The sample position is adjusted with micro-screws and controlled with motors which are used to regulate the distance between the scanner and the sample. The environmental chamber is suspended inside an insulation chamber to protect from any vibrations from the surroundings, acoustic, and electrical noise. The system is composed by a scanner, controlled via the Head Electronic Box and a bipotentiostat interfaced to the computer. STM is not limited to work in UHV, it is

possible to work with the necessary adaptation, under ambient condition, the presence of a liquid, or electrolyte.
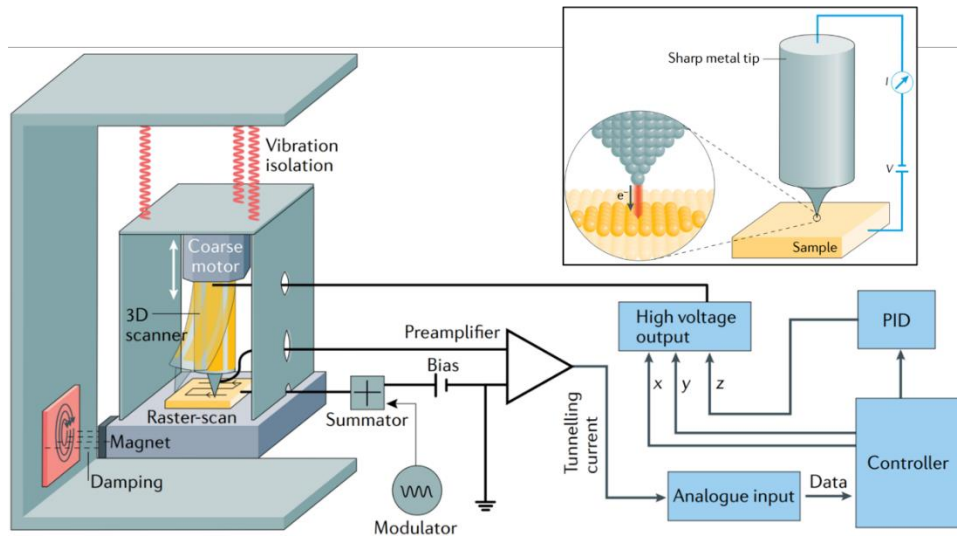
Figure 4.1. Main components of a scanning tunnelling microscope. Adapted.[125]

Figure 4.2 shows the approximation of an electron tunnelling through the junction solid-vacuum-solid as a one-dimensional model where a square potential barrier $V(z)$ of height V_0 above the bottom of the potential ($V = 0$) for $0 < z < d$ and E the energy of the electron tunnelling through the barrier.
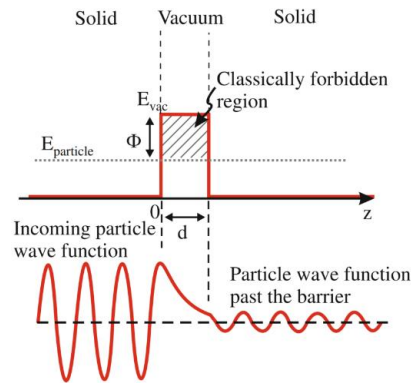
Figure 4.2. Diagrams of a wave function penetrating the vacuum barrier for one-dimensional metal-vacuum-metal tunnelling junction. (top) Shows one-dimensional potential diagram for solid-vacuum-solid configuration with a barrier of height E_{vac}, energy of an electron $E_{particle}$ and the distance d between the solids. (bottom) Shows the electron wave function oscillating to the barrier, which decay exponentially inside it and oscillate again after passing it. Note: the wave function is a complex function and only the cosine function, corresponding to the real part, is represented; the probability for the incoming wave $|\psi(z)|^2 = 1$ is independent of z. Adapted.[123]

In the case of STM, the Figure 4.2 describes the junction tip-gap-sample, with the electrons in the solid at the highest energy available, the Fermi level $E = E_{particle} = E_F$ and the potential barrier equal to the energy of the free electron, or vacuum energy $E_{vacuum} = V_0$. As a result, is defined the work function Φ as the minimum energy needed to remove the particle from the solid, in first approximation it represents the bonding energy of the electrons inside the solid

$$\Phi = E_{vacuum} - E_F$$

(4.1)

The solution for the one-dimensional time-independent Schrödinger equation

$$\frac{\hbar^2}{2m}\frac{\partial^2}{\partial z^2}\psi(z) = [V(z) - E]\psi(z)$$

(4.2)

is an oscillating function inside the solids ([see image] region I and III) as the vacuum barrier $V_0 = E_{vacuum}$ is zero, therefore there is a finite probability for the electron to be in both metal.

Furthermore, the electron has a probability to penetrate inside the barrier (region II Figure 4.2) and equation (4.2) is solved for an exponentially decaying wave function

$$\psi(z) = \psi(z); \; \kappa = \sqrt{\frac{2m\Phi}{\hbar^2}}$$

(4.3)

where the probability of the electron being at position z is proportional to $|\psi(z)|^2$, therefore (4.3) become

$$|\psi(z)|^2 = |\psi(0)|^2 e^{-2\kappa z}$$

(4.4)

Thus, given a transmission coefficient T, defined as

$$T = \frac{|\psi(z)|^2}{|\psi(0)|^2} \approx e^{-2\kappa z}$$

(4.5)

which decays exponentially with the distance z and the square root of the work function Φ.

Tunnelling currents can only be measured when a net excess of electrons flow from one metal to another. It can be achieved when a bias voltage is applied between the two metals, causing a shift of the Fermi levels of the tip and the sample. Figure 4.3 shows the energy diagram where the bias voltage ($eU_b = \Delta E_f = E_{F,S} - E_{F,T}$) results in tunnelling current from the tip to the empty states of the sample. When the fermi levels of both metals are aligned, no current can be measured as the tunnelling of one electron is simultaneously balanced by the movement of one electron in the opposite direction.
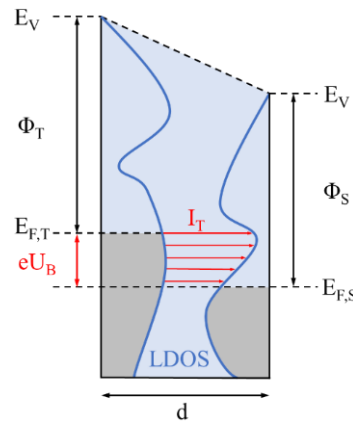
Figure 4.3. Energy diagram of the tunnel junction between tip (T) and sample (S) in the STM where the applied bias voltage between sample and tip (eUB) generates the tunnelling current (IT). With EF Fermi level, Φ work function, d distance tip-sample (tunnelling gap), and EV vacuum level. Adapted.[126]

The tunnelling current in influenced linearly by the bias voltage (U_B) and it is proportional to the transmission coefficient, which has an exponential relation with the height (Φ) and width (d) barriers, and the local density of states (LDOS) near the Fermi level of the sample. As predicted from Tersoff-Hamann theory the tunnelling current can be expressed as a function of the density of states of the tip ($\rho_T(E_F)$) and of the Fermi-level density of states of the sample ($\rho_S(r_0, E_F)$)[127, 128, 129]

$$I \approx V \cdot \rho_T(E_F) \cdot \rho_S(r_0, E_F)$$

(4.6)

The exponential dependency of the tunnelling current with the tip-sample distance allows very precise measure (and control) by piezoelectric actuator elements. The mechanical extension of the actuator elements is proportional to the voltage applied, allowing tip movement in x, y and z directions with atomic-scale precision. The tunnelling

current is measured as the tip is moved across the surface and controlled with a feedback loop that constantly adjusts the tip-sample distance to keep it constant (constant current mode, Figure 4.4A). As a result, the STM produces three-dimensional maps of the surface (apparent) topography. The interpretation of the topography information is influenced by the electronic properties of the surface, such as the local density of states and the local conductivity. Species with same dimension but different electronic properties (i.e. different conductivity) generates topography surface with (apparent) different tip-sample distance. In the case of STM in constant height mode (Figure 4.4B), the tip-sample distance is maintained at a fixed value as it scans over the sample surface while the tunnelling current is measured.
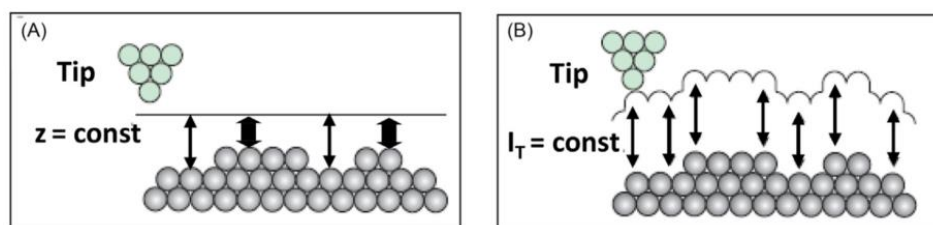
Figure 4.4. Schematics of the constant height (A) and current (B) modes of tunnelling microscopy. The strength of the current is represented with the arrows thickness. Adapted.[126]

4.1.2 *Electrochemical scanning tunnelling microscopy*

Electrochemical scanning tunnelling microscopy (EC-STM), formerly known as *in situ* STM, is a technique used to study the surface properties of electrochemical systems at the nanoscale level. It combines the principles of STM and electrochemistry allowing real-time imaging of electrochemical processes taking place at the electrode surface, such as formation of an electrochemical double layer, metal corrosion, and electrodeposition. EC-STM is developed with four electrodes including the tip, working, counter, and reference electrodes, which are controlled by a bipotentiostat (Figure 4.5). The bipotentiostat allows for the independent control of tip and the surface potential, allowing to influence the energy of their fermi level in addition to the resulting bias voltage (Figure 4.3).
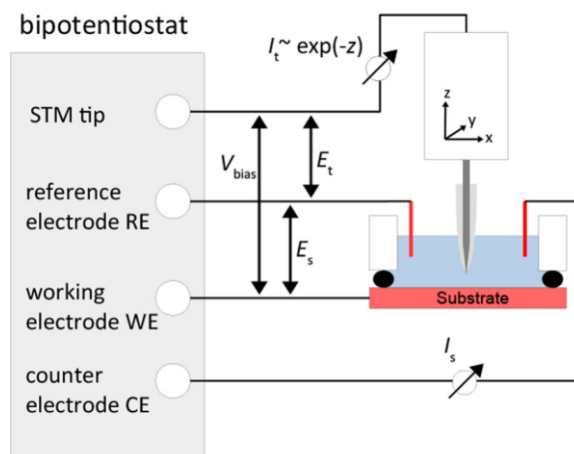
Figure 4.5. Outline of the main components of an electrochemical STM with the independent potential control over the solid-liquid interface allowed by the bi-potentiostat. Adapted.[19]

Experimentally it has been demonstrated that the tunnelling in electrolyte is different from the vacuum as the electrolyte affects both the height (Φ) and width (d) barriers. The adsorption of the water molecules on the surface contributes to lower the work function of the surfaces. Additionally, the water molecules affect the simple exponential decay with the distance as the layered structure of oscillating bonds between atoms diverge from the constant parallel surface of the UHV.

As the bias voltage between tip and surface may also cause Faradaic processes in the presence of the electrolyte, resulting in distortion of the tunnelling current, it is necessary to minimise such disturbance by insulating the tip to reduce the exposed surface (4.2.3).

4.2 Practical considerations

4.2.1 STM tip preparation (mechanical cutting)

The shape and type of the scanning probe in STM heavily affects the final quality and resolution of the images. It is important that the tips remain stable under high electric field and unreactive in the solution used for EC-STM. there are a multitude of techniques for the tip preparation, however the imaging is strongly affected by the shape of the actual apex, which is achieved spontaneously and unpredictably during the measurements (i.e. local variation in the scanning conditions, crashing on the surface, pulsed high electric field, ...).
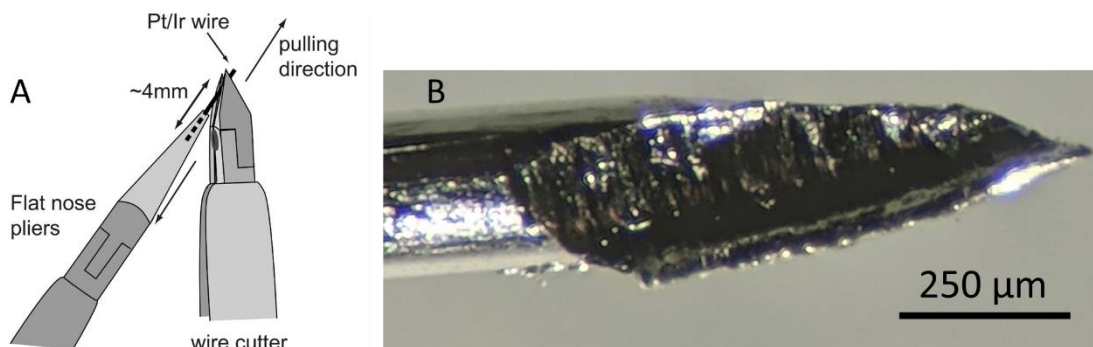
Figure 4.6. Diagram of the mechanical cut (A, adapted.[130]) and photograph of a PtIr tip prepared by mechanical cut (B).

Tips for STM under ambient condition are usually made of platinum or platinum-iridium to prevent any oxidation during the measurement. As pure Pt is soft (Mohs hardness 3.5), the Pt-Ir alloy allows higher stiffness and prevent mechanical deformations. Despite mechanical cut is a quick and easy method, the control over the final shape is difficult. Often empirical procedures are employed during the measurements to increase the sharpness of the scanning probe (i.e. quick variation in the scanning parameters, deliberate tip crash/scratch on the surface, exposing under high electric field). Ultimately the post-processing allows to further enhance the final resolution of images, however it can be more easily used for well-studied (and preferably flat) surface (i.e. HOPG, single crystals) since it can introduce significant artifacts.

4.2.2 STM tip preparation (electrochemical etching)

Tungsten tips are commonly used as probe for STM as they are cost-effective, exceptionally hard (Mohs hardness 7.5), and their preparation is relatively simple. However, the tendency to spontaneously generate oxides can contribute to surface contamination. Further, in aqueous environment, the release of tungsten is spontaneous under any condition (2.1.10). Generally, mechanical etching is not preferred to prepare tungsten tip as its brittleness makes it too challenging to achieve sharp features. By contrast, electrochemical etching is rather simple and does not require harsh conditions.[125]

The electrochemical etching is carried in alkaline environment and the overall electrochemical reaction is

$$W(s) + 2OH^- + 2H_2O \rightarrow WO_{4\,(aq)}^{2-} + 3H_2; \; E^0 = -1.43 \, V$$

(4.7)
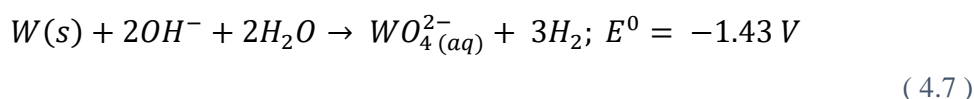
and it involves the formation of hydrogen bubbles and hydroxide reduction at the cathode and the oxidative dissolution of soluble tungstate anions at the anode. The surface tension of the electrolyte solution creates a meniscus around the wire which affects the final aspect and the shape of the tip. Additionally, the hydroxide diffusion to the anode generates a concentration gradient between top and bottom of the meniscus, resulting in a much faster etching rate at the bottom which generates sharper tips. Finally, the concentration of the electrolyte, other than the overpotential applied, influence the reaction as OH^- ions are consumed during the reaction, increasing the etching time required.[131] The process is schematised in Figure 4.7, however contrary to literature reports where the wire is completely immersed in the solution, in this work the etching is carried using a ring electrode which allows to form a lamella with the solution. Such setup allows to terminate the reaction immediately once the tip falls from the solution.
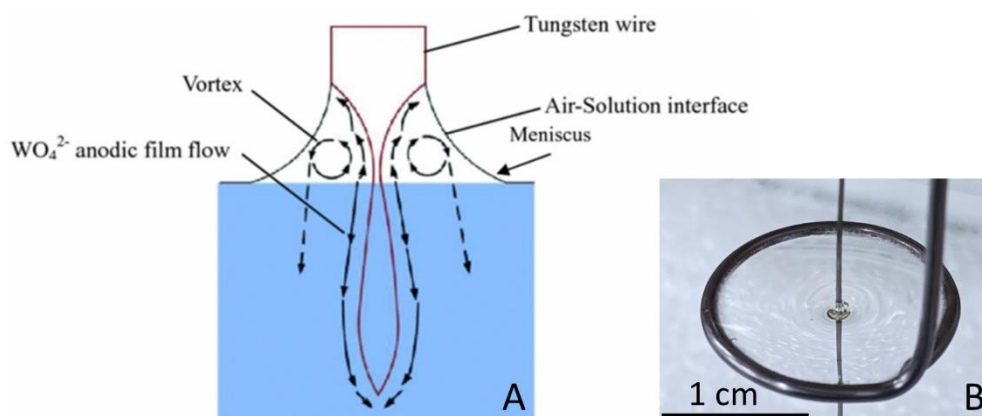
Figure 4.7. (A) Schematic of the anodic film flow during electrochemical etching of metal wire. The final sharpness of the tip is affected by the flow of OH⁻ ions and soluble species from the metal which generate a gradient that enhance the etching rate at the bottom of the meniscus. Adapted.[132] (B) Photograph of the setup used for electrochemical etching with the ring tantalum counter electrode.

Molybdenum can be electrochemically etched following the same procedure used for tungsten due to their similar behaviour in alkaline solution. As there are no reports in literature regarding the use of molybdenum for EC-STM measurements, the electrochemical etching has been used for tip preparation used for other SPM techniques.[66, 67, 133]

The overall electrochemical reaction is

$$Mo(s) + 2OH^- + 2H_2O \rightarrow MoO_{4\,(aq)}^{2-} + 3H_2; \; E^0 = -1.36\,V$$

(4.8)
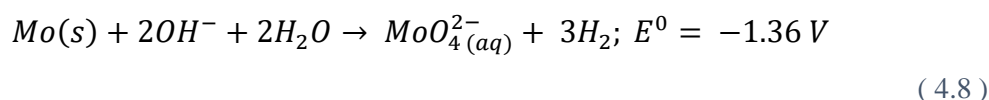
which involves the oxidative formation of soluble molybdate anions while molecular hydrogen in formed.[91, 93, 134, 135]

4.2.3 STM tip coating

For EC-STM, it is essential to minimise the surface area of the probes that comes in direct contact with the electrolyte, exposing only the very end of the tip to the solution. This is required to prevent the generation of excessive Faradaic current during the measurement. A greater exposed surface of the probe may generate significative current order of magnitude higher than the tunnelling current. This would cover the signal from the tip making impossible to generate meaningful images of the surface analysed. Therefore, the immersed portion of the tip in the electrolyte solution should possess excellent insulation properties, ideally leaving exposed only a small number of atoms at the extremity of the tip from which tunnelling occurs.
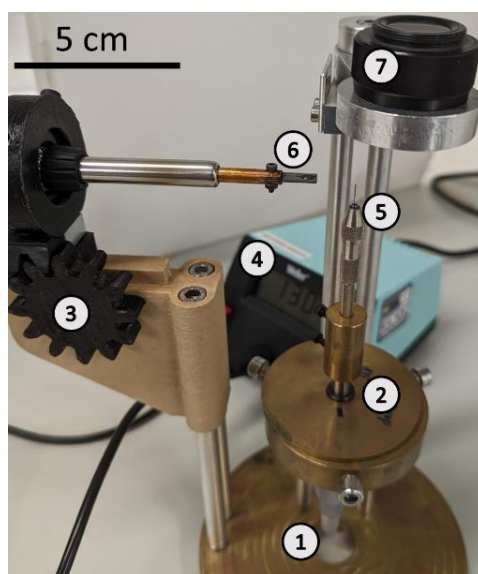
Figure 4.8. Coating station setup. ① Micrometric screw (vertical movement), ② positioning screws (plane alignment), ③ hot plate screw (horizontal positioning), ④ temperature control, ⑤ tip holder, ⑥ hot plate slit, and ⑦ magnification lens. Once the coating polymer is melted on the hot plate, the aligned tip is rapidly moved upwards through the slit. As the coating polymer cools down, the plate is moved away, and the tip is removed and stored.

There are a number of materials adopted for tip coating reported in literature (i.e., special varnishes, waxes, or polymers). Typically, the coating is selected based on the type of electrolyte used and the experimental conditions. In this work, different commercially available thermoplastic polymers with a melting point between 120 - 140°C were used. To apply the coating, the polymer is heated on a plate and the tip is inserted through once the correct temperature is reached. Figure 4.8 shows the setup of a coating station.

4.3 Experimental and computational details

4.3.1 Scanning tunnelling microscopy

STM measurements were conducted in ambient condition (T = 293 K, P = 1 atm) with an Agilent 5500 SPM instrument. The sample was mounted under the STM head (scanner), inside the environmental chamber to isolate it from the surroundings. All the measurements were conducted in constant-current mode.

The HOPG sample was mechanically exfoliated with tape before the measure to guarantee a clean surface. The tips were prepared from Pt/Ir wire (80%Pt/20%Ir, diameter 0.25 mm) by mechanical cut. In the images, the bias voltage refers to the substrate.

4.3.2 Electrochemical scanning tunnelling microscopy

The bipotentiostat of the Agilent 5500 SPM instrument allows for electrochemical STM (EC-STM) measurements. The cell components were cleaned in 20% HNO_3 and rinsed before the use. A perfluoro elastomer O-Ring (Kalrez®) was placed between the hollow cell (made of Kel-F® (polychlorotrifluoroethylene, PCTFE) a fluorocarbon-based polymer) and the sample to prevent any leakage of the electrolyte. The cell was electronically insulated from the sample holder and kept in position with a spring lock system. Platinum wires were used for the counter and reference electrodes, which were flame annealed before assembling the cell. The scanning tip (W, Mo) was prepared by electrochemical etching and coated (4.3.3). All the measurements were conducted in constant-current mode. Any image post-processing was carried with ImageJ[136] (STM-specific plug-in), Gwyddion[137], and WSxM[138].

The solutions were prepared using perchloric acid (70%, purity 99.99%, Thermo Fisher), sulfuric acid (purity 99.99%, Alfa Aesar), potassium iodide (purity 99.995%, Merck) and ultrapure water (Millipore).

The Au(111) single crystal used as working electrode was prepared with the flame annealing method. In addition to removing organic contaminants, flame annealing promotes the formation of larger atomically flat terraces allowing more reproducible imaging.[139, 140] The crystal was heated with a butane torch on a ceramic plate for 10 minutes to a bright orange colour, followed by cooling down to room temperature before it was assembled in the cell and immediately filled with the electrolyte solution. The EC-STM cell was completed with two platinum wires used as counter and quasi-reference electrode. All potentials in the EC-STM images are referred to the Pt quasi-reference electrode potential.

4.3.3 STM tip preparation

Tungsten and molybdenum tips were prepared following the same procedure, consisting of electrochemical etching in NaOH 2M (diluted from a stock 5M solution, Sigma-Aldrich). The metal wires were cleaned using wetted filter paper to remove any external particles from the surface and rinsed with milliQ water. Approximately 15 mm of metal was placed inside a tantalum loop used as a counter electrode, its shape allows to form a lamella with the electrolyte solution (Figure 4.7). A voltage of 3 V (50 Hz AC) was applied between the two electrodes (for approximately 10 minutes) until the tips fall on the sample holder underneath the ring electrode. The tip was rinsed in milliQ water and dried before placing in the coating station where it was rapidly passed through the melted commercial thermoplastic polymers (Certis Benelux) at 140 °C. The tip is then visually under a microscope and any excess of glue removed. Finally, the tips were stored before the use for EC-STM measurements, and any leaking current verified directly in the EC-STM cell prior to the imaging.

4.3.4 h-BN/Rh(111) nanomesh

Hexagonal boron nitride on single crystal rhodium (h-BN/Rh(111), nanomesh) is produced on 10 cm wafer with a specialised setup at the Physik Institute of the Universität

Zürich.[110] The sample substrate is formed by a 150-nanometer thick crystalline Rh(111) film grown on a 40-nanometer thick yttria-stabilized zirconia (YSZ) buffer layer on the Si(111) wafer. Before the boron nitride deposition, any contamination or defects is removed by a thorough cleaning procedure. The single layer is formed, in UHV and at substrate temperature above 750°C, with a self-terminating process by chemical vapour deposition (CVD) using borazine $(HBNH)_3$ as a precursor. Figure 4.9 shows the final surface, characterised by a threefold geometry of the rhodium film substrate and hole-like structures with a diameter of approximately 0.25 µm and depth ranging from 1 to 5 nm, attributed to artefacts from the coalescence of islands.[110]
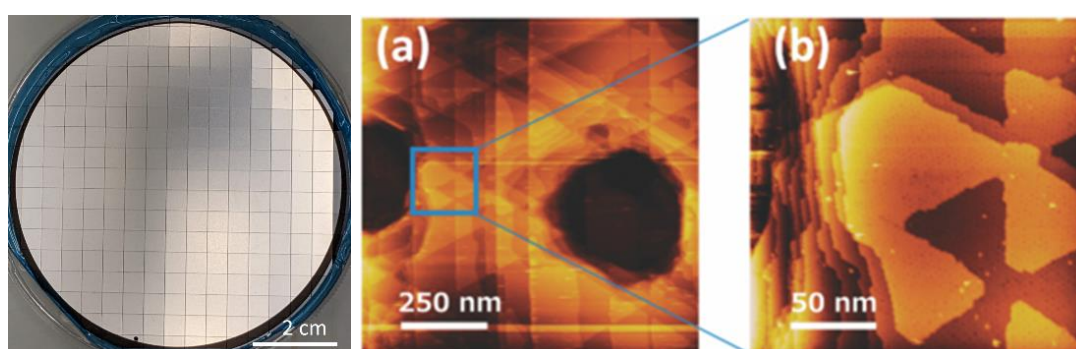
Figure 4.9. Photograph of pre-cut 10-inch wafer. Threefold geometry of the Rh substrate visible at room temperature: (a) STM image of the nanomesh, and (b) magnification. $V_b = 1.0V$, $I_t = 0.5$ nA. Adapted.[110]

In a clean room, the 10 cm wafer is subsequently covered with a polymer film to protect the surface from contamination and cut in smaller samples (5x5 mm^2). The protective layer was UV cured and removed immediately before assembly the electrochemical cell for the EC-STM measurements. Figure 4.10 shows a large-scale EC-STM images of the pristine nanomesh and the same sample with impurities deposited on the surface after multiple uses.
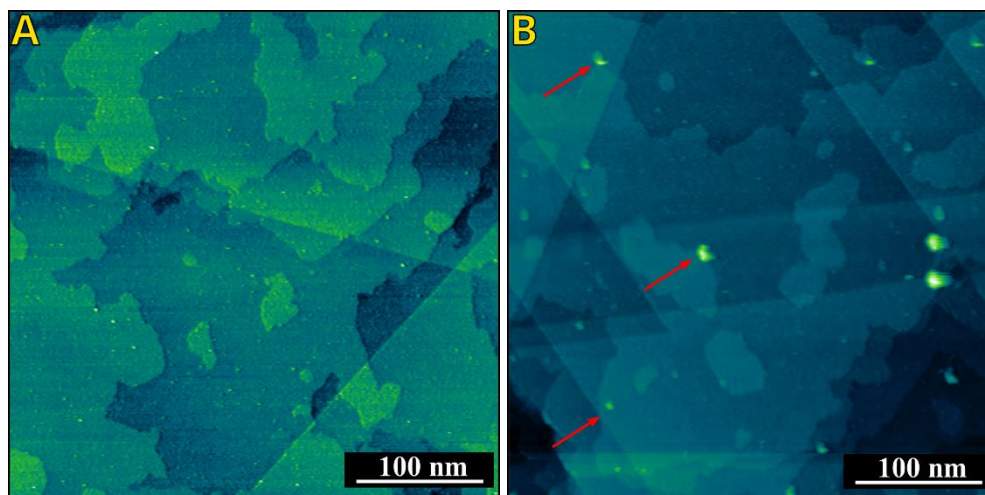
Figure 4.10. EC-STM images of h-BN/Rh(111) nanomesh in 0.1 M HClO$_4$ measured with tungsten tip (V$_b$ = +0.5 V, E$_{sub}$ =0.0 V vs Pt, I$_t$ = 1.0 nA). Difference between a clean surface (A, new sample) and a surface with impurities (B, sample after weeks of imaging with red arrows highlighting some of the multiple impurities).

4.3.5 Computational methods

In collaboration with Dr Marcella Iannuzzi's group at the University of Zürich (Switzerland), we performed computational calculations to describe the tungsten and molybdenum oxides and their interaction with the surface of interest. Dr Iannuzzi's group is primarily focused on computational research of 2D materials (e.g. graphene, metals) and processes occurring at interfaces[141, 142, 143, 144, 145, 146]. Over the past decades, they developed and optimised models[147] in particular for the subject of our interest, h-BN (hexagonal-boron nitride). The group studied the boron nitride deposited on metals[148] and its interaction with various species in UHV[40, 142, 143, 149, 150, 151].

During the Covid-19 related lockdown, we carried out a variety of calculations to optimise the structure of tungsten and molybdenum oxides at different charge states (neutral, single and double negatively charged). Afterwards, we focused on the interaction and configuration of such clusters as they approached the surface in aqueous environment. The calculations allowed to model and provide a plausible explanation on how the clusters interact with the h-BN surface, and how the interactions might affect their behaviour in different environments.

The geometry optimisations at the density functional theory (DFT) were carried with the computing cluster in based in Zurich University (UZH) using the CP2K package.[147, 152] For the calculations, it was employed the norm-conserving Goedecker Teter Hutter (GTH)[153] pseudo-potentials and the Perdew Burke Ernzerhof (PBE)[154] exchange correlation functional. For all elements, the basis sets of polarised double-zeta valence short range Molopt (DZVP)[155] were adopted. The PBE-rVV10 functional[156] was used to account for dispersion forces. The unit cell for the h-BN/Rh(111) is made of a 13x13 boron nitride layer on top a 12x12 Rh atoms.[38]

4.4 Results and discussion

4.4.1 STM tip coating

The coating protocol for coating tips for EC-STM using thermoplastic polymers in literature is often generically described as it requires in-house system, therefore it require additional investigation to find a reliable and effecting procedure for coating of molybdenum tips. The lower hardness of the metal compared to tungsten, combined to a more elongated shape contribute to improperly coating or bent apex. Several thermoplastic polymers with different physical characteristics were tested to identify the most suitable for the two metals and ensure proper insulation. Additionally, the aim was to optimise the operational conditions, such as operative temperature and the amount of substance used, without compromising the integrity of the metal probe.

Product code	Viscosity (Pa·s)	Softening point (°C)	Curing time* (s)	Appearance
12-101	6.5 @200 °C	75	5	Transparent
12-102	5.0 @200 °C	82	7	Transparent/white
12-103	6.5 @190 °C	80	5	Straw yellow
12-107LM	3.0 @160 °C	85	5	Solid white

Table 6. Main experimental parameters provided by the manufacturer (Certis Benelux) for the thermoplastic polymer tested for tip coating (Curing time: time required to completely solidify the polymer at room temperature following its complete melting.)

Table 6 summarises the main characteristic of the polymers used (shown in Figure 4.11a). The materials provided by the manufacturer (*Certis Benelux*) are based on

ethylene-vinyl acetate copolymers; however, as the exact composition is undisclosed, they are identified by their product code.

The temperature control of the slit on which the polymer is deposited on the coating station does not allow for a precise temperature value, therefore the polymers were tested in two temperature ranges: close to (≈ 5 °C) and higher (≈ 30 °C) than the observed melting point. The coated tips were visually inspected with optical microscopy and then tested in the EC-STM cell by measuring the Faradaic current prior to imaging.

Generally, the tips coated by melting the polymer at higher temperatures showed high Faradaic currents, indication of an insufficient insulating layer and the incomplete covering of the apex. These results were expected as higher temperatures resulted in longer time required for solidification which, combined with lower viscosity, increases the de-wetting of the tip apex (i.e. Figure 4.11d).

For tungsten tips, the best results were obtained at lower temperatures and by using a minimal amount of polymer to reduce initial resistance. Among the four polymers used, both sample 12-102 and 12-103 became very sticky after solidification, increasing their tendency to attract impurities on the surface and possibly leading to potential issues during the measurements and contamination in the electrolyte. Despite the good results with polymer 12-107, its limited temperature range was not ideal as it could easily reach burning point. Therefore, the procedure was optimized using polymer 12-101, which exhibited the best overall characteristics and versatility.

The coating procedure for the molybdenum required additional optimisation as the weaker apex was more easily bend during the process (Figure 4.11b, shows the apex bend and trapped inside the polymer resulting from the use of the same parameter as tungsten). The best solution was to reduce the polymer viscosity by slightly increasing the temperature and therefore reduce the mechanical resistance to the tip. To compensate a faster de-wetting due the increased temperature, a larger quantity of polymer was used on the plate. The final "bulkier" shape of the tips showed sufficiently low Faradaic current to allow for EC-STM imaging.
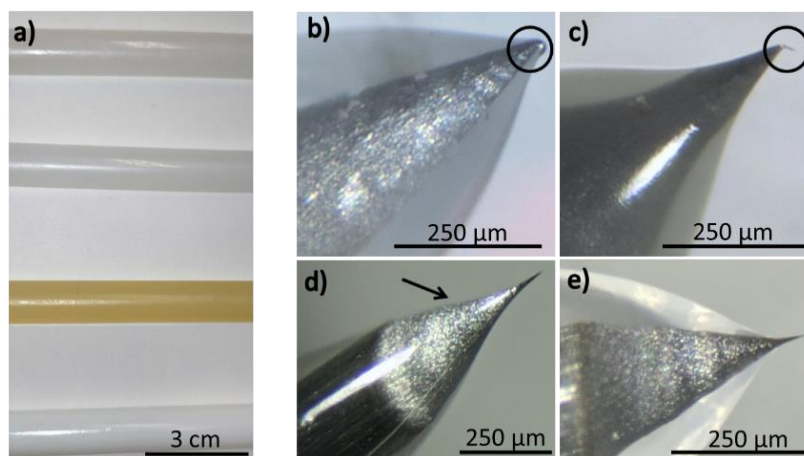
Figure 4.11. Picture of the different thermoplastic polymer tested (a). Pictures of tips ruined during the coating (b, Mo tip bent and trapped in the polymer, and c, W tip). Pictures of Mo tip undercoated (d) and Mo tip properly coated (e).

4.4.2 STM optimisation (noise removal)

To achieve atomic resolution, especially under ambient conditions, it is necessary to minimise any interference that could result in poor imaging. The most common distortions, thermal expansion (thermal drift), and nonlinearities in the piezoelectric actuator (hysteresis and creep), mainly occur along the slow-scan direction. In principle, their contribution can be quantified and eliminated from any images in post-processing, if the analysed surface has a known periodic structure. However, attenuating any source of possible noise allows better image resolution and reproducible results.

Initially the instrument showed two types of periodic distortions occurring unpredictably ("high" and "low" frequency, examples in Figure 4.12). Due to the excessive noise, any attempt to remove distortions through post-processing was not successful, as it resulted in a significant loss of information in the final image. Therefore, to identify the source and further optimise the instrumental setup, well-known surfaces were imaged (i.e. highly oriented pyrolytic graphite (HOPG), and single crystal gold).
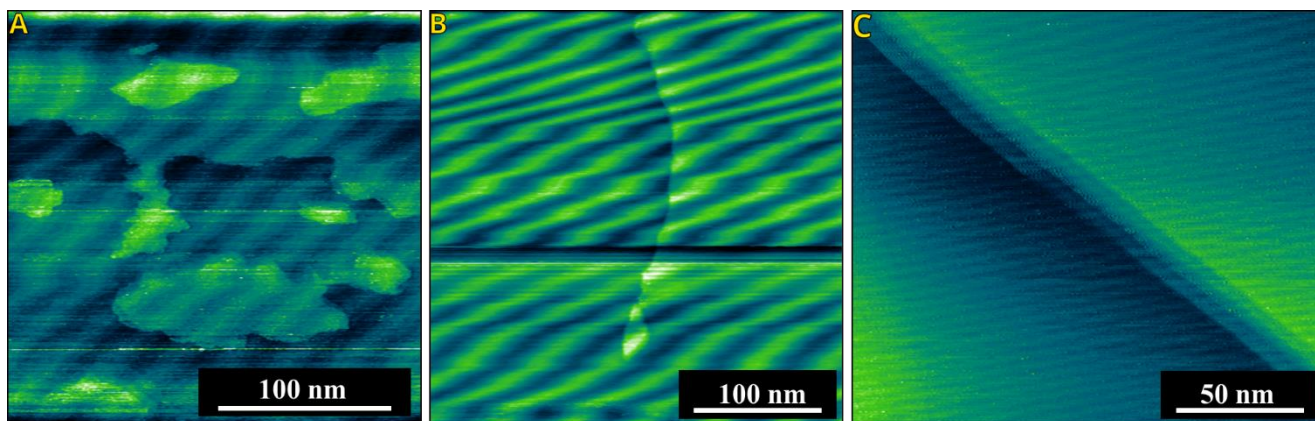
Figure 4.12. low frequency noise in (A, B) EC-STM images of Au(111) in 1 mM KI + 5 mM H_2SO_4 $I_t = 1.81$ nA, $V_b = +0.45$ V, $E_{sub} = -0.05$ V vs Pt. (B) high frequency noise affecting an STM image of HOPG measured with PtIr tip in air, $I_t = 0.1$ nA, $V_b = +0.70$ V.

The distortions observed on the sample appeared unpredictably during imaging, while the features of the noise propagation systematically changed only along the slow-scan direction. Additionally, the noise was never affected by variations in the scanning area or scanning speed, confirming it was originated from external contributions rather than features of the sample itself. The fast Fourier transform (FFT) allowed to measure the frequency of the noise which however varied in a broad range (49 to 401 Hz). To reduce sample vibrations, noise-cancelling foam was employed, the chamber was grounded to shield against possible electromagnetic noise. However, these measures did not improve the obtained images.

Eventually, the source of the issue was identified in the cooling fan spinning inside one component of the head electronic box (HEB). The vibrations from the fan were carried into the chamber, influencing the scanner during the measurements. Figure 4.13 shows the change of the setup which allowed to remove the noise and most of the distortion from the images. The two components of the HEB were separated physically and with the use of insulating and damping materials (foam and box in the picture). The cable entering the chamber was oriented to hamper any vibration with the use of foam to lock its position in the aperture of the STM chamber.
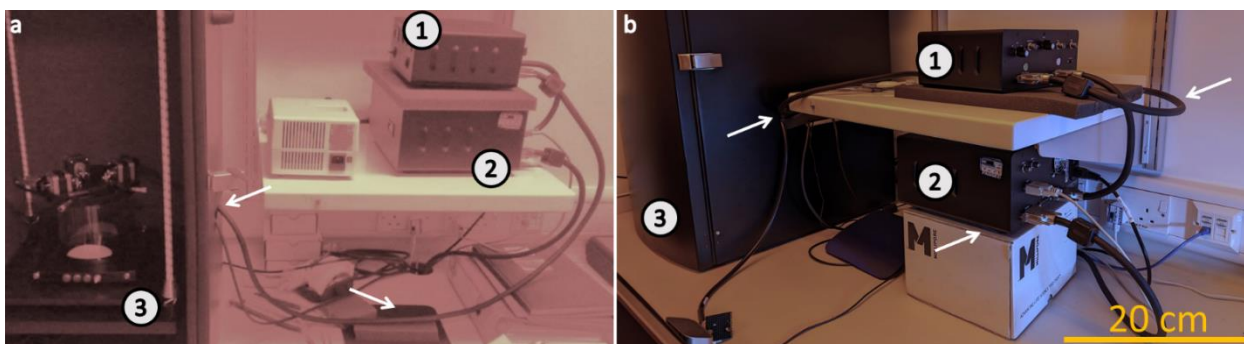
Figure 4.13. Initial a) and final b) configuration of the head electronic box (HEB). The two components are separated as the vibration from the fan (HEB component ② is carried to the HEB component ①) and inside the chamber ③ via the cable to control the scanner (arrows).

Figure 4.14 shows the increase of the resolution using the HOPG and single crystal gold (as in Figure 4.12) reached the noise was reduced with the new HEB setup. To highlight the increase in the lateral resolution obtained after the STM optimisation, we avoided extensive use of post-processing tools (i.e. the images were only processed with mean plane subtraction, colour correction and crop). In Figure 4.14 (A) the regular atomic pattern of the HOPG is measured with atomic resolution. Due to thermal drift the lattice of HOPG is compressed, as shown in the FFT (a compressed hexagonal structure instead of a regular hexagon). In Figure 4.14 (B) the Moiré pattern formed by the adsorbed iodine monolayer (in a limited potential window) is imaged. The lateral resolution reached allowed also to detect the fluctuations in the gold step edges, promoted from the interaction with the iodine adsorbate.[157]
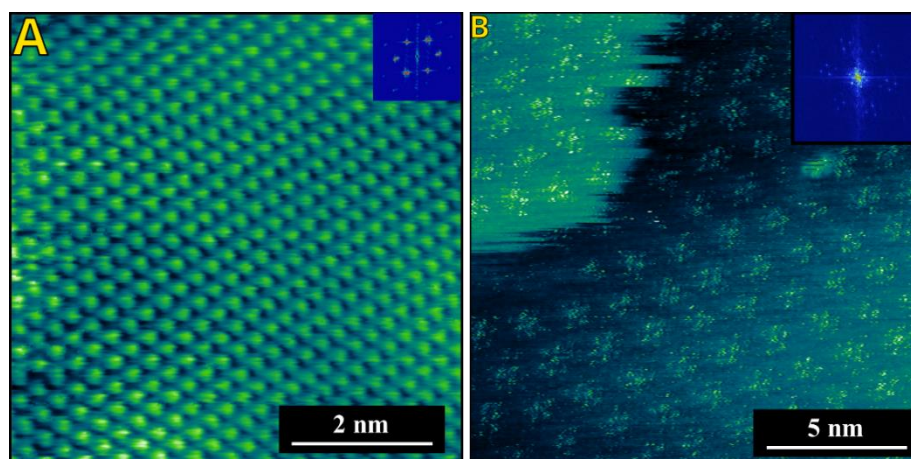
Figure 4.14. (A) STM image of HOPG measured with PtIr tip in air (I_t = 2.0 nA, V_b = +0.80 V). (B) EC-STM image of the of the Au(111) Moiré pattern in 1mM KI + 5 mM H_2SO_4 (I_t = 1.81 nA, V_b = +0.44 V, E_{sub} = -0.04 V vs Pt). following the optimisation and noise reduction.

4.4.3 Imaging hBN nanomesh exposed to W oxide clusters with W tips

Figure 4.15 shows the results from the structure optimisation for the (mono-, and bi-) negatively charged oxide tungsten and molybdenum clusters. The results were compared to previous work[60] to verify the reliability of the model and approximations employed.

The anionic forms of both the metals (respectively, the singly occupied molecular orbital (SOMO) for the monoanion and the highest occupied molecular orbital (HOMO) for the dianion is characterised by d-orbitals overlapping, resulting in a complete delocalisation of the metal-metal bond (d-orbital aromaticity) which increases the stability of the anions.[60, 158, 159, 160, 161, 162]
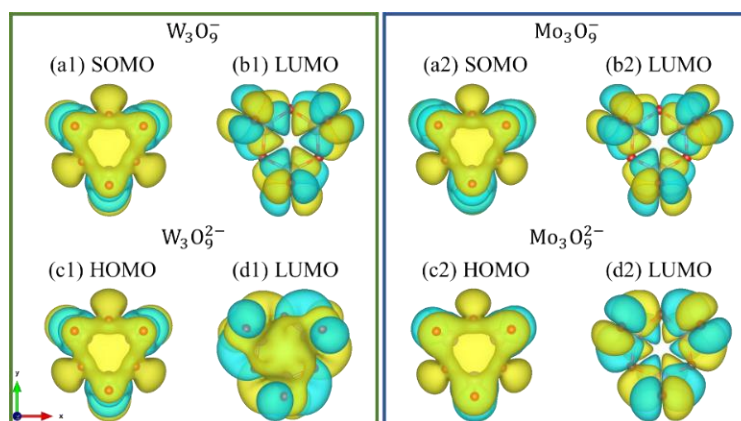
Figure 4.15. Electron density states of the molybdenum (Mo_3O_9) and tungsten (W_3O_9) oxides from DFT simulation visualised with VESTA[163] (positive, yellow; negative, blue). The electron delocalisation occurs for both the single and the double anions of the metal (a) Singly occupied molecular orbital (SOMO) and b) highest occupied molecular orbital (HOMO) while their respective lowest unoccupied molecular orbitals (LUMO) show strong character.

Initially, tungsten probes were used to image the nanomesh surface to assess the instrument in comparison with results in literature. Figure 4.16 shows a preliminary image obtained in similar conditions as previously reported.[64] The spontaneous oxide generated from the tungsten tip adsorbed on the pores are visible as triangular features grouped together in Figure 4.16. However, significant background noise and thermal drift lowered the final resolution, hindering any optimisation through post-editing. The distance between pores is approximately 3nm, corresponding to the corrugation of the nanomesh. We attempted to reproduce the progression of the spontaneous self-assembly process of the tungsten oxide clusters in the nanomesh pores and their dynamic behaviour while they

saturate the surface, as previously reported.[64] However, the probes did not allow to obtain a sequence of reproducible high-resolution images as they were often not stable for the required long acquisition time. Despite the limitations that prevented submolecular imaging of the cluster, Figure 4.16 shows pores filled with a variable population of tungsten oxides (up to nine clusters per pore). The cross-sectional profile of three pores shows changes in apparent height attributed to the clusters.
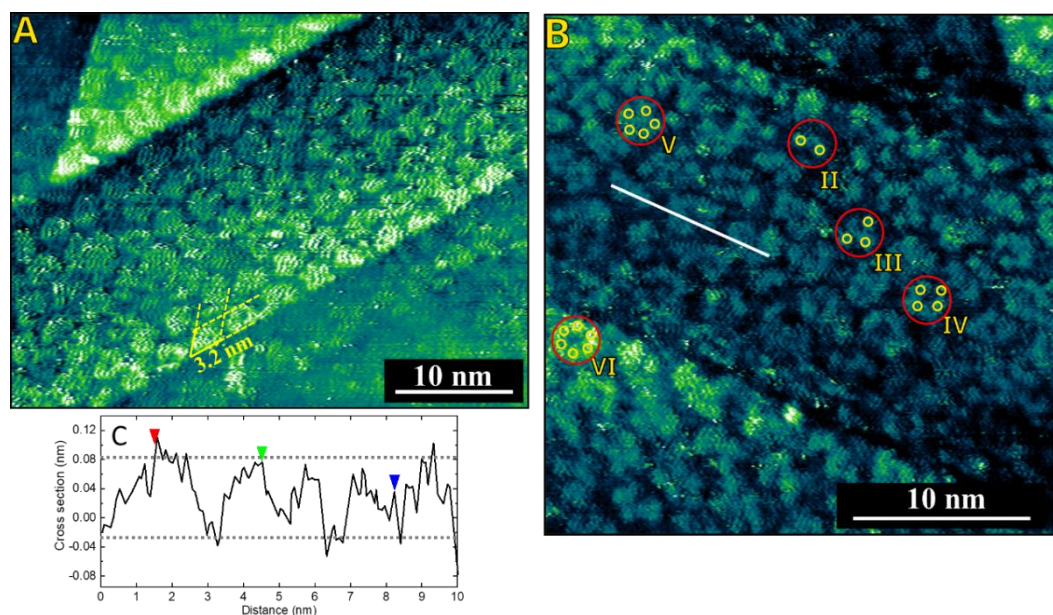
Figure 4.16. EC-STM measured with tungsten tip, images of h-BN/Rh(111) nanomesh in 0.1 M $HClO_4$ with tungsten oxide clusters adsorbed in the pores (A) I_t = 1.31 nA, V_b = +0.46 V, E_{sub} = -0.13 V vs Pt, and (B) I_t = 3.6 nA, V_b = +0.46 V, E_{sub} = -0.13 V vs Pt. Highlighted in (B) pores filled with different numbers of clusters. (C) Cross-sectional profile along the white line in (B), the arrows are spaced by 3.2 (±0.1) nm.

Figure 4.17 shows an image reported in literature with the desired lateral resolution which allows to distinguish between submolecular features of the oxide clusters. The clusters are adsorbed in two orientations relative to the nanomesh rhombic unit cell and the pores are filled with variable number of clusters as observed in Figure 4.16. Although at this stage we did not achieve similar resolution, we begin the imaging using molybdenum tips following the same protocol to assess any differences.
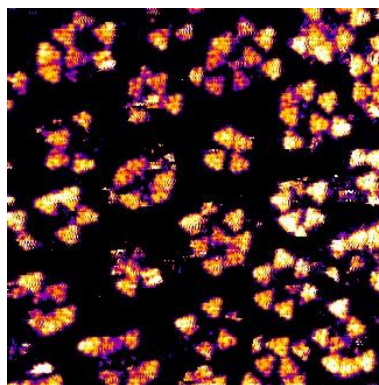
Figure 4.17. EC-STM image of h-BN/Rh(111) nanomesh in 0.1 M HClO$_4$ with W oxide clusters adsorbed in the pores (12×12 nm^2, $V_b = +0.12$ V, $E_{sub} = 0.3$ V vs NHE). With pores arranged in a hexagonal pattern having the centre distanced 3.2 nm. Each triangle consists of 6 submolecular features. Adapted.[64]

4.4.4 Imaging hBN nanomesh exposed to Mo oxide clusters with Mo tips

As described in 4.4.1, molybdenum tips are generally more difficult to prepare and use for imaging. Compared with tungsten, the molybdenum generates thinner and sharper tips when prepared with electrochemical etching. The extreme sharpness combined with a lower hardness (Mohs hardness of 5.5, compared to the tungsten's Mohs hardness of 7.5), resulted in a more challenging and less efficient coating process which required additional care as described in 4.4.1. Moreover, the limited electrochemical stability window due to the transpassive behaviour easily observed for small potential increment (2.3.2), limited the potential window available during the EC-STM measurements (Figure 4.21). However, we believe that over time the mechanism responsible for the cluster generation influenced the tip shape (and more importantly, its sharpness), increasing the lateral resolution, allowing for adequate imaging. Figure 4.18 shows a large-scale image of nanomesh, with the triangular symmetry of Rh (as in Figure 4.10), the larger pores (defects originated from the surface synthesis, as opposed to the nanomesh pores with 3.2 nm diameter not visible in the image) and the terraces are identifiable.
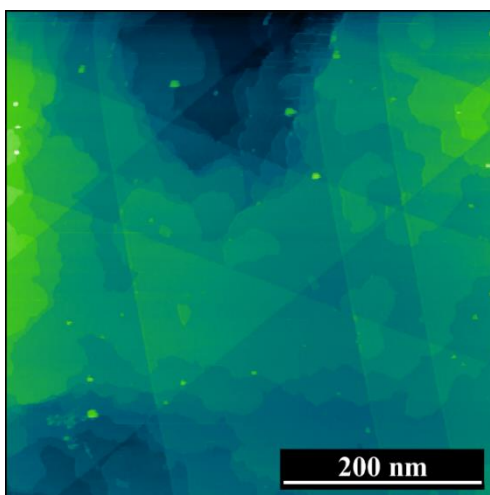
Figure 4.18. EC-STM image of h-BN/Rh(111) nanomesh in 0.1 M HClO$_4$ with molybdenum tip (I$_t$ = 0.8 nA, V$_b$ = +0.40 V, E$_{sub}$ = -0.2 V vs Pt).

Following the initial positive results with molybdenum probes for STM imaging under electrochemical conditions, we achieved sufficient lateral resolution to observed the nanomesh pores. In Figure 4.19 the nanomesh is fully populated by clusters distanced 3.2 nm, as displayed in the cross-sectional profile (Figure 4.19B). Since the sample was only exposed to molybdenum, we assume the pores were filled exclusively with molybdenum oxide clusters, confirming its deposition on the surface with XPS measurements (3.3.3).
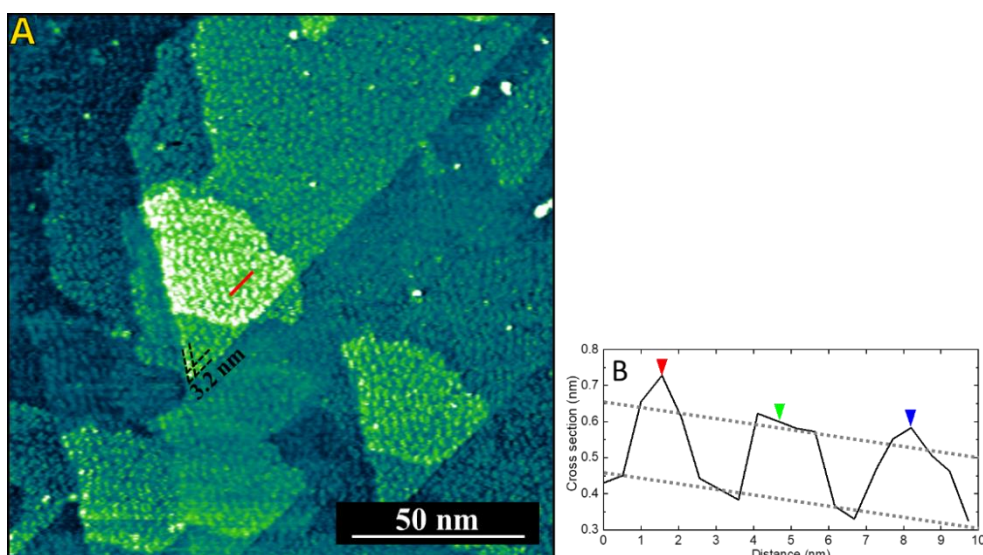
Figure 4.19. (A) EC-STM image of h-BN/Rh(111) nanomesh in 0.1 M HClO$_4$ with Mo tip. Oxide clusters adsorbed in the pores (I$_t$ = 0.8 nA, V$_b$ = +0.50 V, E$_{sub}$ = -0.1 V vs Pt). (B) Cross-sectional profile along the red line in A, the arrows are spaced by 3.2 (±0.1) nm.

Despite encouraging results at larger scale, the short-term stability of the molybdenum tips prevented imaging at smaller scales. Good lateral resolution was quickly lost while scanning, required long time to recover (when and if possible) the proper scanning conditions. Generally, for recovering the probes to a suitable resolution, the tip had to be scratched/tapped lightly on the surface (i.e., by overcorrecting the feedback loop, by moving across the sample while scanning).

4.4.5 Imaging hBN nanomesh exposed to Mo oxide clusters with W tips

The *in silico* optimised tungsten and molybdenum oxide structures results were used to simulate the interaction with the nanomesh surface to determine the favoured configuration and evaluate any effect of capping water ($W_3O_9 \cdot 3H_2O$) on the adsorption energy. The optimal configuration of the density of states of tungsten and molybdenum oxide clusters are compared in Figure 4.20. The two oxide clusters shows different features, especially in the region of the HOMO energy, between -4 and -2 eV, in combination with the clear peak shift (roughly 80 meV) gives the possibly to distinguish between the two clusters by controlling the bias voltage (Figure 4.3).
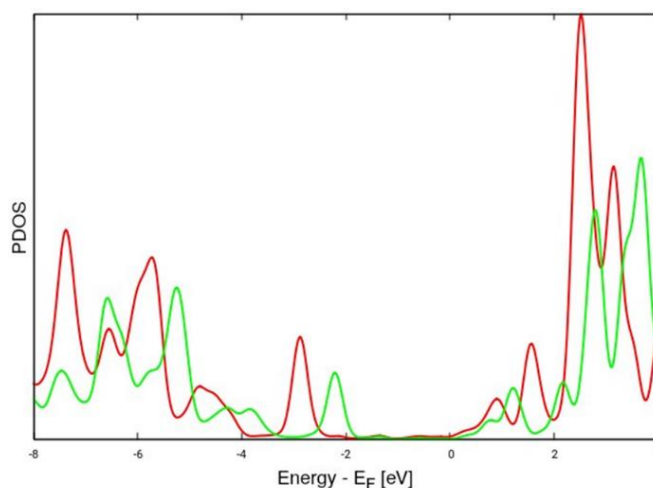
Figure 4.20. Density of states projected on the wavefunctions of the W_3O_9 (red) and Mo_3O_9 (green) clusters adsorbed in the pores of the h-BN/Rh(111) nanomesh.

Due to the slight difference in the energies of the HOMO and LUMO of tungsten and molybdenum oxide clusters, the next objective was to distinguish between the species deposited on the nanomesh by means of potential control. However, is not clear if the oxide generated from the metal probe during the imaging is adsorbed only in its vicinity

or if over time the clusters tend to diffuse over macroscopic distances until the surface becomes completely saturated. Consequently, as there is no precise control over the exact position of the tip every time it is replaced (in particular when W tips are used after imaging with Mo tips, or *vice versa*), we cannot guarantee that the clusters imaged following an initial generation/deposition are not generated by the replaced metal. For this reason, we exposed the surface to long periods of time (more than 8 hours) to simulate EC-STM scanning conditions before employing the opposite metal. Accordingly, the nanomesh was initially imaged with Mo tips and once the surface was saturated, a tungsten probe was used to investigate any possible difference in the images if any tungsten cluster deposited or partially replaced the decorated surface.

Figure 4.21 shows the theoretically accessible substrate bias (as the difference between sample and tip potential) resulting from combining the electrochemical windows for both the surface and the tip used. The nanomesh is limited by its oxidation at positive potentials (not shown in the figure as it occurs at potential higher than 0.7 V vs Ag/AgCl) and hydrogen intercalation at negative potentials which could result in an irreversible damage.[44] The potential allowed for the tips are in first approximation limited by the hydrogen evolution and the anodic oxidation of the metal. However, as the Faradaic current during the EC-STM measurements needs to be negligible the allowed range is considerably more restricted, and it needs to be tested directly during the experiment as it varies with the specific shape and coating of the tip used.

In principle as the tungsten has a wider stability range than molybdenum (2.3.2), it enables a greater variation in substrate bias, and therefore it may better enable the differentiation between the clusters of the two metals, for instance, by "turning off" a cluster due to insufficient bias voltage to achieve tunnelling currents. The nanomesh was imaged using the tungsten tip following a long exposure to molybdenum. Figure 4.22 shows the surface fully populated by cluster however the small lateral resolution limits the detection of the single oxide distributed inside the single pores. In the experimental condition is not possible to determine which metal oxide is populating the surface.
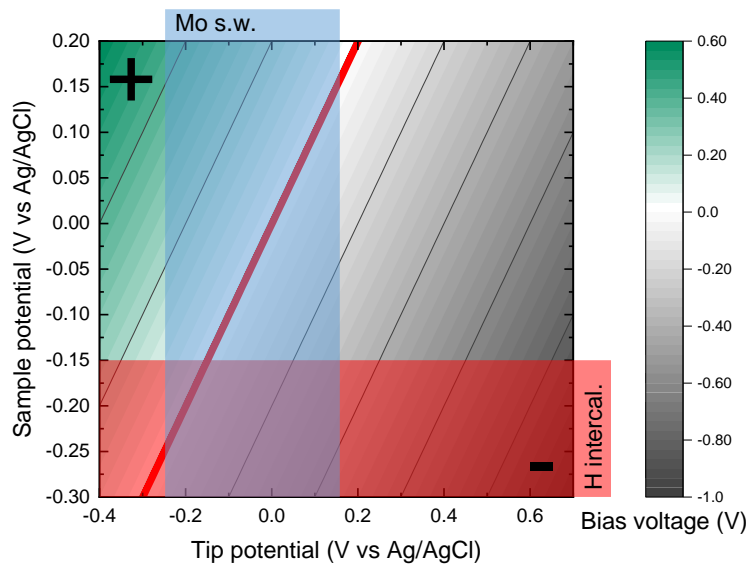
Figure 4.21. Visualisation of accessible substrate bias (as difference between sample and tip potentials) obtained from the potential limits of the sample (hBN nanomesh) and the tungsten or molybdenum (blue rectangle) tips. For V_b= 0 V (red trace) no tunnelling can occur.

Figure 4.22 EC-STM images of h-BN/Rh(111) nanomesh in 0.1 M HClO$_4$ following Mo oxide deposition measured with W tip (A) I_t= 2.0 nA, V_b= +0.50 V, E_{sub}= 0.0 V vs Pt, and (B) I_t = 2.0 nA, V_b = +0.50 V, E_{sub} = 0.0 V vs Pt. (C and D) Cross-sectional profiles along the white lines in (A) and (B), the arrows are spaced by 3.2 ($\pm$0.1) nm.

The instability resulting from a continuous variation of experimental parameters often contributed to a rapid loss of resolution and, ultimately, prevented obtaining a sequence

of clear and comparable images, particularly at high magnifications. Nevertheless, Figure 4.23 shows the presence of triangular structures representing the oxide clusters trapped in the nanomesh pores. However, the quick loss of resolution prevented further variation in the tunnelling conditions and an attempt to distinguish between tungsten and molybdenum oxides. In contrast with images with better resolution (Figure 4.17) it is more challenging to appreciate the cluster distribution within the pores. Despite all the limitations discussed, in the image we still recognise the only two clusters orientation relative to the nanomesh rhombic unit cell. This could potentially allow for the differentiation between the two types of clusters. However, the image is also affected by double-tip artefacts complicating any hypothesis.

Figure 4.23 EC-STM image of h-BN/Rh(111) nanomesh in 0.1 M HClO$_4$ following molybdenum oxide deposition measured with W tip (I$_t$ = 3.0 nA, V$_b$ = +0.50 V, E$_{sub}$ = 0.0 V vs Pt). Two orientations (red and blue triangles) of the oxide clusters relative to the rhombic unit cell. (B) Cross-sectional profile along the red line in (A), the arrows are spaced by 0.8 (±0.1)nm.

4.4.6 Imaging hBN nanomesh exposed to W oxide clusters with Mo tips

Following the same approach as in the previous section (0), after exposing and imaging the nanomesh with tungsten tips for several hours, a molybdenum probe was employed to detect any difference between the two oxide clusters. The smaller stability window of molybdenum limited the potential range available for searching for ideal EC-STM conditions, resulting in a more challenging process. The image Figure 4.24 shows the presence of oxide clusters, however, as discussed in the previous section, it is not possible

94

to unambiguously assign their origin to either material (the surface may be populated with only tungsten following the initial deposition, only molybdenum if the deposition occurs only in the vicinity of the scanning tip, or a combination of the two metal oxides). The lateral resolution of the molybdenum tips however allowed to image with greater detail the clusters as it is possible to recognise single clusters and their orientation with respect to the nanomesh rhombic unit cell (similar to the results with tungsten tips, as shown in Figure 4.17, and Figure 4.23).
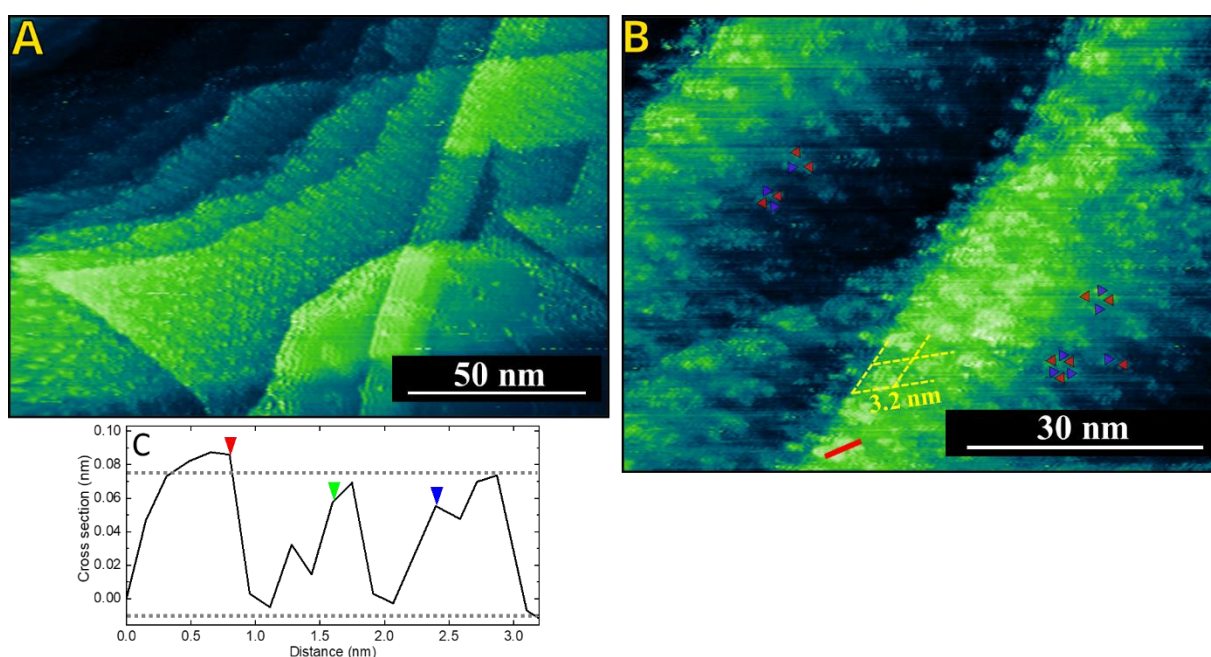
Figure 4.24. EC-STM images of h-BN/Rh(111) nanomesh in 0.1 M HClO$_4$ following tungsten oxide deposition measured with molybdenum tip (A) I_t = 3.5 nA, V_b = +0.48 V, E_{sub} = -0.09 V vs Pt, and (B) I_t = 3.5 nA, V_b = +0.48 V, E_{sub} = -0.09 V vs Pt. In (B), Two orientations (red and blue triangles) of the oxide clusters relative to the rhombic unit cell. (C) Cross-sectional profile along the red line in (B), the arrows are spaced by 0.8 ($\pm$0.1) nm.

Result with high lateral resolution were obtained over multiple days despite facing the same instability problem which prevented the acquisition of series of images or testing within a range of potential. Figure 4.25 clearly shows the presence of clusters on a large scale, however, any attempt to focus on a smaller scanning area resulted in loss of tip resolution. The cross-sectional profile over three partially filled pores shows how they tend to deposit at the edges (as reported in literature both in UHV and electrolyte, Figure 1.10) before saturating the available space (as noticeable in the cross-sectional profiles in Figure 4.22C, D).
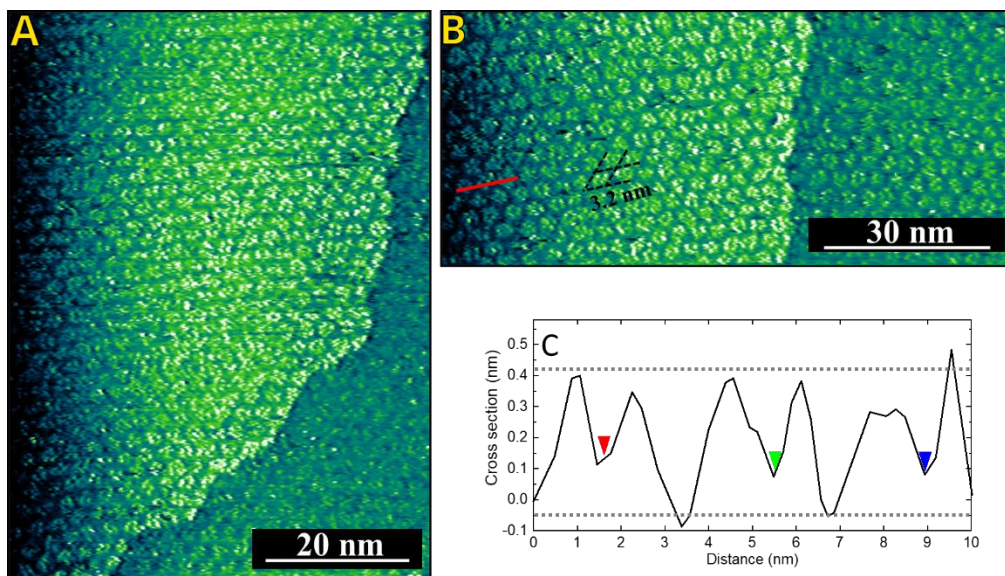
Figure 4.25. EC-STM images of hBN/Rh(111) nanomesh in 0.1 M HClO$_4$ following tungsten oxide deposition measured with Mo tip (A) $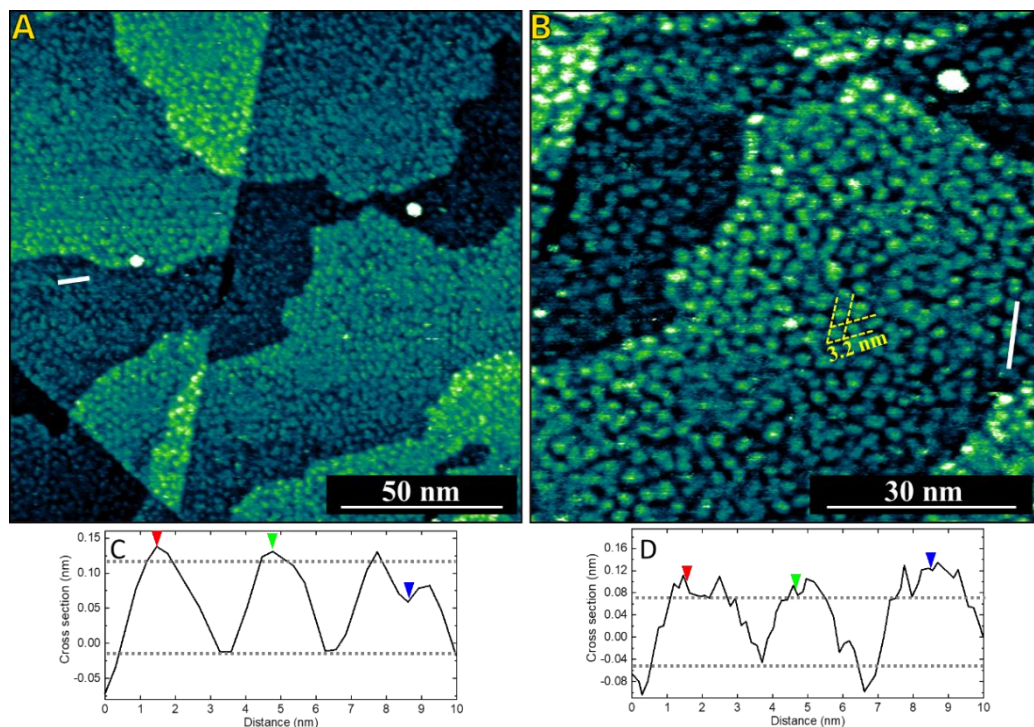I_t$ = 0.5 nA, V_b = +0.50 V, E_{sub} = -0.09 V vs Pt, and (B), I_t = 0.5 nA, V_b = +0.50 V, E_{sub} = -0.09 V vs Pt. (C) Cross-sectional profile along the red line in (B), the arrows are spaced by 3.2 (±0.1) nm.

To provide better insight into instability of the tips, Figure 4.26 shows the image obtained with the same sample and tip after the lateral resolution of the probe was recovered hours later, which prevented valuable insight about the evolution of the surface. Despite the level of the resolution (compared with Figure 4.25) was never recovered (or improved) it is possible to generate cross-sectional profiles of the nanomesh pores.
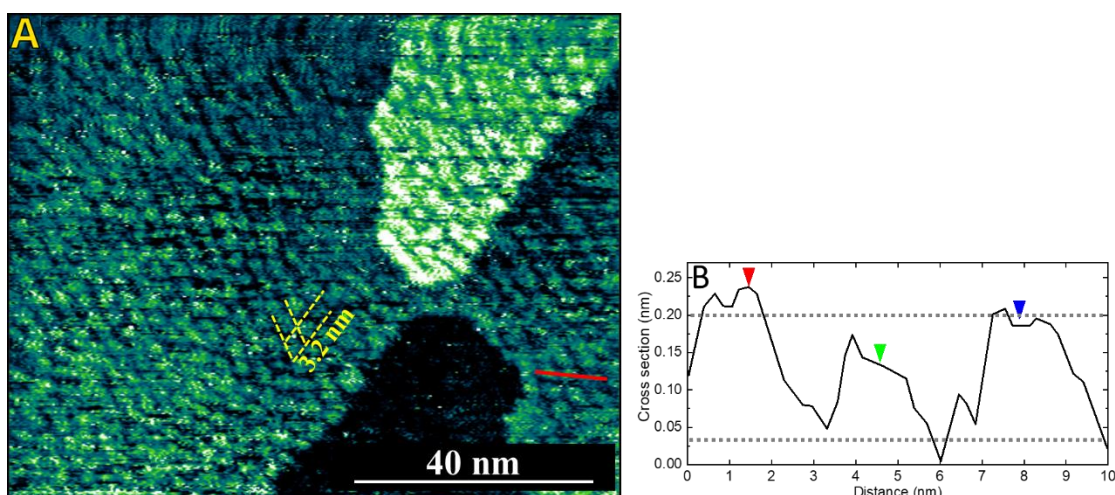
Figure 4.26. EC-STM image of h-BN/Rh(111) nanomesh in 0.1 M HClO$_4$ following tungsten oxide deposition measured with molybdenum tip (I_t = 1.5 nA, V_b = +0.45 V, E_{sub} = -0.0 V vs Pt). (B) Cross-sectional profile along the red line in (A), the arrows are spaced by 3.2 (±0.1) nm.

Ultimately, we attempted to image the surface using molybdenum tips under a negative bias voltage (potential difference between the tip and the substrate) to investigate possible effect on the cluster oxides. It is expected that at positive substrate bias, electrons tunnel from the tip into the substrate, and image temporarily populated empty molecular orbitals (i.e., the LUMO). *Vice versa*, at negative substrate bias, electrons tunnel from the substrate to the tip, and the HOMO is imaged. However, the conditions contributed to increase the tip instability, resulting in very noisy images. Additionally, double-tip artefacts were often visible, making futile any post-processing. Despite the low resolution and the noise, Figure 4.27 shows some pores are occupied by clusters that appear brighter than others, suggesting the possibility of distinguishing between the two species.

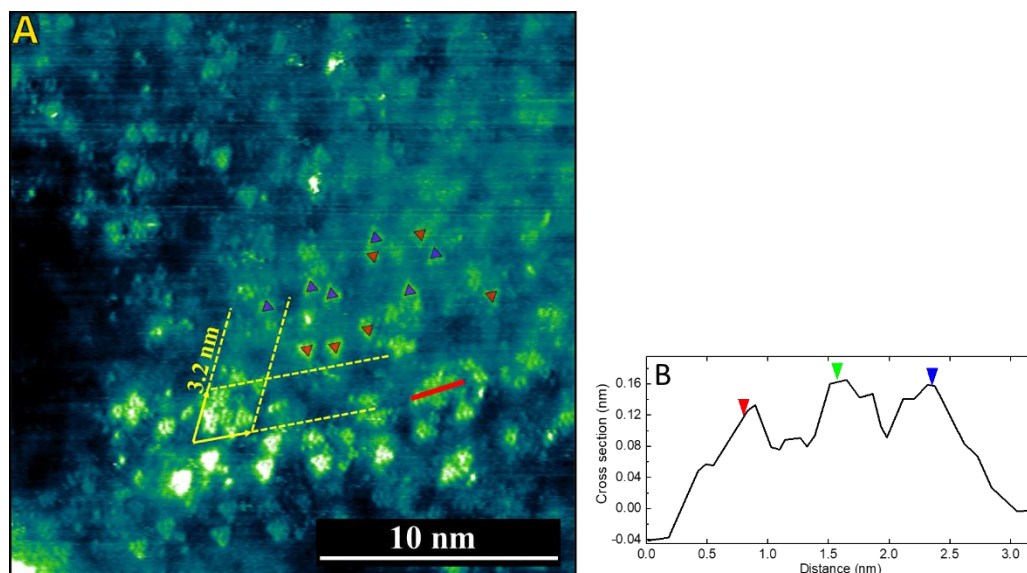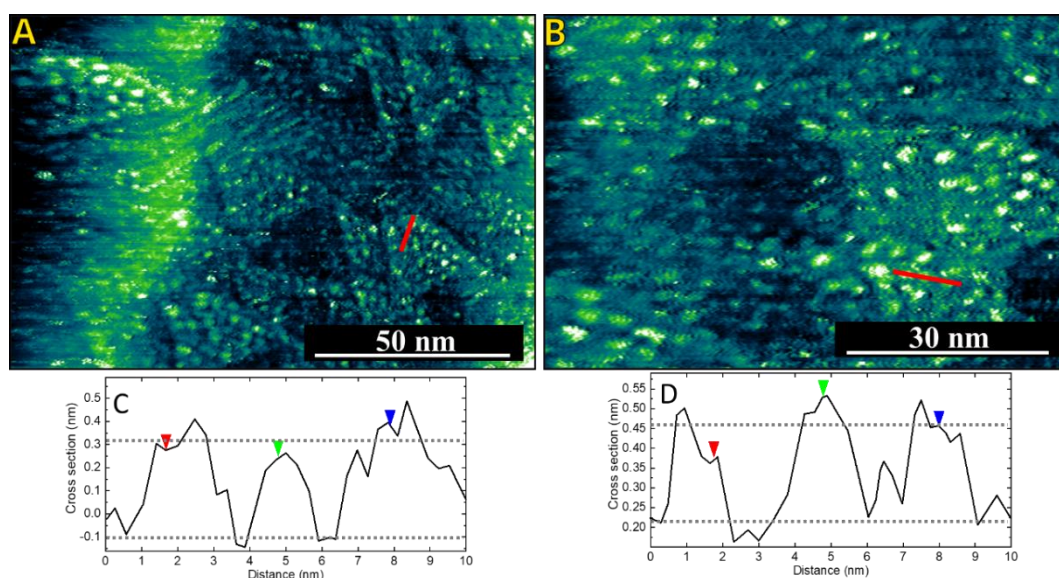Figure 4.27 EC-STM images of h-BN/Rh(111) nanomesh in 0.1 M $HClO_4$ following W oxide deposition measured with Mo tip (I_t = 1.0 nA, V_b = -0.15 V, E_{sub} = -0.65 V vs Pt). (C and D) Cross-sectional profile along the red lines in (A and B), the arrows are spaced by 3.2 ($\pm$0.1) nm.

In summary, in this chapter we first presented the improvements necessary to remove external noise from the STM, enabling atomic resolution necessary to investigate the oxide cluster deposited on the hBN nanomesh. We effectively used for the first time the molybdenum as a probe for ECSTM imaging. Despite the instability of both tungsten and molybdenum tips that prevented reporting the evolution of the oxide cluster, we imaged with sufficient lateral resolution their deposition on the nanomesh pores. Lastly, we attempted to distinguish the electronic structure by using a combination of the two oxide clusters alternatively deposited and imaged with tungsten and molybdenum tips.

5 Conclusions and outlook

In this thesis, we investigated the formation under electrochemical conditions of early transition metal oxide clusters. For the first time, molybdenum tips were used for EC-STM imaging. The tungsten and molybdenum oxides were characterised with non-electrochemical techniques. The unique properties of the boron nitride nanomesh allowed to image the monodispersed oxide cluster with EC-STM generated *in situ*.

In chapter 2 we employed electrochemical methods to study the behaviour of tungsten and molybdenum in aqueous solution. The stability of the metals was investigated using cyclic voltammetry in a range of pH (acidic to alkaline) and in several electrolytes to establish conditions for their passivation. While tungsten is easily passivated also at very low pH values, the molybdenum always favoured rapid transpassive oxidation for small potential increment. The rate of dissolution of the tungsten oxide was estimated from the charge used during the passivation cycle as 0.51 nm per minute (on average), corresponding to a WO_3 generation rate of 1.52 nmol min^{-1} cm^{-2}. Electrochemical impedance spectroscopy allowed to describe the process occurring on the surface of the metals.

In chapter 3 we characterised the metal oxide clusters with non-electrochemical techniques. ICP-OES allowed to evaluate semi-quantitatively both metal oxides generated in solution, however the ionisation used (ESI) for the mass spectrometry was unsuitable for the oxide metals which were undetected both in acidic and alkaline environments. Additionally, the metal oxide cluster deposited on the boron nitride nanomesh were investigated with spectroscopic techniques. With XPS we confirmed the presence of the metal oxide on the surface. Conversely, the low density of clusters on the surface did not allow detection with Raman spectroscopy, also limited by fluorescence of the sample.

In chapter 4 we optimised the EC-STM allowing to reach atomic resolution at room temperature. The new hardware configuration allowed to considerably reduce external vibrations which were affecting the measurements, so that atomic resolution of highly oriented pyrolytic graphite and of an iodine monolayer on Au(111) could routinely be

obtained. We successfully imaged the boron nitride nanomesh surface decorated with tungsten and molybdenum oxides. The stability of the nanomesh allowed to obtain images of the clusters in both positive and negative voltage bias. We report for the first time the use of the molybdenum as EC-STM probe, reaching a resolution comparable to the classically adopted tungsten. Finally, the metal oxide clusters were imaged using the dissimilar metal tips (imaging W with Mo and *vice versa*).

By taking advantage of the insulating property of the hBN nanomesh and its stability in aqueous electrolytes, further work could focus on EC-STM investigation of the metal oxide clusters to better understand molecular and interfacial phenomena, investigating catalytic reactions, charge transport and exchange through the interface.[164, 165, 166] The combination of the electrochemical control and high-resolution of the EC-STM may allow the *in situ* study of suitable reactions catalysed with the metal oxides, giving the possibility to observe intermediates with submolecular resolution during the transformation of the reagents to products,[167, 168, 169] as early metal oxides have been used as (co-)catalysts for alcohol reactions, in particular for the conversion of methanol to (or from) any intermediate product (i.e. formaldehyde, formic acid) up to carbon dioxide and *vice versa*.[57, 170] The investigation of multi-step reactions, such as the alcohol oxidation, may be the preferable as, in principle, any intermediate product could be detected increasing the chances of identifiable species in the system during *in operando* measurement.[171, 172, 173]

Additional spectroscopic techniques to provide chemical information regarding the oxide generation may be very useful. Once the restrictions associated with the detection limit are overcome, Raman spectroscopy can prove to be an excellent technique for *in situ* (or even *in operando*) monitoring of the metal oxide clusters formation and deposition on the nanomesh. The technique could be easily implemented and adapted for studying the evolution of catalysed reactions (i.e. methanol oxidation), integrating EC-STM investigations.[120, 174, 175] Finally, the combination of techniques may provide access to more detailed information. In particular, tip-enhanced Raman spectroscopy would be advantageous for surface characterisation and the investigation of electrochemical processes as it simultaneously provides detailed chemical and topographic information, with a spatial resolution and sensitivity that can reach single-molecule level.[176, 177, 178]

6 References

1. Negahdar L., Parlett C.M.A., Isaacs M.A., Beale A.M., Wilson K., Lee A.F. Shining light on the solid–liquid interface: in situ/operando monitoring of surface catalysis. *Catalysis Science & Technology* 2020, **10**(16)**:** 5362-5385.

2. Xie L., Huang C.Q., Liang Z.F., Wang H.B., Jiang Z., Song F. In-Situ HP-STM and Operando EC-STM Studies of Heterogeneous Catalysis at Interfaces. *Chinese Journal of Structural Chemistry* 2022, **41**(10)**:** 2210029-2210044.

3. Zaera F. Probing liquid/solid interfaces at the molecular level. *Chemical Reviews* 2012, **112**(5)**:** 2920-2986.

4. Weaver M.J., Gao X. In-Situ Electrochemical Surface Science. *Annual Review of Physical Chemistry* 1993, **44:** 459-494.

5. Kolb D.M. Electrochemical Surface Science. *Angewandte Chemie International Edition* 2001, **40**(7)**:** 1162-1181.

6. Kolb D.M. Electrochemical surface science: past, present and future. *Journal of Solid State Electrochemistry* 2011, **15**(7-8)**:** 1391-1399.

7. Gao X. In-Situ Characterization of Electrode-Solution Interfacial Processes by Atomic-Resolution Scanning Tunneling. PhD thesis, University Microfilms International, USA, 1992.

8. Gao X., Weaver M.J. Probing redox-induced molecular transformations by atomic-resolution scanning tunneling microscopy: iodide adsorption and electrooxidation on gold(111) in aqueous solution. *Journal of the American Chemical Society* 1992, **114**(22)**:** 8544-8551.

9. Soriaga M.P., Baricuatro J.H., Cummins K.D., Kim Y.G., Saadi F.H., Sun G.F., Mccrory C.C.L., Mckone J.R., Velazquez J.M., Ferrer I.M., Carim A.I., Javier A., Chmielowiec B., Lacy D.C., Gregoire J.M., Sanabria-Chinchilla J., Amashukeli X., Royea W.J., Brunschwig B.S., Hemminger J.C., Lewis N.S., Stickney J.L. Electrochemical surface science twenty years later: Expeditions into the electrocatalysis of reactions at the core of artificial photosynthesis. *Surface Science* 2015, **631:** 285-294.

10. Alonso-Vante N., Granozzi G. Electrochemical Surface Science: Basics and Applications. *Surfaces* 2019, **2**(3)**:** 455-457.

11. Zaera F. Surface chemistry at the liquid/solid interface. *Surface Science* 2011, **605**(13-14)**:** 1141-1145.

12. Lin S., Chen X., Wang Z.L. Contact Electrification at the Liquid-Solid Interface. *Chemical Reviews* 2022, **122**(5)**:** 5209-5232.

13. Binning G., Rohrer H., Gerber C., Weibel E. Surface Studies by Scanning Tunneling Microscopy. *Physical Review Letters* 1982, **49**(1)**:** 57-61.

14. Varga P., Schmid M. Chemical discrimination on atomic level by STM. *Applied Surface Science* 1999, **141**(3-4)**:** 287-293.

15.   Lustenberger P., Rohrer H., Christoph R., Siegenthaler H. Scanning tunneling microscopy at potential controlled electrode surfaces in electrolytic environment. *Journal of Electroanalytical Chemistry* 1988, **243**(1)**:** 225-235.

16.   Gentz K., Wandelt K. Electrochemical scanning tunneling microscopy. *Chimia* 2012, **66**(1-2)**:** 44-51.

17.   Cui K., Dorner I., Mertens S.F.L. Interfacial supramolecular electrochemistry. *Current Opinion in Electrochemistry* 2018, **8:** 156-163.

18.   Elliott M. High-resolution electrochemical STM of redox metalloproteins. *Current Opinion in Electrochemistry* 2017, **4**(1)**:** 152-158.

19.   Mertens S.F. Adsorption and Self-Organization of Organic Molecules under Electrochemical Control. In: Wandelt K (I ed). *Encyclopedia of Interfacial Chemistry: Surface Science and Electrochemistry*, vol. 4.1. Elsevier: Netherlands, 2018, pp 13-23. 978-0-12-809894-3.

20.   Cui K., Mali K.S., Ivasenko O., Wu D., Feng X., Walter M., Mullen K., De Feyter S., Mertens S.F. Squeezing, then stacking: from breathing pores to three-dimensional ionic self-assembly under electrochemical control. *Angewandte Chemie International Edition* 2014, **53**(47)**:** 12951-12954.

21.   Cui K., Mali K.S., Wu D., Feng X., Mullen K., Walter M., De Feyter S., Mertens S.F.L. Ambient Bistable Single Dipole Switching in a Molecular Monolayer. *Angewandte Chemie International Edition* 2020, **59**(33)**:** 14049-14053.

22.   Tao N.J. Probing potential-tuned resonant tunneling through redox molecules with scanning tunneling microscopy. *Physical Review Letters* 1996, **76**(21)**:** 4066-4069.

23.   He Y., Borguet E. Dynamics of porphyrin electron-transfer reactions at the electrode-electrolyte interface at the molecular level. *Angewandte Chemie International Edition* 2007, **46**(32)**:** 6098-6101.

24.   Den Boer D., Li M., Habets T., Iavicoli P., Rowan A.E., Nolte R.J., Speller S., Amabilino D.B., De Feyter S., Elemans J.A. Detection of different oxidation states of individual manganese porphyrins during their reaction with oxygen at a solid/liquid interface. *Nature Chemistry* 2013, **5**(7)**:** 621-627.

25.   Faisal F., Stumm C., Bertram M., Waidhas F., Lykhach Y., Cherevko S., Xiang F., Ammon M., Vorokhta M., Smid B., Skala T., Tsud N., Neitzel A., Beranova K., Prince K.C., Geiger S., Kasian O., Wahler T., Schuster R., Schneider M.A., Matolin V., Mayrhofer K.J.J., Brummel O., Libuda J. Electrifying model catalysts for understanding electrocatalytic reactions in liquid electrolytes. *Nature Materials* 2018, **17**(7)**:** 592-598.

26.   Pumera M. Graphene-based nanomaterials and their electrochemistry. *Chemical Society Reviews* 2010, **39**(11)**:** 4146-4157.

27.   Morozan A., Jaouen F. Metal organic frameworks for electrochemical applications. *Energy & Environmental Science* 2012, **5**(11)**:** 9269-9290.

28.   Geim A.K., Grigorieva I.V. Van der Waals heterostructures. *Nature* 2013, **499**(7459)**:** 419-425.

29. Phan T.H., Van Gorp H., Li Z., Trung Huynh T.M., Fujita Y., Verstraete L., Eyley S., Thielemans W., Uji I.H., Hirsch B.E., Mertens S.F.L., Greenwood J., Ivasenko O., De Feyter S. Graphite and Graphene Fairy Circles: A Bottom-Up Approach for the Formation of Nanocorrals. *ACS Nano* 2019, **13**(5)**:** 5559-5571.

30. Auwärter W. Hexagonal boron nitride monolayers on metal supports: Versatile templates for atoms, molecules and nanostructures. *Surface Science Reports* 2019, **74**(1)**:** 1-95.

31. Kumar A., Xu Q. Two-Dimensional Layered Materials as Catalyst Supports. *ChemNanoMat* 2018, **4**(1)**:** 28-40.

32. Nath N.C.D., Debnath T., Nurunnabi M., Kim E.-K. In Vitro Toxicity of 2D Materials. *Biomedical Applications of Graphene and 2D Nanomaterials*. Elsevier: Netherlands, 2019, pp 165-186. 978-0128158890.

33. Fan F.R., Bard A.J. STM on wet insulators: electrochemistry or tunneling? *Science* 1995, **270**(5243)**:** 1849-1852.

34. Kuznetsov A.M., Ulstrup J. Theory of electron transfer at electrified interfaces. *Electrochimica Acta* 2000, **45**(15-16)**:** 2339-2361.

35. Greber T., Corso M., Osterwalder J. Fermi surfaces of single layer dielectrics on transition metals. *Surface Science* 2009, **603**(10-12)**:** 1373-1377.

36. Uosaki K., Elumalai G., Dinh H.C., Lyalin A., Taketsugu T., Noguchi H. Highly Efficient Electrochemical Hydrogen Evolution Reaction at Insulating Boron Nitride Nanosheet on Inert Gold Substrate. *Scientific Reports* 2016, **6:** 32217.

37. Corso M., Auwärter W., Muntwiler M., Tamai A., Greber T., Osterwalder J. Boron nitride nanomesh. *Science* 2004, **303**(5655)**:** 217-220.

38. Berner S., Corso M., Widmer R., Groening O., Laskowski R., Blaha P., Schwarz K., Goriachko A., Over H., Gsell S., Schreck M., Sachdev H., Greber T., Osterwalder J. Boron nitride nanomesh: functionality from a corrugated monolayer. *Angewandte Chemie International Edition* 2007, **46**(27)**:** 5115-5119.

39. Dil H., Lobo-Checa J., Laskowski R., Blaha P., Berner S., Osterwalder J., Greber T. Surface trapping of atoms and molecules with dipole rings. *Science* 2008, **319**(5871)**:** 1824-1826.

40. Iannuzzi M., Tran F., Widmer R., Dienel T., Radican K., Ding Y., Hutter J., Groning O. Site-selective adsorption of phthalocyanine on h-BN/Rh(111) nanomesh. *Physical Chemistry Chemical Physics* 2014, **16**(24)**:** 12374-12384.

41. Fu Q., Bao X. Surface chemistry and catalysis confined under two-dimensional materials. *Chemical Society Reviews* 2017, **46**(7)**:** 1842-1874.

42. Mehler A., Neel N., Kroger J. Probing site-dependent decoupling of hexagonal boron nitride with molecular frontier orbitals. *Journal of Vacuum Science & Technology A* 2019, **37**(6)**:** 61404.

43. Widmer R., Berner S., Groning O., Brugger T., Osterwalder J., Greber T. Electrolytic in situ STM investigation of h-BN-nanomesh. *Electrochemistry Communications* 2007, **9**(10)**:** 2484-2488.

44. Mertens S.F.L. Copper underpotential deposition on boron nitride nanomesh. *Electrochimica Acta* 2017, **246:** 730-736.

45. Mohn F., Schuler B., Gross L., Meyer G. Different tips for high-resolution atomic force microscopy and scanning tunneling microscopy of single molecules. *Applied Physics Letters* 2013, **102**(7)**:** 073109.

46. Repp J., Meyer G., Stojkovic S.M., Gourdon A., Joachim C. Molecules on insulating films: scanning-tunneling microscopy imaging of individual molecular orbitals. *Physical Review Letters* 2005, **94**(2)**:** 026803.

47. Cun H., Seitsonen A.P., Roth S., Decurtins S., Liu S.-X., Osterwalder J., Greber T. An electron acceptor molecule in a nanomesh: F$_4$TCNQ on h-BN/Rh(111). *Surface Science* 2018, **678:** 183-188.

48. Mertens S.F., Hemmi A., Muff S., Groning O., De Feyter S., Osterwalder J., Greber T. Switching stiction and adhesion of a liquid on a solid. *Nature* 2016, **534**(7609)**:** 676-679.

49. Zemski K.A., Justes D.R., Castleman A.W. Studies of Metal Oxide Clusters: Elucidating Reactive Sites Responsible for the Activity of Transition Metal Oxide Catalysts. *Journal of Physical Chemistry B* 2002, **106**(24)**:** 6136-6148.

50. Gillaspie D.T., Tenent R.C., Dillon A.C. Metal-oxide films for electrochromic applications: present technology and future directions. *Journal of Materials Chemistry* 2010, **20**(43)**:** 9585-9592.

51. Kalantar-Zadeh K., Ou J.Z., Daeneke T., Mitchell A., Sasaki T., Fuhrer M.S. Two dimensional and layered transition metal oxides. *Applied Materials Today* 2016, **5:** 73-89.

52. Mardare C.C., Hassel A.W. Review on the Versatility of Tungsten Oxide Coatings. *Physica Status Solidi A* 2019, **216**(12)**:** 1900047.

53. Meyer J., Hamwi S., Kroger M., Kowalsky W., Riedl T., Kahn A. Transition metal oxides for organic electronics: energetics, device physics and applications. *Advanced Materials* 2012, **24**(40)**:** 5408-5427.

54. Asthagiri A., Dixon D.A., Dohnálek Z., Kay B.D., Rodriguez J.A., Rousseau R., Stacchiola D.J., Weaver J.F. Catalytic Chemistry on Oxide Nanostructures. *Oxide Materials at the Two-Dimensional Limit*. Springer: New York, 2016, pp 251-280. 978-3-319-28332-6.

55. Royer S., Duprez D. Catalytic Oxidation of Carbon Monoxide over Transition Metal Oxides. *ChemCatChem* 2011, **3**(1)**:** 24-65.

56. Yusuf A., Snape C., He J., Xu H., Liu C., Zhao M., Chen G.Z., Tang B., Wang C., Wang J., Behera S.N. Advances on transition metal oxides catalysts for formaldehyde oxidation: A review. *Catalysis Reviews* 2017, **59**(3)**:** 189-233.

57. Fang Z., Li Z., Kelley M.S., Kay B.D., Li S., Hennigan J.M., Rousseau R., Dohnálek Z., Dixon D.A. Oxidation, Reduction, and Condensation of Alcohols over (MO$_3$)$_3$ (M = Mo, W) Nanoclusters. *Journal of Physical Chemistry C* 2014, **118**(39)**:** 22620-22634.

58. Li Z., Fang Z., Kelley M.S., Kay B.D., Rousseau R., Dohnalek Z., Dixon D.A. Ethanol Conversion on Cyclic $(MO_3)_3$ (M = Mo, W) Clusters. *Journal of Physical Chemistry C* 2014, **118**(9)**:** 4869-4877.

59. Tang X., Bumueller D., Lim A., Schneider J., Heiz U., Gantefor G., Fairbrother D.H., Bowen K.H. Catalytic Dehydration of 2-Propanol by Size-Selected (WO_3) and $(MoO_3)_n$ Metal Oxide Clusters. *Journal of Physical Chemistry C* 2014, **118**(50)**:** 29278-29286.

60. Huang X., Zhai H.J., Kiran B., Wang L.S. Observation of d-orbital aromaticity. *Angewandte Chemie International Edition* 2005, **44**(44)**:** 7251-7254.

61. Zubarev D.Y., Averkiev B.B., Zhai H.J., Wang L.S., Boldyrev A.I. Aromaticity and antiaromaticity in transition-metal systems. *Physical Chemistry Chemical Physics* 2008, **10**(2)**:** 257-267.

62. Mercero J.M., Boldyrev A.I., Merino G., Ugalde J.M. Recent developments and future prospects of all-metal aromatic compounds. *Chemical Society Reviews* 2015, **44**(18)**:** 6519-6534.

63. Boldyrev A.I., Wang L.S. Beyond organic chemistry: aromaticity in atomic clusters. *Physical Chemistry Chemical Physics* 2016, **18**(17)**:** 11589.

64. Mullner M., Balajka J., Schmid M., Diebold U., Mertens S.F.L. Self-Limiting Adsorption of WO_3 Oligomers on Oxide Substrates in Solution. *Journal of Physical Chemistry C* 2017, **121**(36)**:** 19743-19750.

65. Wilms M., Kruft M., Bermes G., Wandelt K. A new and sophisticated electrochemical scanning tunneling microscope design for the investigation of potentiodynamic processes. *Review of Scientific Instruments* 1999, **70**(9)**:** 3641-3650.

66. Carrozzo P., Tumino F., Facibeni A., Passoni M., Casari C.S., Li Bassi A. Note: Fabrication and characterization of molybdenum tips for scanning tunneling microscopy and spectroscopy. *Review of Scientific Instruments* 2015, **86**(1)**:** 016112.

67. Goto Y., Suizu R., Noguchi Y., Yamada T.K. Oxidative vaporization etching for molybdenum tip formation in air. *Applied Surface Science* 2021, **542:** 148642.

68. Girault H.H. *Analytical and physical electrochemistry*. EPFL Press: Switzerland, 2004. 978-2940222032.

69. Dorner I. Electrochemical Surface Investigations of TiO_2 Rutile(110). MSc thesis, TU Wien, Wien, 2016.

70. Compton R.G., Banks C.E. *Understanding voltammetry*, 3rd edn. World Scientific: United Kingdom, 2018. 978-1786345295.

71. Rueda M.R., Dapena F.P. Application of Electrochemical Impedance Spectroscopy to the Study of Surface Processes. *Collection of Czechoslovak Chemical Communications* 2011, **76**(12)**:** 1825-1854.

72. Orazem M.E., Tribollet B. A tutorial on electrochemical impedance spectroscopy. *ChemTexts* 2020, **6**(2)**:** 6-12.

73. Wang S., Zhang J., Gharbi O., Vivier V., Gao M., Orazem M.E. Electrochemical impedance spectroscopy. *Nature Reviews Methods Primers* 2021, **1**(1)**:** 1-41.

74. Orazem M.E., Tribollet B. *Electrochemical Impedance Spectroscopy*. Wiley: New Jersey, 2008. 978-0470041406.

75. Lasia A. *Electrochemical Impedance Spectroscopy and its Applications*. Springer: New York, 2014. 978-1-4614-8932-0.

76. Pourbaix M. *Atlas of Electrochemical Equilibria in Aqueous Solution*. Cebelcor: Belgium, 1996. 978-0915567980.

77. Johnson J.W., Wu C.L. The Anodic Dissolution of Tungsten. *Journal of The Electrochemical Society* 1971, **118**(12)**:** 1909.

78. Anik M., Cansizoglu T. Dissolution kinetics of WO_3 in acidic solutions. *Journal of Applied Electrochemistry* 2006, **36**(5)**:** 603-608.

79. Lillard R.S., Kanner G.S., Butt D.P. The Nature of Oxide Films on Tungsten in Acidic and Alkaline Solutions. *Journal of The Electrochemical Society* 2019, **145**(8)**:** 2718-2725.

80. El-Basiouny M.S., Hassan S.A., Hefny M.M. On the electrochemical behaviour of tungsten: the formation and dissolution of tungsten oxide in sulphuric acid solutions. *Corrosion Science* 1980, **20**(7)**:** 909-917.

81. Anik M. Effect of concentration gradient on the anodic behavior of tungsten. *Corrosion Science* 2006, **48**(12)**:** 4158-4173.

82. Anik M., Osseo-Asare K. Effect of pH on the anodic Behavior of tungsten. *Journal of The Electrochemical Society* 2002, **149**(6)**:** B224-B233.

83. Miu E.V., Mckone J.R., Mpourmpakis G. The Sensitivity of Metal Oxide Electrocatalysis to Bulk Hydrogen Intercalation: Hydrogen Evolution on Tungsten Oxide. *Journal of the American Chemical Society* 2022, **144**(14)**:** 6420-6433.

84. Haynes W.M., Lide D.R., Bruno T.J. *CRC Handbook of Chemistry and Physics*, 97th edn. CRC Press: Florida, 2016. 978-1315380476.

85. Vergé M.G., Olsson C.O.A., Landolt D. Anodic oxide growth on tungsten studied by EQCM, EIS and AES. *Corrosion Science* 2004, **46**(10)**:** 2583-2600.

86. Krebsz M., Kollender J.P., Hassel A.W. In situmonitoring of the electrochemical dissolution of tungsten. *Physica Status Solidi A* 2017, **214**(9)**:** 1600803.

87. Hsu C.H., Mansfeld F. Technical Note: Concerning the Conversion of the Constant Phase Element Parameter Y_0 into a Capacitance. *Corrosion* 2001, **57**(09)**:** 747-748.

88. Lazanas A.C., Prodromidis M.I. Electrochemical Impedance Spectroscopy-A Tutorial. *ACS Measurement Science* 2023, **3**(3)**:** 162-193.

89. Biaggio S.R., Rocha-Filho R.C., Vilche J.R., Varela F.E., Gassa L.M. A study of thin anodic WO_3 films by electrochemical impedance spectroscopy. *Electrochimica Acta* 1997, **42**(11)**:** 1751-1758.

90. Kelsey G.S. The Anodic Oxidation of Tungsten in Aqueous Base. *Journal of The Electrochemical Society* 2019, **124**(6)**:** 814-819.

91.   De Castro I.A., Datta R.S., Ou J.Z., Castellanos-Gomez A., Sriram S., Daeneke T., Kalantar-Zadeh K. Molybdenum Oxides - From Fundamentals to Functionality. *Advanced Materials* 2017, **29**(40)**:** 1701619.

92.   Seguin L., Figlarz M., Cavagnat R., Lassègues J.C. Infrared and Raman spectra of MoO_3 molybdenum trioxides and $MoO_3 \cdot xH_2O$ molybdenum trioxide hydrates. *Spectrochimica Acta Part A* 1995, **51**(8)**:** 1323-1344.

93.   Saji V.S., Lee C.W. Molybdenum, molybdenum oxides, and their electrochemistry. *ChemSusChem* 2012, **5**(7)**:** 1146-1161.

94.   Lu Y.C., Clayton C.R. An XPS study of the passive and transpassive behavior of molybdenum in deaerated 0.1 M HCl. *Corrosion Science* 1989, **29**(8)**:** 927-937.

95.   Johnson J.W., Chi C.H., Chen C.K., James W.J. The Anodic Dissolution of Molybdenum. *Corrosion* 1970, **26**(8)**:** 338-342.

96.   Pozdeeva A.A., Antonovskaya E.I., Sukhotin A.M. Passivity of molybdenum. *Corrosion Science* 1966, **6**(3-4)**:** 149-158.

97.   Nölte J. *ICP Emission Spectrometry*. Wiley: New Jersey, 2021. 978-3527346578.

98.   Thomas R. *Practical Guide to ICP-MS*, III edn. CRC Press: Florida, 2013. 1466555432.

99.   Smith R.W. Mass Spectrometry. *Encyclopedia of Forensic Sciences*. Elsevier: Netherlands, 2013, pp 603-608. 978-0123821669.

100.   Hofmann S. *Auger- and X-Ray Photoelectron Spectroscopy in Materials Science*. Springer: New York, 2013. 978-3642273803.

101.   Woicik J. *Hard X-ray Photoelectron Spectroscopy (HAXPES)*. Springer: New York, 2016. 978-3-319-24041-1.

102.   Wagner J.M. *X-ray photoelectron spectroscopy*. Nova: New York, 2011. 978-1617282409.

103.   Van Der Heide P. *X-Ray Photoelectron Spectroscopy*. Wiley: New Jersey, 2011. 978-1118062531.

104.   Toporski J., Dieing T., Hollricher O. *Confocal Raman Microscopy*. Springer: New York, 2018. 978-3642125218.

105.   Gervasio A.P.G., Luca G.C., Menegário A.A., Reis B.F., Filho H.B. On-line electrolytic dissolution of alloys in flow injection analysis. *Analytica Chimica Acta* 2000, **405**(1-2)**:** 213-219.

106.   Johnson G.E., Tyo E.C., Castleman A.W., Jr. Cluster reactivity experiments: employing mass spectrometry to investigate the molecular level details of catalytic oxidation reactions. *Proceedings of the National Academy of Sciences* 2008, **105**(47)**:** 18108-18113.

107.   Ausekar M.V., Mawale R.M., Pazdera P., Havel J. Matrix Assisted and/or Laser Desorption Ionization Quadrupole Ion Trap Time-of-Flight Mass Spectrometry of WO_3

Clusters Formation in Gas Phase. Nanodiamonds, Fullerene, and Graphene Oxide Matrices. *Journal of the American Society for Mass Spectrometry* 2018, **29**(3)**:** 581-587.

108. Banerjee S., Mazumdar S. Electrospray ionization mass spectrometry: a technique to access the information beyond the molecular weight of the analyte. *International Journal of Analytical Chemistry* 2012, **2012:** 282574.

109. Konermann L., Ahadi E., Rodriguez A.D., Vahidi S. Unraveling the mechanism of electrospray ionization. *Analytical Chemistry* 2013, **85**(1)**:** 2-9.

110. Hemmi A., Bernard C., Cun H., Roth S., Klockner M., Kalin T., Weinl M., Gsell S., Schreck M., Osterwalder J., Greber T. High quality single atomic layer deposition of hexagonal boron nitride on single crystalline Rh(111) four-inch wafers. *Review of Scientific Instruments* 2014, **85**(3)**:** 035101.

111. Castle J.E., Baker M.A. The feasibility of an XPS expert system demonstrated by a rule set for carbon contamination. *Journal of Electron Spectroscopy and Related Phenomena* 1999, **105**(2-3)**:** 245-256.

112. Walton J., Alexander M.R., Fairley N., Roach P., Shard A.G. Film thickness measurement and contamination layer correction for quantitative XPS. *Surface and Interface Analysis* 2016, **48**(3)**:** 164-172.

113. Khyzhun O.Y. XPS, XES and XAS studies of the electronic structure of tungsten oxides. *Journal of Alloys and Compounds* 2000, **305**(1-2)**:** 1-6.

114. Manciu F.S., Enriquez J.L., Durrer W.G., Yun Y., Ramana C.V., Gullapalli S.K. Spectroscopic analysis of tungsten oxide thin films. *Journal of Materials Research* 2011, **25**(12)**:** 2401-2406.

115. Werfel F., Minni E. Photoemission study of the electronic structure of Mo and Mo oxides. *Journal of Physics C* 1983, **16**(31)**:** 6091-6100.

116. Koyun O., Gorduk S., Arvas M.B., Sahin Y. Direct, one-step synthesis of molybdenum blue using an electrochemical method, and characterization studies. *Synthetic Metals* 2017, **233:** 111-118.

117. Alov N.V. Determination of the States of Oxidation of Metals in Thin Oxide Films by X-Ray Photoelectron Spectroscopy. *Journal of Analytical Chemistry* 2005, **60**(5)**:** 431-435.

118. Daniel M.F., Desbat B., Lassegues J.C., Gerand B., Figlarz M. Infrared and Raman study of WO_3 tungsten trioxides and $WO_3 \cdot xH_2O$ tungsten trioxide tydrates. *Journal of Solid State Chemistry* 1987, **67**(2)**:** 235-247.

119. Garcia-Sanchez R.F., Ahmido T., Casimir D., Baliga S., Misra P. Thermal effects associated with the Raman spectroscopy of WO_3 gas-sensor materials. *Journal of Physical Chemistry A* 2013, **117**(50)**:** 13825-13831.

120. Mestl G., Ruiz P., Delmon B., Knozinger H. Oxygen-Exchange Properties of MoO_3: An in situ Raman Spectroscopy Study. *Journal of Physical Chemistry* 1994, **98**(44)**:** 11269-11275.

121. Kuzuba T., Era K., Ishii T., Sato T. A low frequency Raman-active vibration of hexagonal boron nitride. *Solid State Communications* 1978, **25**(11)**:** 863-865.

122. Cai Q., Scullion D., Falin A., Watanabe K., Taniguchi T., Chen Y., Santos E.J., Li L.H. Raman signature and phonon dispersion of atomically thin boron nitride. *Nanoscale* 2017, **9**(9)**:** 3059-3067.

123. Voigtländer B. *Scanning Probe Microscopy (Atomic Force Microscopy and Scanning Tunneling Microscopy).* Springer: New York, 2015. 978-3-662-45239-4.

124. Binnig G., Rohrer H., Gerber C., Weibel E. Tunneling through a controllable vacuum gap. *Applied Physics Letters* 1982, **40**(2)**:** 178-180.

125. Bian K., Gerber C., Heinrich A.J., Muller D.J., Scheuring S., Jiang Y. Scanning probe microscopy. *Nature Reviews Methods Primers* 2021, **1**(1)**:** 1-36.

126. Nowicki M., Wandelt K. Electrochemical Scanning Tunneling Microscopy. *Surface Science and Electrochemistry* 2018**:** 108-128.

127. Tersoff J., Hamann D.R. Theory of the scanning tunneling microscope. *Physical Review B* 1985, **31**(2)**:** 805-813.

128. Leavens C.R., Aers G.C. Tunneling current density within Tersoff and Hamann's theory of the scanning tunneling microscope. *Physical Review B* 1988, **38**(11)**:** 7357-7364.

129. Huang Z.H., Feuchtwang T.E., Cutler P.H., Kazes E. Wentzel-Kramers-Brillouin method in multidimensional tunneling. *Physical Review A* 1990, **41**(1)**:** 32-41.

130. Nanosurf easyScan 2 STM operating instruction. *Nanosurf AG*; 2011.

131. Ibe J.P., Bey P.P., Brandow S.L., Brizzolara R.A., Burnham N.A., Dilella D.P., Lee K.P., Marrian C.R.K., Colton R.J. On the Electrochemical Etching of Tips for Scanning Tunneling Microscopy. *Journal of Vacuum Science & Technology A* 1990, **8**(4)**:** 3570-3575.

132. Ju B.F., Chen Y.L., Ge Y. The art of electrochemical etching for preparing tungsten probes with controllable tip profile and characteristic parameters. *Review of Scientific Instruments* 2011, **82**(1)**:** 013707.

133. Lisowski W., Van Den Berg A.H.J., Hanekamp L.J., Van Silfhout A. Composition and thickness of surface layer on molybdenum tips for scanning tunnelling microscopy (STM) studied by SEM/AES/(AR)XPS. *Surface and Interface Analysis* 1992, **19**(1-12)**:** 93-99.

134. Hull M.N. On the anodic dissolution of molybdenum in acidic and alkaline electrolytes. *Journal of Electroanalytical Chemistry and Interfacial Electrochemistry* 1972, **38**(1)**:** 143-157.

135. Mitchell P.C.H., Outteridge T., Kloska K., Mcmahon S., Epshteyn Y., Sebenik R.F., Burkin A.R., Dorfler R.R., Laferty J.M., Leichtfried G., Meyer-Grünow H., Vukasovich M.S. Molybdenum and Molybdenum Compounds. *Ullmann's Encyclopedia of Industrial Chemistry*. Wiley: New Jersey, 2020, pp 1-63. 978-3527303854.

136. Schneider C.A., Rasband W.S., Eliceiri K.W. NIH Image to ImageJ: 25 years of image analysis. *Nature Methods* 2012, **9**(7)**:** 671-685.

137. Nečas D., Klapetek P. Gwyddion: an open-source software for SPM data analysis. *Central European Journal of Physics* 2012, **10**(1)**:** 181-188.

138.   Horcas I., Fernandez R., Gomez-Rodriguez J.M., Colchero J., Gomez-Herrero J., Baro A.M. WSXM: a software for scanning probe microscopy and a tool for nanotechnology. *Review of Scientific Instruments* 1988, **78**(1)**:** 1503.

139.   Dishner M.H., Ivey M.M., Gorer S., Hemminger J.C., Feher F.J. Preparation of gold thin films by epitaxial growth on mica and the effect of flame annealing. *Journal of Vacuum Science & Technology A* 1998, **16**(6)**:** 3295-3300.

140.   Nogues C., Wanunu M. A rapid approach to reproducible, atomically flat gold films on mica. *Surface Science* 2004, **573**(3)**:** 383-389.

141.   Iannuzzi M., Kalichava I., Ma H.F., Leake S.J., Zhou H.T., Li G., Zhang Y., Bunk O., Gao H.J., Hutter J., Willmott P.R., Greber T. Moire beatings in graphene on Ru(0001). *Physical Review B* 2013, **88**(12)**:** 125433.

142.   Bacle P., Seitsonen A.P., Iannuzzi M., Hutter J. Chemical Reactions on Metal-supported Hexagonal Boron Nitride Investigated with Density Functional Theory. *Chimia* 2014, **68**(9)**:** 596-601.

143.   Iannuzzi M. Ar Implantation at the hBN/Rh(111) Nanomesh by ab Initio Molecular Dynamics. *Journal of Physical Chemistry C* 2015, **119**(38)**:** 22198-22207.

144.   Rodríguez-Fortea A., Iannuzzi M., Parrinello M. Ab Initio Molecular Dynamics Study of Heterogeneous Nitric Acid Decomposition Reactions on Graphite Surfaces. *Journal of Physical Chemistry C* 2007, **111**(5)**:** 2251-2258.

145.   Dienel T., Gomez-Diaz J., Seitsonen A.P., Widmer R., Iannuzzi M., Radican K., Sachdev H., Mullen K., Hutter J., Groning O. Dehalogenation and coupling of a polycyclic hydrocarbon on an atomically thin insulator. *ACS Nano* 2014, **8**(7)**:** 6571-6579.

146.   Melani G., Guerrero-Felipe J.P., Valencia A.M., Krumland J., Cocchi C., Iannuzzi M. Donors, acceptors, and a bit of aromatics: electronic interactions of molecular adsorbates on hBN and MoS_2 monolayers. *Physical Chemistry Chemical Physics* 2022, **24**(27)**:** 16671-16679.

147.   Hutter J., Iannuzzi M., Schiffmann F., Vandevondele J. CP2K: atomistic simulations of condensed matter systems. *Wiley Interdisciplinary Reviews: Computational Molecular Science* 2014, **4**(1)**:** 15-25.

148.   Gómez Díaz J., Ding Y., Koitz R., Seitsonen A.P., Iannuzzi M., Hutter J. Hexagonal boron nitride on transition metal surfaces. *Theoretical Chemistry Accounts* 2013, **132**(4)**:** 1350.

149.   Ding Y., Iannuzzi M., Hutter J. Investigation of Boron Nitride Nanomesh Interacting with Water. *Journal of Physical Chemistry C* 2011, **115**(28)**:** 13685-13692.

150.   Musso T., Caravati S., Hutter J., Iannuzzi M. Second generation Car-Parrinello MD: application to the h-BN/Rh(111) nanomesh. *European Physical Journal B* 2018, **91**(7)**:** 148-157.

151.   Golze D., Hutter J., Iannuzzi M. Wetting of water on hexagonal boron nitride@Rh(111): a QM/MM model based on atomic charges derived for nano-structured substrates. *Physical Chemistry Chemical Physics* 2015, **17**(22)**:** 14307-14316.

152. Kuhne T.D., Iannuzzi M., Del Ben M., Rybkin V.V., Seewald P., Stein F., Laino T., Khaliullin R.Z., Schutt O., Schiffmann F., Golze D., Wilhelm J., Chulkov S., Bani-Hashemian M.H., Weber V., Borstnik U., Taillefumier M., Jakobovits A.S., Lazzaro A., Pabst H., Muller T., Schade R., Guidon M., Andermatt S., Holmberg N., Schenter G.K., Hehn A., Bussy A., Belleflamme F., Tabacchi G., Gloss A., Lass M., Bethune I., Mundy C.J., Plessl C., Watkins M., Vandevondele J., Krack M., Hutter J. CP2K: An electronic structure and molecular dynamics software package - Quickstep: Efficient and accurate electronic structure calculations. *Journal of Chemical Physics* 2020, **152**(19)**:** 194103.

153. Goedecker S., Teter M., Hutter J. Separable dual-space Gaussian pseudopotentials. *Physical Review B* 1996, **54**(3)**:** 1703-1710.

154. Perdew J.P., Burke K., Ernzerhof M. Generalized Gradient Approximation Made Simple. *Physical Review Letters* 1996, **77**(18)**:** 3865-3868.

155. Vandevondele J., Hutter J. Gaussian basis sets for accurate calculations on molecular systems in gas and condensed phases. *Journal of Chemical Physics* 2007, **127**(11)**:** 114105.

156. Vydrov O.A., Van Voorhis T. Nonlocal van der Waals density functional made simple. *Physical Review Letters* 2009, **103**(6)**:** 063004.

157. Mchardy R., Haiss W.H., Nichols R.J. An STM investigation of surface diffusion on iodine modified Au(111). *Physical Chemistry Chemical Physics* 2000, **2**(7)**:** 1439-1444.

158. Li S., Dixon D.A. Structural and Electronic Near Degeneracy of $M_3O_9^-$ (M = Cr, Mo, W). *Journal of Physical Chemistry C* 2011, **115**(39)**:** 19190-19196.

159. Zhu J., Jin H., Chen W., Li Y., Zhang Y., Ning L., Huang X., Ding K., Chen W. Structural and Electronic Properties of a W_3O_9 Cluster Supported on the TiO_2(110) Surface. *Journal of Physical Chemistry C* 2009, **113**(40)**:** 17509-17517.

160. Das T., Tosoni S., Pacchioni G. Structural and electronic properties of bulk and ultrathin layers of V_2O_5 and MoO_3. *Computational Materials Science* 2019, **163:** 230-240.

161. Li And S., Dixon D.A. Structural and Electronic Properties of Group 6 Transition Metal Oxide Clusters. *New and Future Developments in Catalysis*. Elsevier: Netherlands, 2013, pp 21-61. 978-0444538741.

162. Zhai H.J., Wang L.S. Probing the electronic structure of early transition metal oxide clusters: Molecular models towards mechanistic insights into oxide surfaces and catalysis. *Chemical Physics Letters* 2010, **500:** 185-195.

163. Momma K., Izumi F. VESTA 3 for three-dimensional visualization of crystal, volumetric and morphology data. *Journal of Applied Crystallography* 2011, **44**(6)**:** 1272-1276.

164. Molaei M.J., Younas M., Rezakazemi M. A Comprehensive Review on Recent Advances in Two-Dimensional (2D) Hexagonal Boron Nitride. *ACS Applied Electronic Materials* 2021, **3**(12)**:** 5165-5187.

165. Gross L. Recent advances in submolecular resolution with scanning probe microscopy. *Nature Chemistry* 2011, **3**(4)**:** 273-278.

166. Imai-Imada M., Imada H., Miwa K., Jung J., Shimizu T.K., Kawai M., Kim Y. Energy-level alignment of a single molecule on ultrathin insulating film. *Physical Review B* 2018, **98**(20)**:** 201403.

167. Liang Y., Pfisterer J.H.K., Mclaughlin D., Csoklich C., Seidl L., Bandarenka A.S., Schneider O. Electrochemical Scanning Probe Microscopies in Electrocatalysis. *Small Methods* 2019, **3**(8)**:** 1800387.

168. Feng H., Xun X., Du Y., Dou S.X. Application of Scanning Tunneling Microscopy in Electrocatalysis and Electrochemistry. *Electrochemical Energy Reviews* 2021, **4**(2)**:** 249-268.

169. Jin H., Guo C., Liu X., Liu J., Vasileff A., Jiao Y., Zheng Y., Qiao S.Z. Emerging Two-Dimensional Nanomaterials for Electrocatalysis. *Chemical Reviews* 2018, **118**(13)**:** 6337-6408.

170. Martínez S., Martins M.E., Zinola C.F. Surface metal modifiers for methanol electrooxidation on platinum, molybdenum and tungsten. *International Journal of Hydrogen Energy* 2010, **35**(11)**:** 5343-5355.

171. Védrine J.C., Fechete I. Heterogeneous partial oxidation catalysis on metal oxides. *Comptes Rendus Chimie* 2016, **19**(10)**:** 1203-1225.

172. Rousseau R., Dixon D.A., Kay B.D., Dohnalek Z. Dehydration, dehydrogenation, and condensation of alcohols on supported oxide catalysts based on cyclic $(WO_3)_3$ and $(MoO_3)_3$ clusters. *Chemical Society Reviews* 2014, **43**(22)**:** 7664-7680.

173. Choksi T., Greeley J. Partial Oxidation of Methanol on MoO_3 (010): A DFT and Microkinetic Study. *ACS Catalysis* 2016, **6**(11)**:** 7260-7277.

174. Hu H., Wachs I.E. Catalytic Properties of Supported Molybdenum Oxide Catalysts: In Situ Raman and Methanol Oxidation Studies. *Journal of Physical Chemistry* 1995, **99**(27)**:** 10911-10922.

175. Burcham L.J., Badlani M., Wachs I.E. The origin of the ligand effect in metal oxide catalysts: Novel fixed-bed in situ infrared and kinetic studies during methanol oxidation. *Journal of Catalysis* 2001, **203**(1)**:** 104-121.

176. Domke K.F., Pettinger B. In situ discrimination between axially complexed and ligand-free Co porphyrin on Au(111) with tip-enhanced Raman spectroscopy. *ChemPhysChem* 2009, **10**(11)**:** 1794-1798.

177. Kurouski D. Advances of tip-enhanced Raman spectroscopy (TERS) in electrochemistry, biochemistry, and surface science. *Vibrational Spectroscopy* 2017, **91:** 3-15.

178. Pfisterer J.H.K., Domke K.F. Unfolding the versatile potential of EC-TERS for electrocatalysis. *Current Opinion in Electrochemistry* 2018, **8:** 96-102.

7 Appendices

Appendix A – Electrochemical measurements
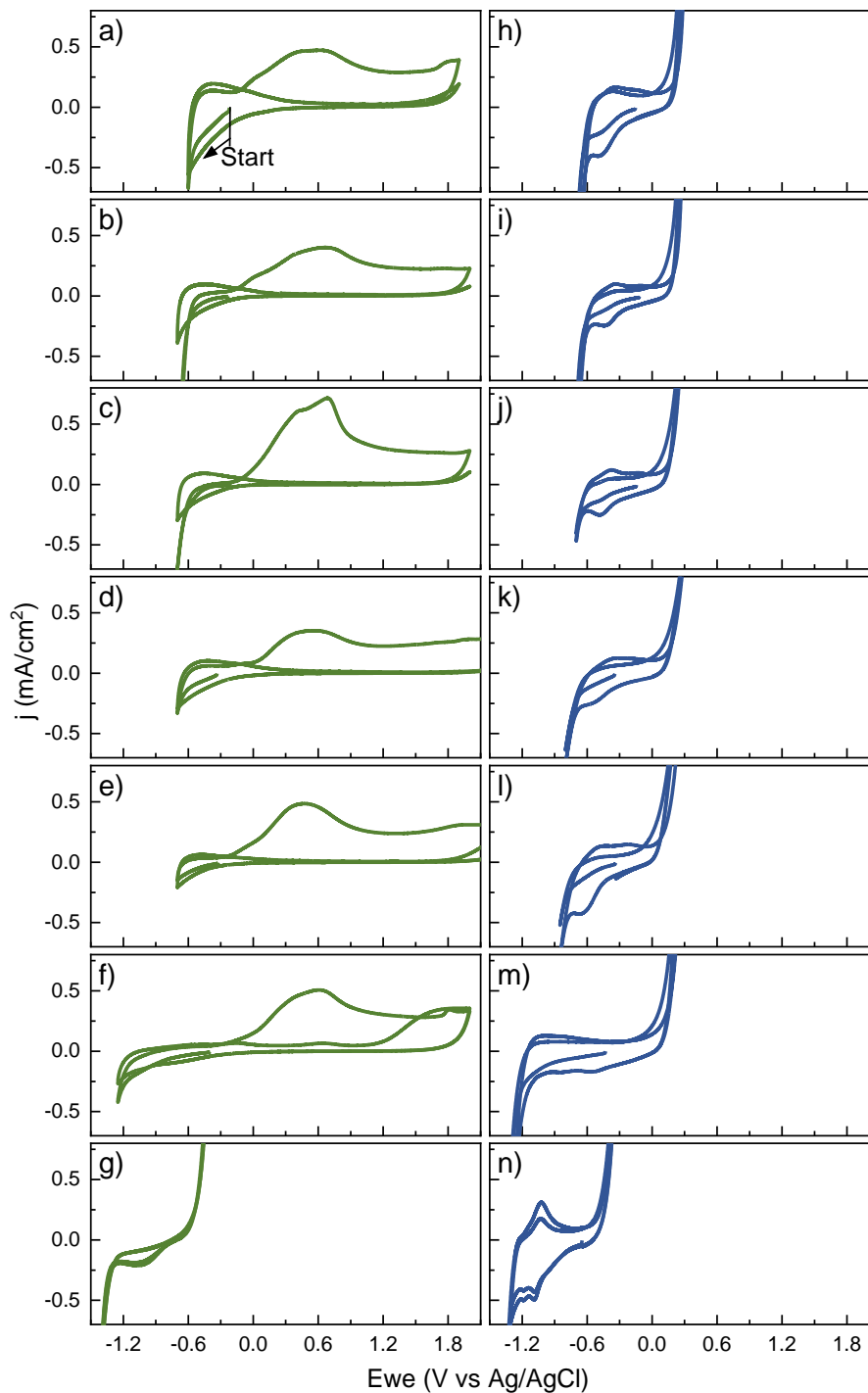
Cyclic voltammograms of polycrystalline tungsten (green) and molybdenum (blue) wires in (top to bottom) $HClO_4$ 0.1M, HCl 0.1M, H_2SO_4 0.05M, formic acid 0.1M (pH 2.5), formic acid buffer solution (pH 4.6) 0.1M, $NaClO_4$ 0.1M, NaOH 0.1M. Two cycles measured after equilibration for 15 minutes. Oxygen removed from the solution with argon.
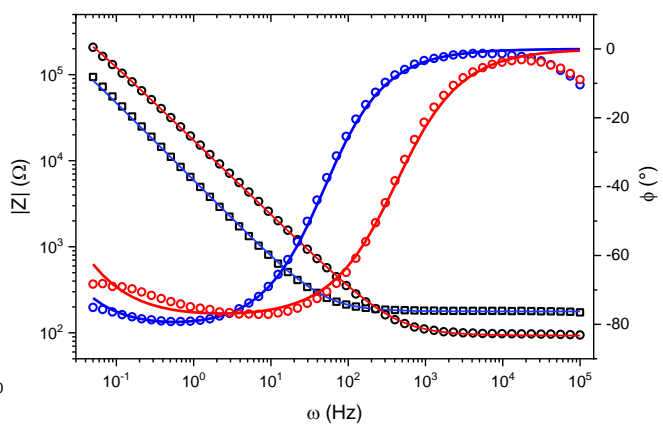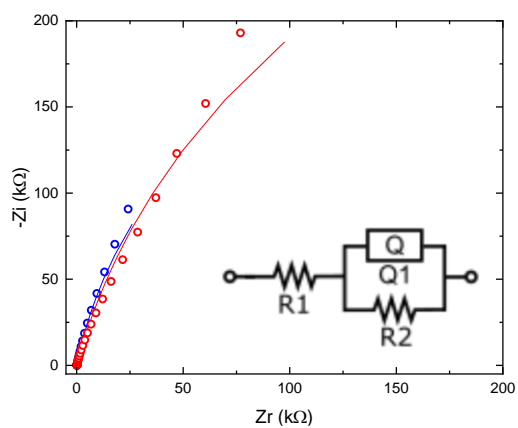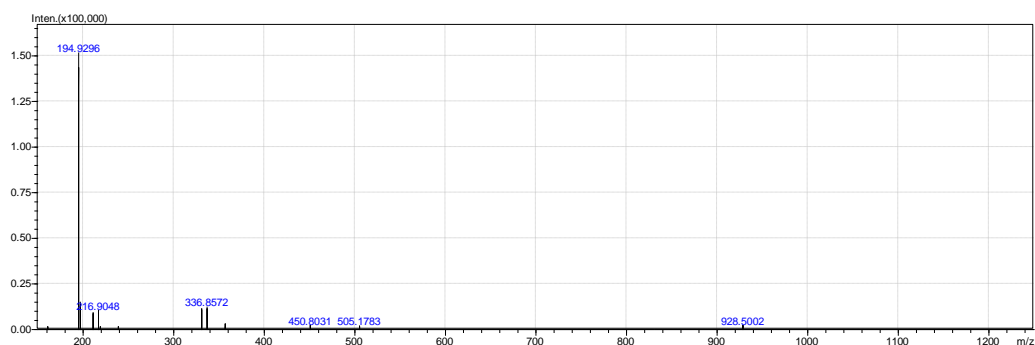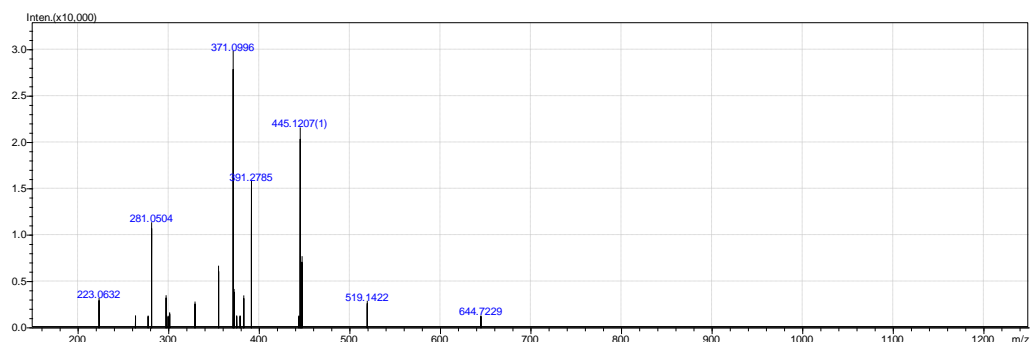
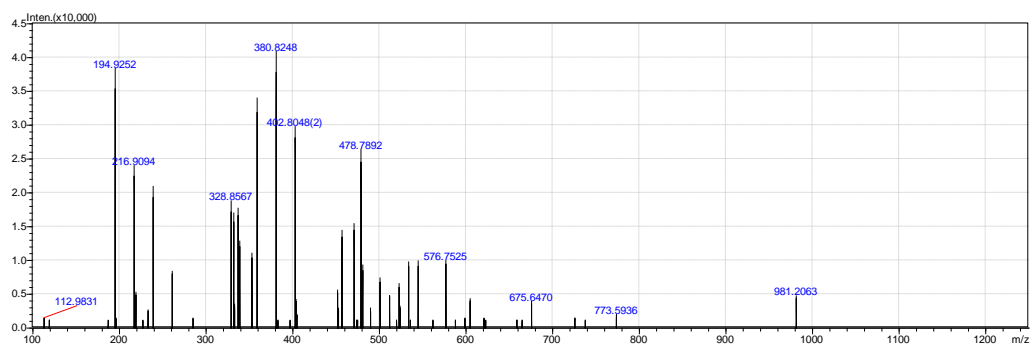EIS of tungsten in H₂SO₄ (blue) and FA buffer (red) measured at E = 0.0 V vs Ag/AgCl.
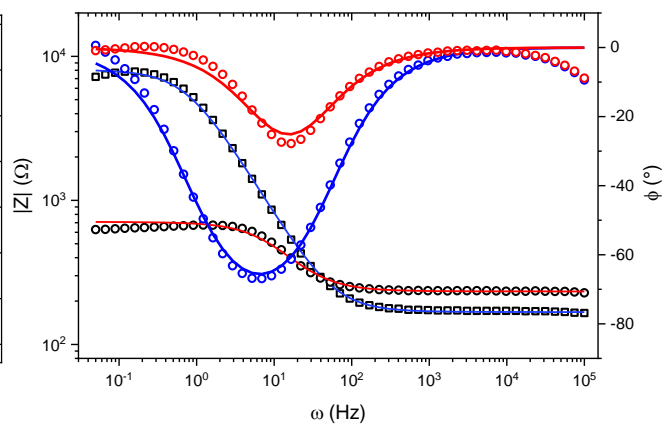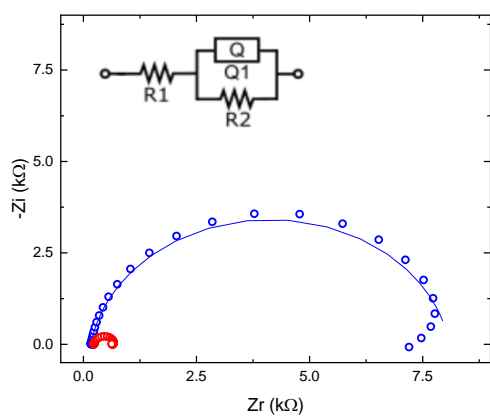
EIS of molybdenum in H₂SO₄ (blue) and FA buffer (red) measured at E = 0.0 V vs Ag/AgCl.

Appendix B – Mass spectrometry measurements

Positive (top) and negative (bottom) adducts from mass spectrometry of tungsten oxide powder in H_2SO_4 0.05 M (after NaOH neutralisation) (45 ppm)
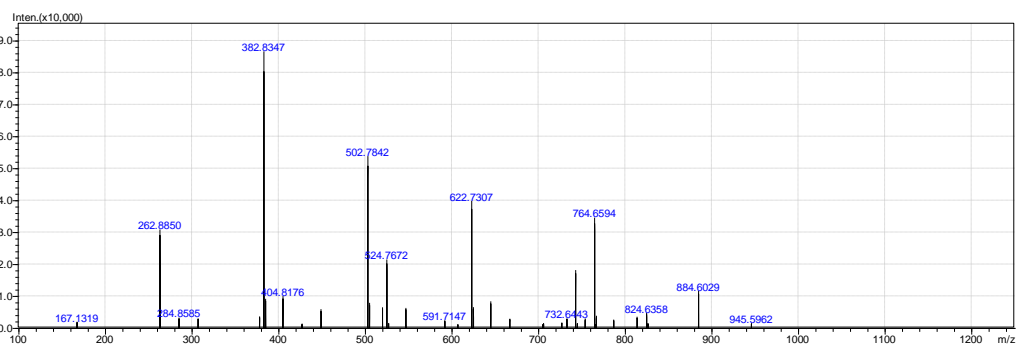
Positive (top) and negative (bottom) adducts from mass spectrometry of tungsten oxide powder in NaOH 0.1M (465 ppm)
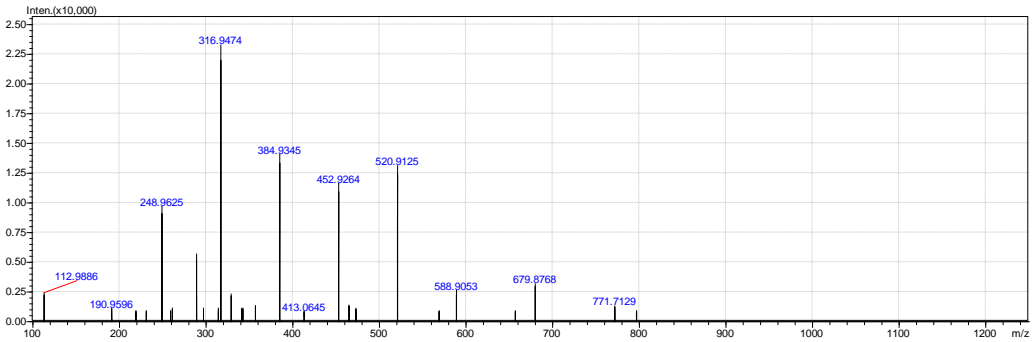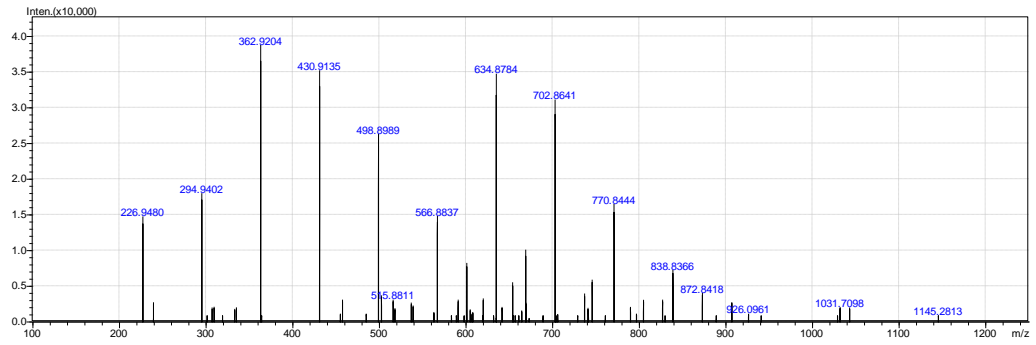
Positive (top) and negative (bottom) adducts from mass spectrometry of tungsten oxide powder in NaOH 0.1M (55 ppm)
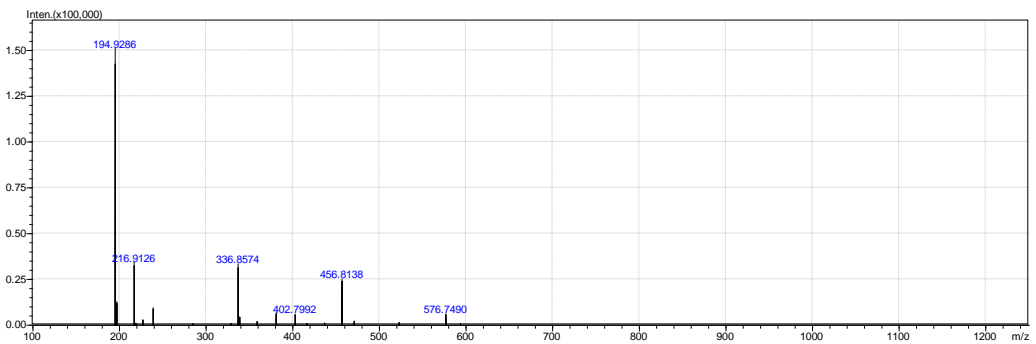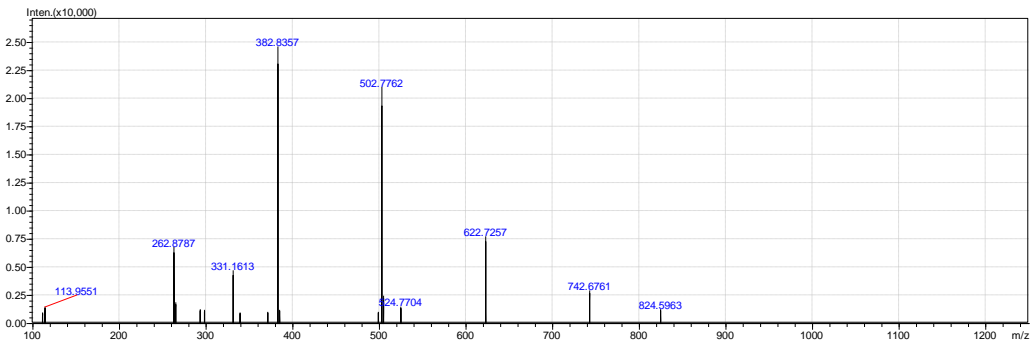
Positive (top) and negative (bottom) adducts from mass spectrometry of tungsten oxides generated electrochemically in H_2SO_4 0.05 M

# Appendix C – Raman measurements
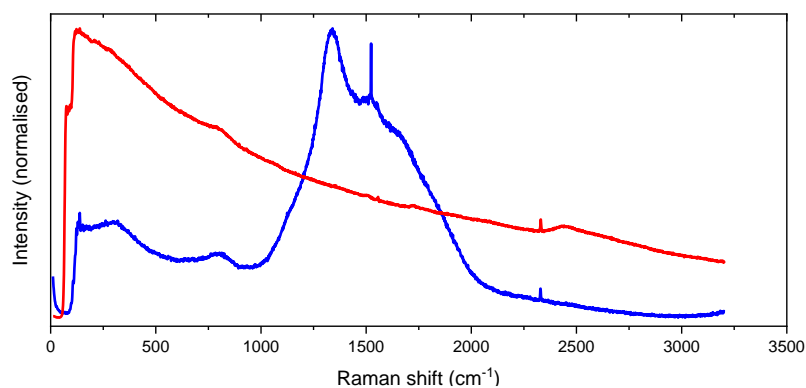
Fluorescence of bare Au(111) 532 (red) and 785 (blue) nm
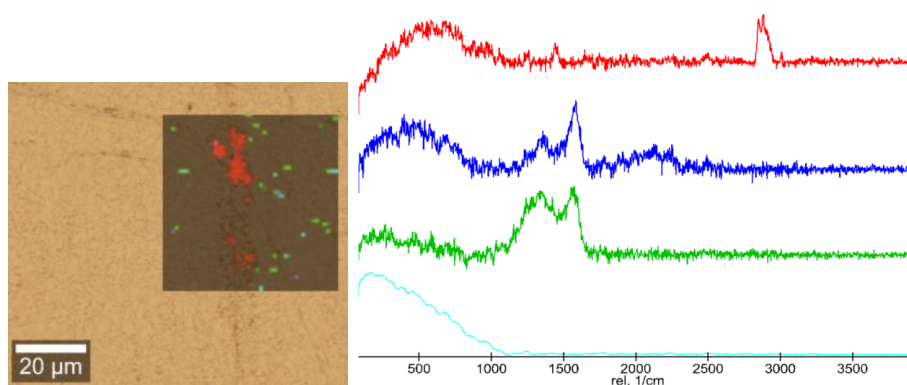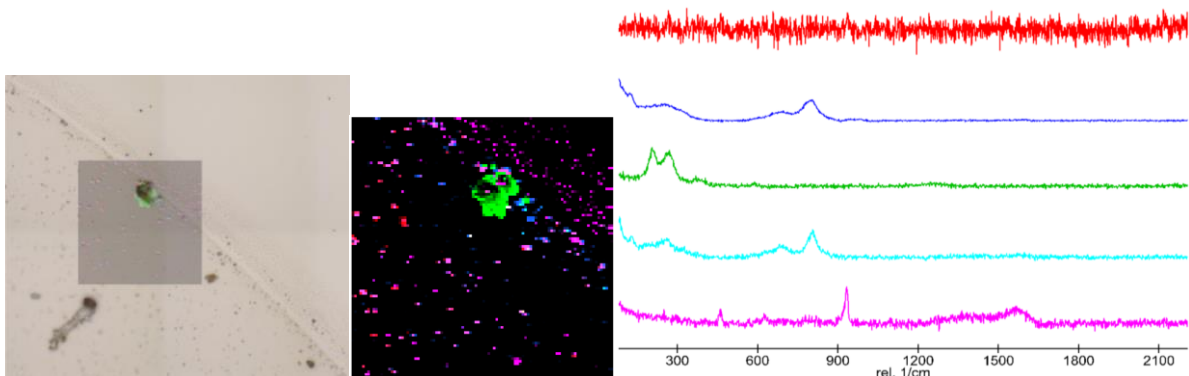

A Raman map (overlaid on the optical image) of the Au sample showing the distribution of the individual components obtained via True Component Analysis. (λ 532nm laser source, power 20 mW Map size 50x50 µm, Points per Line100, Lines per image 100, Integration Time 0.2 s. Measured by Dr Josh Lea at Oxford Instrument.)
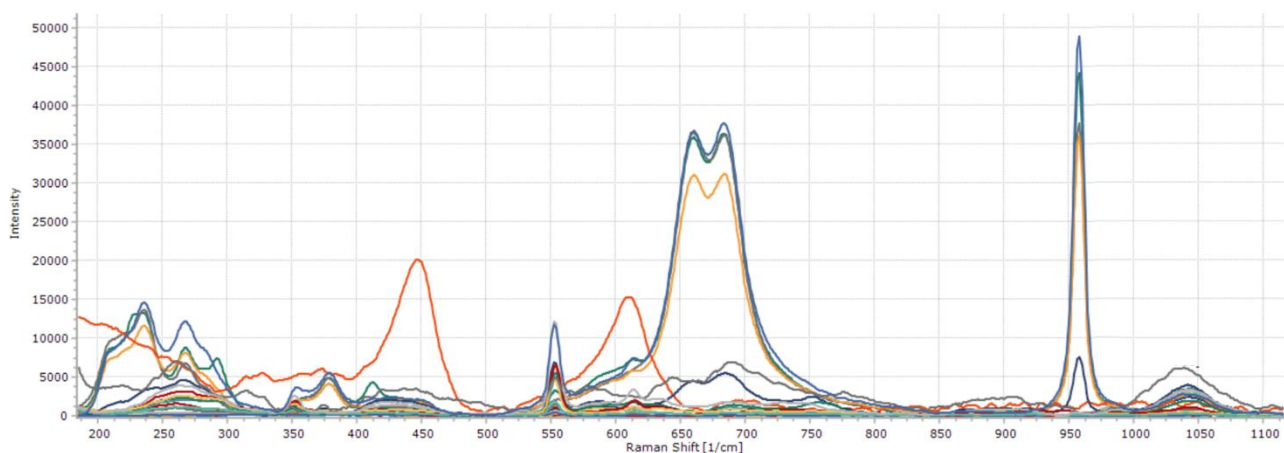
Examples of impurities and electrolyte Raman spectra obtained in different part of the sample (baseline and smooth corrected. laser λ 532nm, power 10 mW)
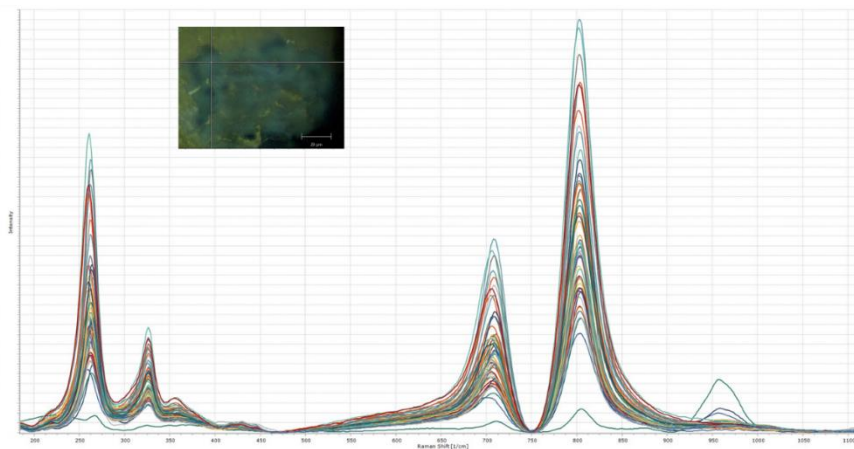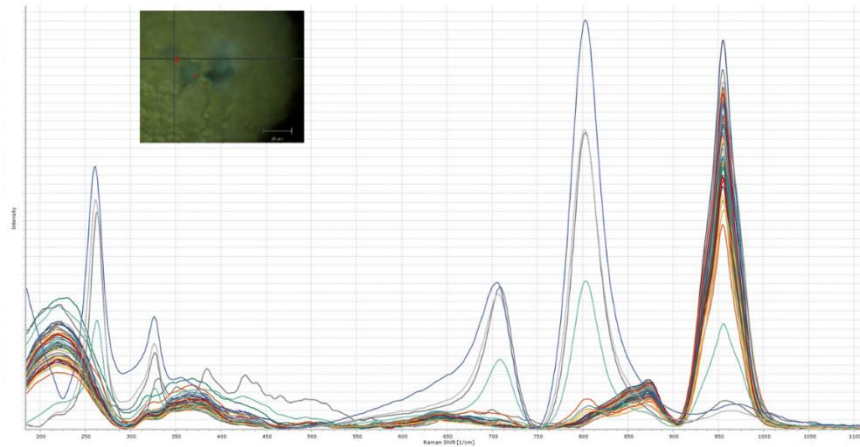
Accumulated Raman spectra of the hBN sample mapped twice with a 1µm grid (baseline and smooth corrected). Inset shows the optical images of the surface before the measurements. The heat generated during the measurement allowed to expose the inner layers with the tungsten oxide. Sample prepared by deposition of the tungsten oxide powder with a concentration of 500 ppm (laser λ 532nm, power 10 mW)


A Raman map (overlaid on the optical image) of the hBN substrate showing the distribution of the individual components obtained via True Component Analysis.(Laser λ 532nm, Power 50 mW, Map size 50x50 µm, Points per Line 100, Lines per image 100, Integration Time 0.5 s. Measured by Leah Josh at Oxford Instrument.)

Appendix D – Impedimetric monitoring of clusters adsorption on the nanomesh
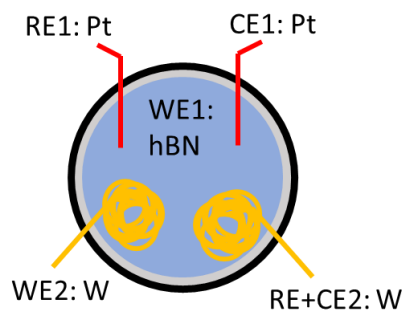
Configuration of the electrode for monitoring of the evolution of the nanomesh impedance during the tungsten oxide electrochemical generation.
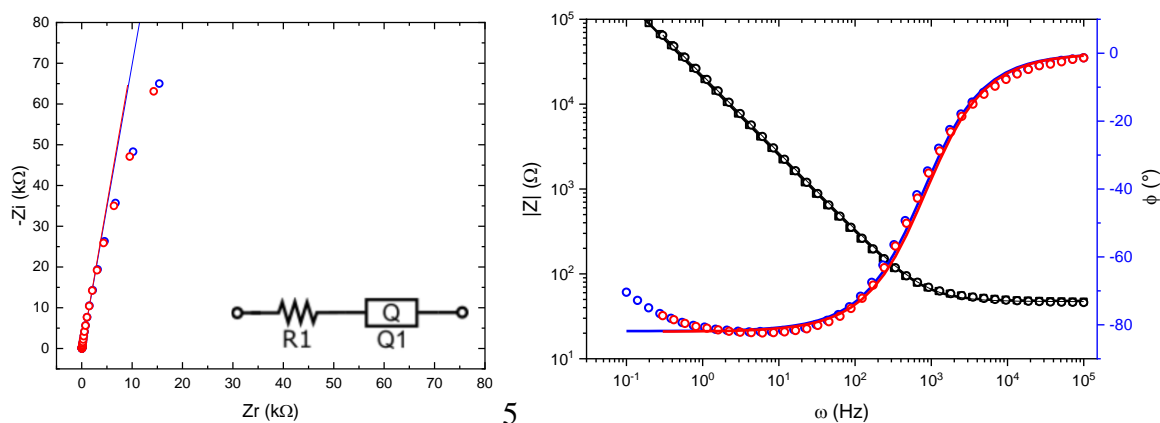
Impedance of the hBN nanomesh measured with at potential near OCP (0.2V vs Ag/AgCl) before (blue) and after two hours (red) of electrochemical generation carried in the same cell.

	Initial	Final
R_s ($\Omega \cdot cm^2$)	2.35	2.39
Q_d ($\mu s^{\alpha}/\Omega\ cm^2$)	171.9	183.8
α_d	0.911	0.909

Parameters of the equivalent circuit resulting from the fitting of the impedance spectra